A COUPLED THREE-DIMENSIONAL HYDRAULIC FRACTURE PROPAGATION MODEL ACCOUNTING FOR THE EFFECT OF BEDDING LAYERS

A Dissertation

by

JIZHOU TANG

Submitted to the Office of Graduate and Professional Studies of
Texas A&M University
in partial fulfillment of the requirements for the degree of

DOCTOR OF PHILOSOPHY

Chair of Committee,	Kan Wu
Committee Members,	Christine Ehlig-Economides
	Peter Valko
	Benchun Duan
Head of Department,	Jeff Spath

August 2018

Major Subject: Petroleum Engineering

ABSTRACT

Unconventional shale reservoirs have been the most recent production frontier in the United States. Optimization of the production of shale reservoirs depends greatly on hydraulic fracture treatment. In recent studies, strongly contrasting properties of multi-layered rocks and pervasively distributed weak interfaces become the primary factors in determining the propagation pathway of fractures, which further influences the fracture height growth and fracture geometry. Few of hydraulic fracture propagation models enable us to quantitatively estimate the fracture height containment or predict fracture geometry under the influence of multiple bedding planes. Therefore, development of a reliable and practical simulator for modeling fracture propagation that enables accurate prediction of the fracture height growth in multiple-layered shale formation is critical to efficient resource development.

In this dissertation, I have developed a coupled three-dimensional hydraulic fracture propagation model considering the effects of bedding planes. In this model, a fully three-dimensional displacement discontinuity method is used to model the rock deformation. The advantage of this approach is that it addresses both the mechanical interaction between hydraulic fractures and weak bedding planes in three-dimensional space and the physical mechanism of slippage along weak bedding planes. Fluid flow governed by finite difference methodology considers the flow in both vertical fractures and opening bedding planes. An iterative algorithm is used to couple fluid flow and rock deformation. Comparison between the developed model and the PKN model showed good agreement. Analysis of different fracture geometry and sensitivity analysis of different

parameters are conducted to investigate their impacts on the opening of vertical fractures and bedding planes, and also the shear sliding along the bedding planes. A width jump, created along the vertical fracture when the vertical fracture penetrates the bedding plane, is regarded as a primary mechanism of fracture height containment. Both widths of fracture segments and shear sliding along the bedding plane are positively related with the distance between the injection source and the bedding plane segment. Higher formation Young's modulus can restrict the opening of bedding plane and retard the fluid percolation into the bedding plane. Smaller fracture spacing gives rise of the opening reduction of the fracture segments. Our model enables us to provide a critical insight for the selection of the proppant grain size range and assessment of the required pumping rate to obtain the required width at both junction and intersected bedding plane.

DEDICATION

To my parents

ACKNOWLEDGEMENTS

First of all, I would express my deep gratitude to my advisor, Professor Kan Wu, for her sincerity, unrequited guidance and substantial support during my Ph.D program.

I also feel grateful to my former advisor, Professor Christine Ehlig-Economides, for her solicitous instruction on my research and future career.

Then I would like to thank my committee members, Professor Benchun Duan, and Professor Peter Valko, for their guidance and support throughout my Ph.D program.

Special thanks also go to Dr. Wei Yu, for his continuous help and guidance on the improvement of my academic skills.

Cordially thanks to my team members: Dr. Lihua Zuo, Xiaodong Hu, Xuyang Guo, Jiawei Li, Anusarn Sangnimnuan, Seunghwan Chun and Ross Patterson.

Finally, thanks to my mother and father for their encouragement and endless love and support.

CONTRIBUTORS AND FUNDING SOURCES

Contributors

This work was supervised by a dissertation committee consisting of Professor Kan Wu [advisor], Professor Peter Valko of the Department of Petroleum Engineering and Professor Benchun Duan of the Department of Geology and Geophysics, and Professor Christine Ehlig-Economides of the Department of Petroleum Engineering at University of Houston.

All work for the dissertation was completed independently by the student.

Funding Sources

Graduate study was supported by Texas A&M Engineering Experiment Station (TEES).

NOMENCLATURE

u_j	Displacement Component at a Point, m
σ_{jk}	Stress Component at a Point, Pa
u_i	Displacement Component over the Boundary Region, m
t_i	Traction Component, Pa
$M_{ij}, N_{ij}, E_{ijk}, T_{ijk}$	Tensor Fields with Displacements at a Point under a Certain Traction
$\sigma_{11}, \sigma_{22}, \sigma_{33}, \sigma_{12}, \sigma_{13}, \sigma_{23}$	Stress Components from Analytical Solution, Pa
$D_{SL}(D_1)$	Shear Displacement Discontinuity in the Fracture Length Direction, m
$D_{SH}(D_2)$	Shear Displacement Discontinuity in the Fracture Height Direction, m
$D_{NN}(D_3)$	Normal Displacement Discontinuity, m
G	Shear Modulus, Pa
ν	Poisson's Ratio,

J_i	Derivatives of a Kernel Analytical Solution for i from 1 to 19
(x_1, x_2, x_3)	Local Coordinate System, m
(X, Y, Z)	Global Coordinate System, m
R_1	Matrix Considering the Rotation of y Axis
R_2	Matrix Considering the Rotation of z Axis
R	Matrix Considering the Rotation of y and z Axis
β	Strike Angle
θ	Dip Angle
γ	Difference of Strike Angle between Element i and Element j
φ	Difference of Dip Angle between Element i and Element j
$A_{SL,SL}^{ik}$	Boundary Influence Coefficient of Induced Shear Stress in the Fracture Length Direction of Element i Resulting from Shear Displacement Discontinuity in the Fracture Length Direction of Element k
$A_{SL,SH}^{ik}$	Boundary Influence Coefficient of Induced Shear Stress in the Fracture Length Direction of Element i Resulting from Shear

	Displacement Discontinuity in the Fracture Height Direction of Element k
$A_{SL,NN}^{ik}$	Boundary Influence Coefficient of Induced Shear Stress in the Fracture Length Direction of Element i Resulting from Normal Displacement Discontinuity of Element k
$A_{SH,SL}^{ik}$	Boundary Influence Coefficient of Induced Shear Stress in the Fracture Height Direction of Element i Resulting from Shear Displacement Discontinuity in the Fracture Length Direction of Element k
$A_{SH,SH}^{ik}$	Boundary Influence Coefficient of Induced Shear Stress in the Fracture Height Direction of Element i Resulting from Shear Displacement Discontinuity in the Fracture Height Direction of Element k
$A_{SH,NN}^{ik}$	Boundary Influence Coefficient of Induced Shear Stress in the Fracture Height Direction of Element i Resulting from Normal Displacement Discontinuity of Element k
$A_{NN,SL}^{ik}$	Boundary Influence Coefficient of Induced Normal Stress of Element i Resulting from Shear Displacement Discontinuity in the Fracture Length Direction of Element k

$A_{NN,SH}^{ik}$	Boundary Influence Coefficient of Induced Normal Stress of Element i Resulting from Shear Displacement Discontinuity in the Fracture Height Direction of Element k
$A_{NN,NN}^{ik}$	Boundary Influence Coefficient of Induced Normal Stress of Element i Resulting from Normal Displacement Discontinuity of Element k
σ_{SL}^{i}	Shear Stress in the Fracture Length Direction of Element i, Pa
σ_{SH}^{i}	Shear Stress in the Fracture Height Direction of Element i, Pa
σ_{NN}^{i}	Normal Stress of Element i, Pa
${\sigma_{XX}}^{P}$	Induced Normal Stress in the X Direction at Any Point P, Pa
${\sigma_{YY}}^{P}$	Induced Normal Stress in the Y Direction at Any Point P, Pa
${\sigma_{ZZ}}^{P}$	Induced Normal Stress in the Z Direction at Any Point P, Pa
${\sigma_{XY}}^{P}$	Induced Shear Stress in the XY Plane at Any Point P, Pa
${\sigma_{XZ}}^{P}$	Induced Shear Stress in the XZ Plane at Any Point P, Pa
${\sigma_{YZ}}^{P}$	Induced Shear Stress in the YZ Plane at Any Point P, Pa
$(\tilde{x}_1, \tilde{x}_2, \tilde{x}_3)$	Non-dimensional Coordinate System

$\tilde{\sigma}_{SL}$	Non-dimensional Shear Stress along the Fracture Length Direction
$\tilde{\sigma}_{SH}$	Non-dimensional Shear Stress along the Fracture Height Direction
$\tilde{\sigma}_{NN}$	Non-dimensional Normal Stress
$\widetilde{D}_{SL}$	Non-dimensional Shear Displacement Discontinuity in the Fracture Length Direction
$\widetilde{D}_{SH}$	Non-dimensional Shear Displacement Discontinuity in the Fracture Height Direction
$\widetilde{D}_{NN}$	Non-dimensional Normal Displacement Discontinuity
H_0	Reference Length, m
P_0	Reference Pressure, Pa
w	Fracture Width, m
P	Net Pressure within the Fracture, Pa
b	Half-length of the Fracture, m
x	Location along the Fracture Length, m

$\vec{v} = (v_x, v_y, v_z)$	Velocity Vector, m/s
$\vec{\mathrm{F}}$	Body Force per Unit Mass, Pa
ρ	Fluid Density, kg/m^3
$p(x, y, t)$	Pressure at a Certain Time t, Pa
$Q(x, y, t)$	Fluid Injection Rate at a Certain Time t, m^3/s
q_x	Flow Rate per Unit Length in the x Direction, m^2/s
q_y	Flow Rate per Unit Length in the y Direction, m^2/s
q_L	Leak-off Rate, m^2/s
C_L	Experimentally determined leak-off coefficient
$\tau(x, y)$	Initiation time for the leak-off process at a point (x, y), s

TABLE OF CONTENTS

Page

LIST OF FIGURES

LIST OF TABLES

1. GENERAL INTRODUCTION

1.1 Background

Unconventional shale reservoirs have been the most recent production frontier in the United States. After 1990s, shale plays such as Barnett, Bakken, Eagle Ford, Permian, Niobrara and Utica, become the primary source of shale oil and shale gas for industrial use and people's daily life (IlScams.org). Figure 1.1 depicts the forecast for shale oil production of different plays in the US from 2010 to 2025. From this figure, we observe that Bakken and Eagle Ford shales contribute the primary growth of shale oil production. Moreover, LUKOIL (2013) forecasted that shale oil production in the US would have an intensive growth in the following 5-10 years and the production amount would reach 3.9 mb/d by 2025.

With the technology breakthrough in the areas of horizontal drilling and hydraulic fracturing, US wants to hold the unconventional gas resources firmly in its hands. LUKOIL (2013) forecasted that US would become a net exporter of gas by 2020 due to flourish shale gas revolution. Figure 1.2 illustrates recoverable reserves of unconventional gas and unconventional gas production forecast, respectively. Figure 1.2 (a) reveals that those four regions, Asia, North American, Latin American, and Africa, become the dominant sources of shale gas supply in the world. Figure 1.2 (b) indicates that the forecasting production of unconventional gas in US far exceeds other world regions.

Although China has begun its own shale gas revolution in Sichuan basin, it is challenge to decrease the production cost as low as US in the short term as a result of shortage of gas infrastructure and limited water resources.

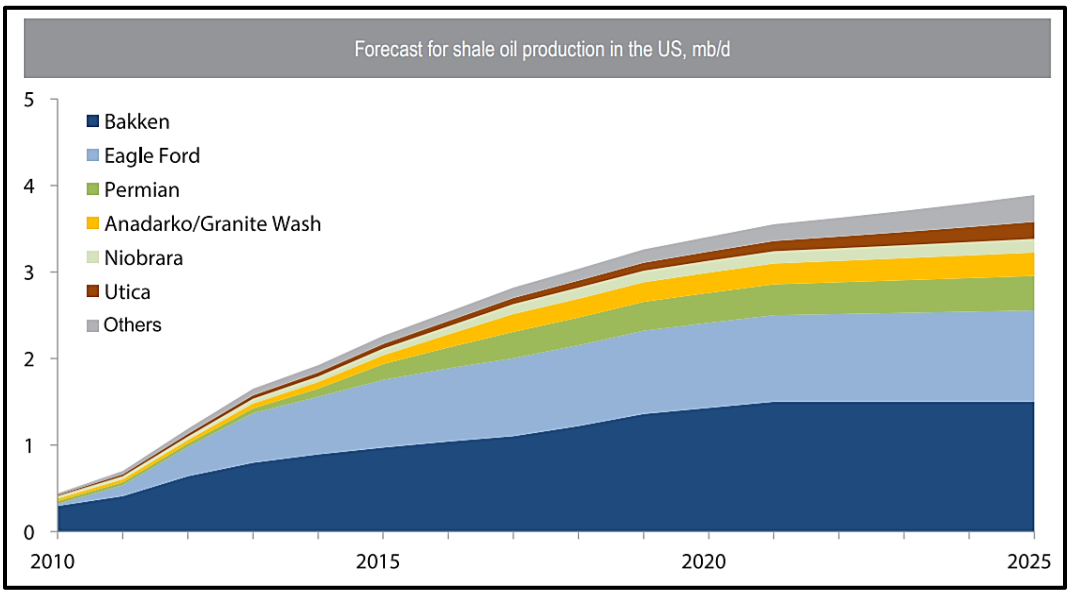

Figure 1.1: Forecast for shale oil production in the US (Reprinted from LUKOIL 2013).

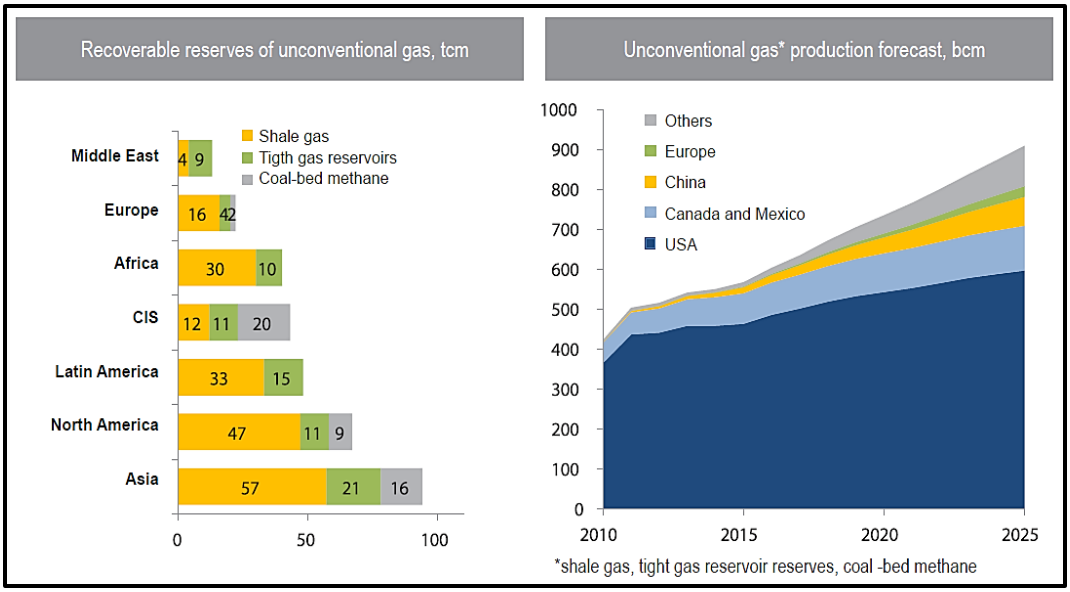

Figure 1.2: Unconventional gas (a) recoverable reserves and (b) production forecast (Reprinted from LUKOIL 2013).

Optimization of the production of shale reservoirs is greatly dependent on hydraulic fracture treatment, which is successfully applied to most unconventional resources such as shale gas and tight oil. This technology aims at injecting a mixture of water, sand, chemical additives through a drilled well under a high but controlled pressure, so as to stimulate the oil/gas production (Lepotter 2014). According to the *Geological Society of America*, small cracks would be generated during the hydraulic fracture treatment and they would propagate to a desired distance from the wellbore by controlling the pumping rate, fluid pressure, and injection time (GSA 2014). Figure 1.3 illustrated an intuitive picture of horizontal drilling and hydraulic fracturing. A horizontal wellbore is drilled and mixture liquid (water, sand, and additives) would be injected into an oil-or-gas bearing rock formation via the pumper truck, small cracks are created at the beginning and more complex fracture geometry would generated with the continuous injection.

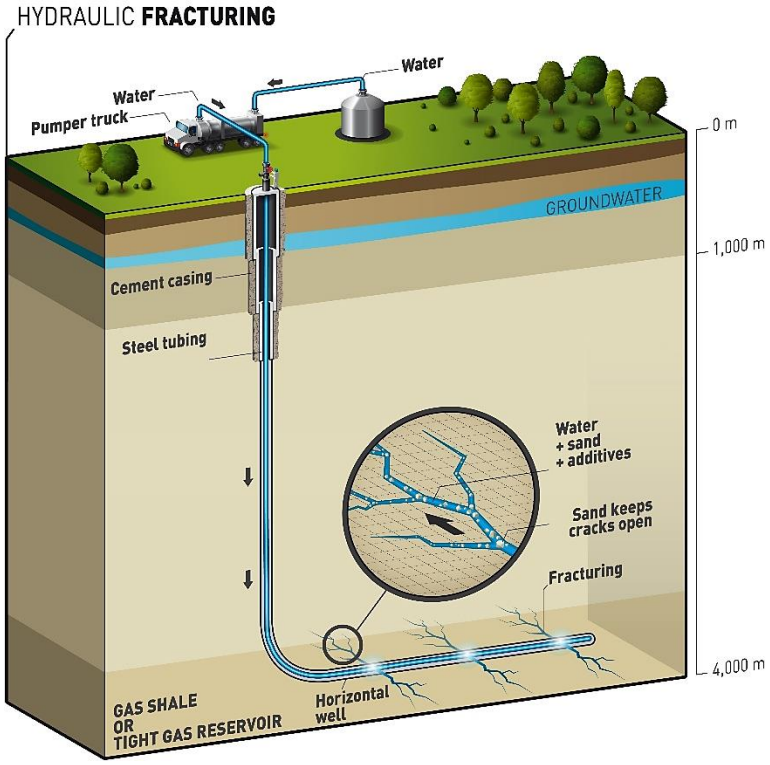

Figure 1.3: Horizontal drilling and Hydraulic Fracturing (Reprinted from Lepotter 2014).

1.2 Problem Statement

Shale formations, as a representative of unconventional reservoirs, have complicated structures with thin beds or laminations, accompanied by varying in-situ stress states, layer material properties, and interlayer interface properties. Rock layering, presented as bed parallel ash beds, mineralized veins and slickensides, pervasively exists in the shale reservoirs (Suarez-Rivera et al. 2016). (2011) indicated that rock layering is comprised of vertically stacking of repetitious parasequences as a result of cyclic climate and sea level alteration. All these organic-rich and mineralized layers can be observed from different range of scales such as outcrop scale, core scale, small sample scale, and SEM scale (Suarez-Rivera et al. 2016). Figure 1.4 shows the photographs of thin rock

layering on outcrops from the Montney and Eagle Ford shales. We can observe that these multi-layered shales have strongly contrasting properties and the bedding plane/interface between two adjoining rock layers can break or slide during fracturing treatments.

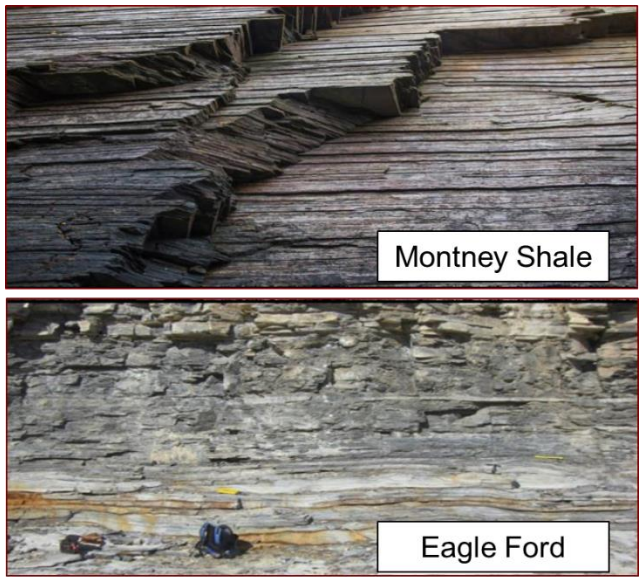

Figure 1.4: Photographs of thin rock layering on outcrops from the Montney and Eagle Ford Shales (Reprinted from Suarez-Rivera et al. 2016).

Hydraulic fracture interactions with multiple bedding planes in shale formations during hydraulic fracturing treatment can generate T-shape fractures, kinks, branches, offsets, and ledges along the bedding planes as the result of fracture crossing, arresting, blunting, and/or diversion at the bedding planes (Fisher and Warpinski 2012; Abbas et al. 2014; Cohen et al. 2017). Figure 1.5 elaborates the fracture height growth with multiple bedding layers. We labeled the fractures, bedding planes and wellbore as orange, yellow and black, respectively. Physical mechanisms of facture propagation in multiple bedding layers are concluded as: (1) The fracture directly penetrates the bedding plane; (2) The

fracture is arrested by the bedding plane; (3) The fracture contacts the bedding plane and then an offset is generated along the bedding plane. All these mechanisms would significantly influence the fracture height growth and final fracture geometry. Hence, multi-layered rocks and pervasively distributed weak bedding planes become the primary factors in determining the propagation pathway of fractures, which further influences the fracture height growth and whole fracture geometry.

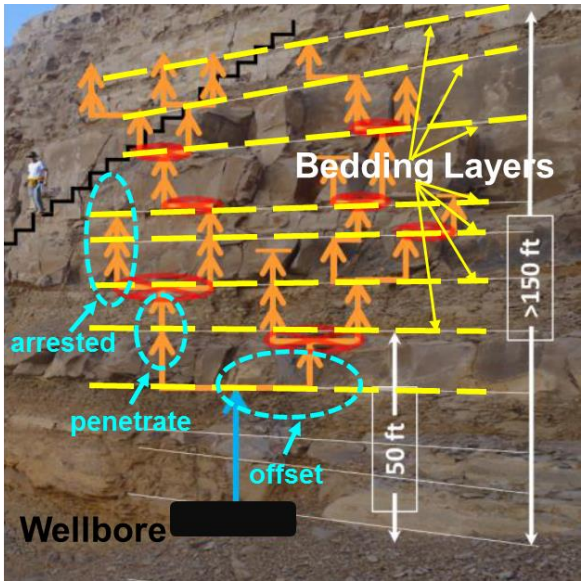

Figure 1.5: Fracture height growth with multiple bedding layers (Adapted from Suarez-Rivera et al. 2016).

Previous study indicated that fracture height is overestimated if hydraulic fracture models merely consider the mechanisms of stress contrast (Simonson et al. 1978; Palmer and Carroll Jr. 1983; Adachi et al. 2010) and modulus contrast (Van Eekelen 1982; Smith et al. 2001; Gu and Siebrits 2008) between adjacent layers. Based on previous field studies (Warpinski and Teufel, 1987; Rutledge et al. 2016; Suarez-Rivera et al. 2016),

experimental investigations (Teufel and Clark 1984; Thiercelin et al. 1987; Bunger et al. 2015; Xing et al. 2016; Zhao et al. 2016; Lee et al. 2016; Llanos et al. 2017; Ma et al. 2017; Li et al. 2017) and model analysis (Cooke 2001; Miskimins and Barree 2003; Zhang et al. 2007; Zhang and Jeffrey 2008; Gu et al. 2008; Gu and Weng, 2010; Wang et al. 2012; Abbas et al. 2014; Chuprakov and Prioul 2015; Liu and Valko 2015; Zou et al. 2016; Cohen et al. 2017; Zhang et al. 2017), it reveals that weak bedding planes also play an important role in determining the fracture height growth during hydraulic fracturing treatments. Gu et al. (2008) considered the interfacial sliding between bedding layers (weak interfaces) as one of the mechanisms that would alter hydraulic fracture growth. Fisher and Warpinski (2012) indicated that weak interfaces are regarded as a significant factor in stopping fracture height growth at shallow depths, initiating interface fractures or creating offsets along the interface. Chuprakov (2015) developed an analytical model describing the fluid leak-off from the hydraulic fracture into permeable horizontal interfaces and demonstrating the significant effect of bedding layer leak-off on fracture propagation. Laboratory investigation showed that hydraulic fracture propagation is ceased as a result of fluid infiltration into the weak interface (Bunger et al. 2015). Zhao et al. (2016) conducted experiments to investigate the effect of bedding interfaces on hydraulic fracture propagation that revealed that thick and high strength bedding interfaces divert injected fluid along the bedding interfaces and thereby arrest growth of the main fracture. Suarez-Rivera et al. (2016) illustrated that the distribution of weak interfaces is an indicator for proper selection of the lateral landing depth, which helps improve the final propped and connected fracture height and enhances the well performance. Well

productivity alters significantly with different lateral landing depth in the Bakken, Barnett, Niobrara, Woodford, Montney, Eagle Ford and other plays. Llanos et al. (2017) conducted experimental studies and then demonstrated that the frictional interfaces would greatly affect the overall fracture growth due to the slip initiation along the interface. Thus, it is extremely necessary to develop a hydraulic fracture propagation model considering the effect of rock layering on fracture height growth.

1.3 Motivation and Objectives

Considering fracture propagation in shale formations with multiple bedding layers, more complicated fracture geometries with "T" shapes, kinks, and offsets are often induced (Olson 1995; Hedayati and Meadows 1996; Fisher and Warpinski 2012). Experiments (Warpinski et al. 1993) and microseismic measurements (Maxwell et al. 2002; Fisher et al. 2002) also indicate that complex fracture networks pervasively exist in unconventional reservoirs during hydraulic fracturing stimulation. Weng (2015) reviewed current available hydraulic fracturing models that deal with complex hydraulic fracture networks. In terms of modeling fracture height growth, these models face challenges due to a lack of understanding effects of weak interfaces on hindering fracture height growth. Hence, the objective of my research is to develop a new model which can simulate the fracture height growth with discontinuities: (1) Develop a fully three-dimensional displacement discontinuity method to deal with multiple fractures with arbitrary angles in 3D space; (2) Couple the rock deformation and fluid flow to simulate fracture propagation

in 3D space; (3) Investigate the effects of the weak bedding interfaces on fracture propagation; (4) Accurately quantify fracture width distribution on bedding planes.

1.4 Literature Review

Adachi et al. (2007) concluded that the basic processes for characterizing the physical mechanisms of hydraulic fracturing: rock deformation induced by the fluid injection, fluid flow in the fracture considering the leak-off effect, and fracture propagation in the formation. In terms of modeling rock deformation, the theory of linear elasticity is adopted and solutions are obtained via applying boundary element method (Crouch and Starfield 1983) or finite element method (Smith and Griffiths 1998). Finite element (Dhatt and Touzat 1984), finite difference (LeVeque 2007) or finite volume approaches (Versteeg and Malalasekera 2007) are used for fluid flow modeling in order to solve the partial differential equation satisfying the conservation of mass and the conservation of momentum, which also correlate with pressure gradient, fracture width, and fluid velocity (Weng 2015; Calhoun and LeVeque 2000). Fracture propagation criterion depends on the linear elastic fracture mechanics (LEFM) theory that propagation initiates if stress intensity factor along the fracture front approximates the rock toughness (Valko and Economides 1995).

The simulation of hydraulic fracturing, dating back to 1950s (Hubbert and Willis 1957; Crittendon 1959) and flourishing through nearly 60 years, is developed from simple 2D models to pseudo 3D (P3D) models then to fully 3D models which depend on the degree of complexity of fracture geometry and required computational accuracy for the

predictions (Carter et al. 2000). The simple 2D models include PKN model (Perkins and Kern 1961; Nordren 1972), KGD model (Khristianovic and Zheltov 1955; Geertsma and de Klerk 1969) and radial model (Sneddon 1946; Green and Sneddon 1950). The pseudo 3D models (Simonson et al. 1978; Settari and Cleary 1982; Palmer and Carroll 1982; Palmer and Carroll 1983; Palmer and Craig 1984; Settari and Cleary 1986; Meyer 1986; Fung et al. 1987; Mack and Warpinski 2000; Adachi et al. 2010) evolved from 1980s and gradually displaced the position of 2D models. These models behave more efficiently in computational process and account for the growth of fracture height. Since from 1980s, the planar 3D (PL3D) models (Clifton et al. 1981; Barree 1983; Abou-Sayed et al. 1984; Gu 1987; Gu and Yew 1988; Clifton and Wang 1991; Peirce and Siebrits 2001; Siebrits and Peirce 2002) emerged and with the following 20 years, they had a booming evolution. Compared with the P3D models, PL3D models reveal a better accuracy for the solution but less computational efficiency. Additionally, a majority of PL3D models integrate 3D rock deformation and 2D fluid flow in the lateral and vertical directions, however, most P3D models only consider the fluid flow in the lateral direction.

1.4.1 Current Fracture Model for Unconventional Reservoirs

All the planar hydraulic fracture models discussed above are called as conventional models, which use different numerical approaches and simulate the propagation of a single planar fracture. These models do not consider the effect of fracture interaction. However, factors such as the wellbore angle relative to the in-situ stress field, stress anisotropy and injection parameters, can determine the creation of the non-planar hydraulic fracture

(multiple-parallel fractures, reoriented fractures or T-shaped fractures) (Olson 1995; Abass et al. 1996). Moreover, microseismic monitoring reveals complex fracture networks generated in shale reservoirs during the hydraulic fracturing treatments (Fisher et al. 2002; Maxwell et al. 2002). Hence, the conventional hydraulic fracture models used for bi-wing planar geometry becomes inapplicable for complex fracture geometry in shale reservoirs (Weng et al. 2011). The complex fracture geometry is primarily created by two aspects: (1) multiple fracture initiation generated by perforation clusters; (2) the intersection between hydraulic fractures (HF) and pre-existing weak planes, such as natural fractures (NF) and bedding layers. Yamamoto et al. (2004), Wong and Xu (2013), and Shin and Sharma (2014) proposed multiple hydraulic fracture models instead of the conventional single planar model, accounting for both rock deformation and fluid flow. For the HF approaching the pre-existing NF in the formation, the intersection would give rise to opening of NF, branching or path diversion of HF and eventually generate complex fracture networks. Weng (2015) put forward six scenarios of HF interaction with NF as: (1) direct crossing without offset; (2) crossing with offset; (3) HF arrested at NF; (4) branching at the intersecting location; (5) branching or turning at the end of NF; (6) NF dilation due to shear slippage. Moreover, laboratory hydraulic fracture experiments were made to study the interactions between hydraulic fractures and natural fractures (Fan et al. 2014; Fan and Zhang 2014; Zhang and Fan 2014). Extensive theoretical (Renshaw and Pollard 1995; Gu and Weng 2010; Gu et al. 2011), experimental work (Blanton 1986; Warpinski and Teufel 1987) and numerical simulation (Zhang and Jeffrey 2006; Zhang and Jeffrey 2008; Bao et al. 2014; Zhao and Young 2009; Dahi-Taleghani and Olson 2011;

Chuprakov et al. 2013) are conducted to investigate the crossing criterion of fracture propagation at the intersection and given a reasonable explanation on fracture behaviors.

Recently, hydraulic fracture models for unconventional reservoirs applied to complex fracture networks are developed to consider more comprehensive physical aspects (such as rock deformation, fluid flow and leak-off effect, fracture propagation, interaction between HF and NF or HF and HF, fracture height containment, proppant transport, effect of multi-layer, and formation heterogeneity) and implement microseismic monitoring, downhole temperature measurements (Cui and Zhu 2014; Cui et al. 2016) and diagnostic fracture injection testing (Liu and Ehlig-Economides 2015; Liu and Ehlig-Economides 2016; Ehlig-Economides and Liu 2017) for estimating the fracture calibration parameters. The models are categorized as boundary element based models (Olson 2004; Olson 2008; Olson and Dahi-Taleghani 2009; McClure 2012; Yamamoto et al. 2004; Rungamornrat et al. 2005; Wong and Xu 2013; Wong et al. 2013; Wu 2014), coupled geomechanics and reservoir models (Ji et al. 2009; Dean and Schmidt 2008; Chen 2012; Singh et al. 2014; Huang et al. 2016; Yang et al. 2016), distinct element method based models (Shi 1988; Jing et al. 2001; Fu et al. 2011; Nagel et al. 2011; Riahi and Damjanac 2013), lumped P3D network models (Xu et al. 2009; Meyer and Bazan 2011), and cell-based P3D network models (Weng et al. 2011; Kresse et al. 2013).

1.4.2 Current Models Considering Bedding Layer Effect

Weak bedding planes play an important role in stopping fracture height growth, initiating interface fractures or creating offsets in the fracture. These offsets put a huge

restriction on fracture height growth due to the fact that fracture width becomes narrower in the offset range and possibility of proppant bridging. Currently, very few models have been developed to investigate the bedding layer effects on fracture geometry. Cooke (2011) developed a numerical model to investigate fracture-interface contacting problems and analyzed frictional slip and correlated opening-mode fracture propagation using a two-dimensional Boundary Element Method (BEM). Zhang et al. (2007) employed a two-dimensional boundary element method (BEM) based model to study the interaction mechanisms between fracture and bedding interfaces. Gu et al. (2008) implemented an interfacial slip model to a pseudo-three-dimensional (P3D) hydraulic fracture simulator and indicated that interfacial slippage along the bedding planes plays a significant role in determining the fracture height growth, fracture width deformation, fracture pressure and entire fracture geometry. Abbas et al. (2014) employed the Extended Finite Element Method (XFEM) to study geometric effects of fracture offsets that retard fracture height growth, as depicted in Figure 1.6 (a). Chuprakov and Prioul (2015) elaborated a FracT model which can solve the problem of elasto-frictional fracture contact with weak horizontal interfaces, as illustrated in Figure 1.6 (b). Cohen et al. (2017) proposed a new Stacked Height Growth (SHG) model, regarded as an enhanced Pseudo 3D model (P3D), can model the effect of ledges at weak interfaces. Izadi et al. (2017) developed a fully coupled 3D hydraulic fracturing simulator to investigate multiple fractures interference with consideration of the effect of bedding planes. Zhang et al. (2017) described a new cell-based pseudo-3D (P3D) model which accounts for the effect of multiple elastic layers on fracture height growth. Llanos et al. (2017) conducted experiments by using

MineHF2D model developed by CSIRO and demonstrated that fracture propagation is greatly influenced by the slippage along the frictional interfaces. All these models have limitations: (1) All models above are limited within two-dimensional space; (2) It is difficult for quantifying fracture width around the junction area between the vertical fracture and the bedding plane; (3) It rarely accounts for the multiple fracture cases.

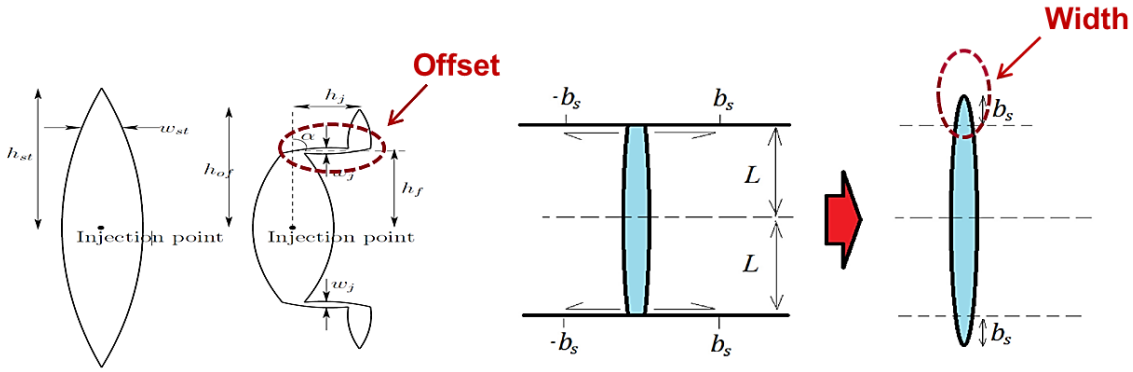

Figure 1.6: Models for simulating the bedding layer effects on fracture geometry (a) Extended Finite Element Method (XFEM) based model (Adapted from Abbas et al. 2014) and (b) FracT model (Adapted from Chuprakov and Prioul 2015).

1.4.3 Impact of Inclined Bedding Planes on Fracture Propagation

In reality, multi-layered bedding planes are not horizontally distributed in the shale reservoirs and thus the intersection angle between the fractures and the inclined bedding planes is non-orthogonal. Previous studies showed that the intersection angle plays a significant impact on the fracture approaching at the frictional discontinuities such as natural fractures, interface planes and veins (Blanton 1982; Zhou et al. 2008; Gu and Weng 2010; Virgo et al. 2014; Lee et al. 2016; Lee et al. 2018). Gu and Weng (2010) expanded the Renshaw and Pollard's (1995) criterion for solving non-orthogonal approaching cases.

This modified Model indicated that a fracture is more difficult to cross the oblique bedding plane with a smaller intersection angle less than **90**°, which creates more chance for the fracture to divert or propagate along the bedding plane (Gu and Weng 2010; Gu et al. 2011). Sarmadivaleh and Rasouli (2014) also proposed an extended criterion based on Renshaw and Pollard's criterion to deal with non-orthogonal cohesive interface plane. Virgo et al. (2014) did tension tests based on Three-Dimensional Discrete Element Method (3D DEM) and found that fracture deflection occurs at a low approaching angle and the length of the deflection pathway along the interface increases with the decrement of approaching angle of the vein. Lee et al. (2016) numerically modeled fracture-vein interactions with different approach angles and concluded that tensile fractures were more likely to divert into pre-existing veins in the case of smaller approach angle. Lee et al. (2018) found that the hydraulic fracture with a vein of smaller approach angle would propagate all the way along the vein and fracture would be kinked back into another layer leaving a short diversion along the vein when the approach angle is large.

2. ROCK DEFORMATION

This chapter first introduces the development history of the three-dimensional displacement discontinuity method (3D DDM). Mathematical derivation of our developed 3D DDM is then presented, which enables dealing with cases of multiple fractures with arbitrary angles in three dimensions. In other word, all the vertical/slanted hydraulic fractures and frictional discontinuities such as natural fractures and horizontal/oblique interface segments, can be simulated by our 3D DDM. The numerical solution from 3D DDM has a good match with the 2D analytical solution as shown in the model validation section. The cases of different fracture geometries are then analyzed in this chapter, such as a symmetric crossing-shaped fracture, a T-shaped fracture, an I-shaped fracture and a complex fracture geometry with offsets. For each case, horizontal fractures can be regarded as opening of weak horizontal interfaces and vertical fractures would either be arrested or step over from interfaces. Displacement discontinuities on vertical and horizontal fractures were investigated to study the effects of opening of weak horizontal interfaces.

---

*Part of this section is reprinted with permission from "A 3-D Model for Simulation of Weak Interface Slippage for Fracture Height Containment in Shale Reservoirs" by J. Tang, K. Wu, 2018. International Journal of Solids and Structures, Copyright [2018] by Elsevier.

2.1 Three-Dimensional Displacement Discontinuity Method (3D DDM)

Compared with finite element method (FEM), boundary element method (BEM) has the advantage of reducing the dimension of elasticity equation and only discretizing the fracture surface. Hence, BEM has high computational efficiency. With those advantages of surface-only discretization and high computational efficiency, a boundary element method, Displacement Discontinuity Method (DDM), has been widely used in modeling rock deformation of hydraulic fracturing treatments for both homogeneous and multi-layered formations in two dimensions or three dimensions (Vandamme and Curran 1989; Siebrits and Peirce 2002; Siebrits and Peirce 2007; Wu and Olson 2015; Kumar and Ghassemi 2015; Kumar and Ghassemi 2016; Wu et al. 2016; Xie et al. 2018). Moreover, DDM can be also extended to stress evolution prediction, pressure distribution and production estimation (Yu et al. 2016; Sangnimnuan et al. 2017; Guo et al. 2018; Li et al. 2018). In this dissertation, we employed this method with coupled fluid flow to investigate the effects of weak horizontal interfaces on fracture height growth and fracture geometry.

The Displacement Discontinuity Method (DDM) firstly put forward by Crouch (1976). Crouch and Starfield (1983) then proposed 2D displacement discontinuity method (DDM) approach, which classified as a special direct boundary element method (BEM) for solving the stress and displacement within the unknown boundary under the given assumption. 2D DDM only does fracture discretization along fracture length and hence neglects the fracture width alteration along the fracture height direction. Olson (2004), Olson (2008) and Olson and Dahi-Taleghani (2009) developed an enhanced 2D DDM model for both single and multiple fractures propagation, which adding a correction factor

for taking the effect of fracture height into consideration. In this enhanced model, the fracture width at any location along the fracture length direction means the average width over the fracture height. Wu and Olson (2013) found that the computational accuracy of the enhanced 2D DDM Model for multiple fractures is less than that for single fracture due to the fact of underestimation of fracture interaction leading to larger fracture apertures. Shou (1993) developed a fully Three-Dimensional Displacement Discontinuity Method (3D DDM), regarding displacement discontinuity as a constant and using rectangular element mesh in an infinite medium. The analytical solutions for stress distribution and displacement discontinuity can be obtained by coordinate transformation. Shou (1997) then presented a 3D higher order displacement discontinuity element method, which using nine collocation points spread over a nine element patch, in order to accurately predict both stresses and displacements for the field points closer than one element length. Based on the fully 3D DDM, Wu (2014) proposed a simplified 3D DDM (S3D DDM) method that only pick a single element over the fracture height and derive the correction factor under the assumption of vertical fractures and without any dip-slip shear stress. This new model provides an accurate solution for the induced stress of fractures and works for multiple fractures but misses the displacement discontinuities in the fracture height direction. Nintcheu Fata (2016) proposed a three-dimensional DDM scheme applying unstructured triangular meshes instead of conventional rectangular-shaped structure to conform to a domain of any shapes.

2.1.1 Mathematical Derivation

Shou (1993) introduced Displacement Discontinuity Method (DDM) to determine the induced stresses and displacements for fractures in three dimensions with a given boundary condition,

$$u_j(\omega) = \int_{\Psi} M_{ij}(\omega, \varphi)\, t_i(\varphi)\, d\Psi(\varphi) - \int_{\Psi} N_{ij}(\omega, \varphi)\, u_i(\varphi)\, d\Psi(\varphi) \tag{2.1}$$

$$\sigma_{jk}(\omega) = \int_{\Psi} E_{ijk}(\omega, \varphi)\, t_i(\varphi)\, d\Psi(\varphi) - \int_{\Psi} T_{ijk}(\omega, \varphi)\, u_i(\varphi)\, d\Psi(\varphi) \tag{2.2}$$

where, $u_j(\omega)$ and $\sigma_{jk}(\omega)$ represent displacement components and stress components at a point ω, respectively. $M_{ij}(\omega, \varphi)$, $N_{ij}(\omega, \varphi)$, $E_{ijk}(\omega, \varphi)$, $T_{ijk}(\omega, \varphi)$ are tensor fields with displacements at a point ω under the traction applied to a point φ. $t_i(\varphi)$ and $u_i(\varphi)$ represent a traction component and a displacement component over the boundary region Ψ, respectively.

Wu (2014) described a single three-dimensional vertical fracture discretized into numerous rectangular elements in an infinite elastic medium. The fully three-dimensional displacement discontinuity method (3D DDM) is further developed for modeling multiple fractures with arbitrary angles in three dimensions. Figure 2.1 illustrates a three-dimensional horizontal fracture in an infinite elastic solid. The fracture is divided into many planar elements with the assumption of constant displacement discontinuities on each element. The global coordinates are (X, Y, Z) and the local coordinates are (x_1, x_2, x_3). Each rectangular element has two opposite surfaces labeled as $x_3 = 0^+$ and $x_3 = 0^-$.

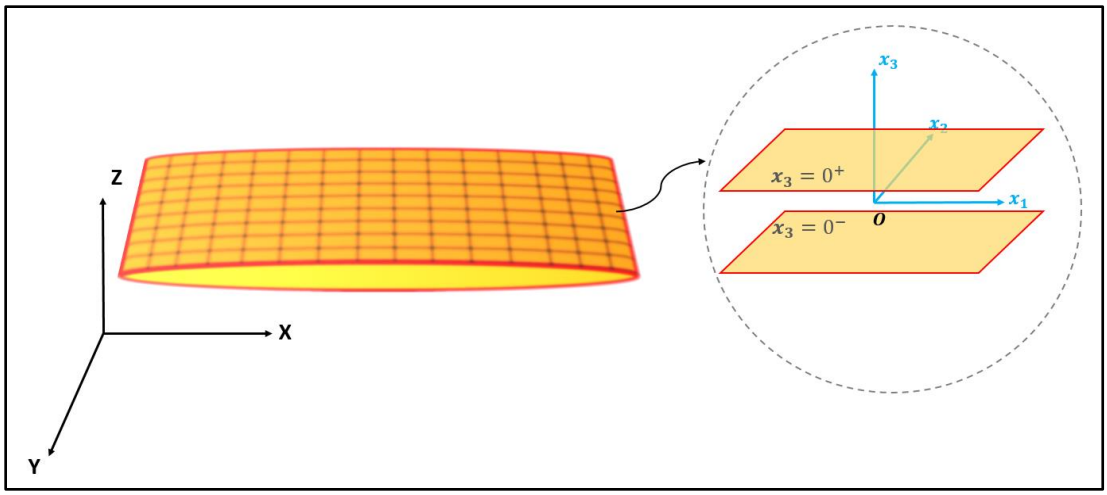

Figure 2.1: A three-dimensional horizontal crack in an infinite elastic solid (Tang and Wu 2018).

The analytical solution for stress components, σ_{ij}, induced by an element with constant displacement discontinuities (Rongved 1957; Salamon 1964), can be given under the local coordinate system x_1, x_2, x_3, as:

$$\sigma_{11} = \frac{G}{4\pi(1-\nu)}\{D_1[2J_8 - x_3J_{10}] + D_2[2\upsilon J_9 - x_3J_{11}] + D_3[J_6 + (1-2\upsilon)J_5 - x_3J_{12}]\}$$

$$\sigma_{22} = \frac{G}{4\pi(1-\nu)}\{D_1[2\upsilon J_8 - x_3J_{13}] + D_2[2J_9 - x_3J_{14}] + D_3[J_6 + (1-2\upsilon)J_4 - x_3J_{15}]\}$$

$$\sigma_{33} = \frac{G}{4\pi(1-\nu)}\{D_1[-x_3J_{16}] + D_2[-x_3J_{17}] + D_3[X_6 - x_3J_{18}]\}$$

$$\sigma_{12} = \frac{G}{4\pi(1-\nu)}\{D_1[(1-\upsilon)J_9 - x_3J_{11}] + D_2[(1-\upsilon)J_8 - x_3J_{13}]$$

$$- D_3[(1-2\upsilon)J_7 + x_3J_{19}]\}$$

$$\sigma_{13} = \frac{G}{4\pi(1-\nu)}\{D_1[J_6 + \upsilon J_5 - x_3J_{12}] - D_2[\upsilon J_7 + x_3J_{19}] - D_3[x_3J_{16}]\}$$

$$\sigma_{23} = \frac{G}{4\pi(1-\nu)}\{-D_1[\upsilon J_7 + x_3 J_{19}] + D_2[J_6 + \upsilon J_4 - x_3 J_{15}] - D_3[x_3 J_{17}]\},$$

..... (2.3)

where G is the shear modulus and ν is the Poisson's ratio. D_1 is the shear displacement discontinuity in the fracture length direction, D_2 is the shear displacement discontinuity in the fracture height direction, D_3 is the normal displacement discontinuity, also named as fracture width. These three components of displacement discontinuities are depicted in Figure 2.2. J_i represents the derivatives of a kernel analytical solution found using a Green's function approach for i ranging from 1 to 19.

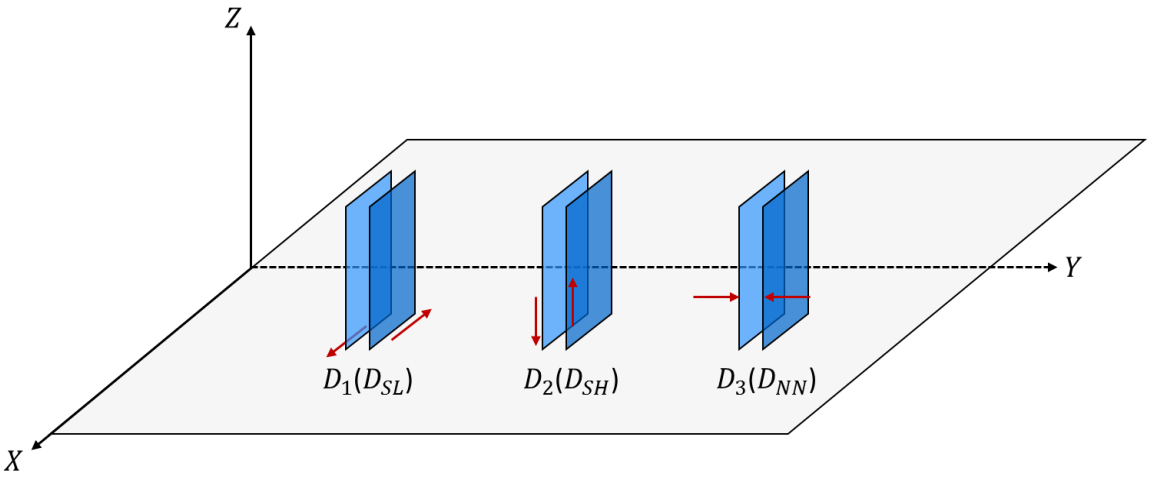

Figure 2.2: Three components of displacement discontinuities - $D_1(D_{SL})$ is the shear displacement discontinuity in the fracture length direction (x axis), $D_2(D_{SH})$is the shear displacement discontinuity in the fracture height direction (z axis), $D_3(D_{NN})$ is the normal displacement discontinuity (y axis) (Tang and Wu 2018).

When determining stresses at a point (X, Y, Z) with respect to global coordinate system induced by displacement discontinuities of element j, the point (X, Y, Z) needs to be transformed to the local coordinate system (x_1, x_2, x_3) of element j,

$$x_1 = (X - X_j)\cos\beta + (Y - Y_j)\sin\beta$$

$$x_2 = (X - X_j)\sin\beta\sin\theta - (Y - Y_j)\cos\beta\sin\theta + (Z - Z_j)\cos\theta \quad (2.4)$$

$$x_3 = -(X - X_j)\sin\beta\cos\theta + (Y - Y_j)\cos\beta\cos\theta + (Z - Z_j)\sin\theta,$$

where β and θ represent the strike angle and dip angle, respectively.

Before calculating the induced stresses at the midpoint of element i, the coordinate of element i (X_i, Y_i, Z_i) should be written as,

$$x_1 = (X_i - X_j)\cos\beta + (Y_i - Y_j)\sin\beta$$

$$x_2 = (X_i - X_j)\sin\beta\sin\theta - (Y_i - Y_j)\cos\beta\sin\theta + (Z_i - Z_j)\cos\theta \quad (2.5)$$

$$x_3 = -(X_i - X_j)\sin\beta\cos\theta + (Y_i - Y_j)\cos\beta\cos\theta + (Z_i - Z_j)\sin\theta.$$

For vertical fractures, x_2 is the direction of the fracture height for both coordinate of i^{th} element and j^{th} element. Hence, only matrix R_1 is required to consider the rotation of *y* axis,

$$R_1 = R_y = \begin{bmatrix} \cos\beta & 0 & \sin\beta \\ 0 & 1 & 0 \\ -\sin\beta & 0 & \cos\beta \end{bmatrix}. \quad (2.6)$$

For the matrix above, it is clockwise rotation matrix with strike angle β is negative. However, if horizontal fractures are considered in 3D DDM model, another matrix R_2 is required to consider the rotation of *z* axis,

$$R_2 = R_z = \begin{bmatrix} 1 & 0 & 0 \\ 0 & \cos\theta & -\sin\theta \\ 0 & \sin\theta & \cos\theta \end{bmatrix}. \quad (2.7)$$

Finally, the transformed matrix R_1 should be multiplied by matrix R_2 to obtain a new matrix R as below, which utilized for transformation of x_1 and x_2,

$$R = R_2 R_1 = \begin{bmatrix} 1 & 0 & 0 \\ 0 & \cos\theta & -\sin\theta \\ 0 & \sin\theta & \cos\theta \end{bmatrix} \begin{bmatrix} \cos\beta & 0 & \sin\beta \\ 0 & 1 & 0 \\ -\sin\beta & 0 & \cos\beta \end{bmatrix} =$$

$$\begin{bmatrix} \cos\beta & 0 & \sin\beta \\ \sin\beta\sin\theta & \cos\theta & -\cos\beta\sin\theta \\ -\sin\beta\cos\theta & \sin\theta & \cos\beta\cos\theta \end{bmatrix}. \tag{2.8}$$

Transform the point (X, Y, Z) of global coordinate system of element j to the local coordinate system of element j,

$$\begin{bmatrix} x_1 \\ x_2 \\ x_3 \end{bmatrix} = \begin{bmatrix} \cos\beta & 0 & \sin\beta \\ \sin\beta\sin\theta & \cos\theta & -\cos\beta\sin\theta \\ -\sin\beta\cos\theta & \sin\theta & \cos\beta\cos\theta \end{bmatrix} \begin{bmatrix} X - X_j \\ Z - Z_j \\ Y - Y_j \end{bmatrix}. \tag{2.9}$$

Similarly, transform to local coordinate of i^{th} element from local coordinate of j^{th} element,

$$\begin{bmatrix} x_1^i \\ x_2^i \\ x_3^i \end{bmatrix} = \begin{bmatrix} \cos\beta & 0 & \sin\beta \\ \sin\beta\sin\theta & \cos\theta & -\cos\beta\sin\theta \\ -\sin\beta\cos\theta & \sin\theta & \cos\beta\cos\theta \end{bmatrix} \begin{bmatrix} x_1^j \\ x_2^j \\ x_3^j \end{bmatrix}. \tag{2.10}$$

The coordinate of the stresses need to transform from the local reference frame of element j to that of element i based on coordinate transformation, then we obtain the new stress tensor as,

$$\begin{bmatrix} \sigma_{11}^i & \sigma_{12}^i & \sigma_{13}^i \\ \sigma_{21}^i & \sigma_{22}^i & \sigma_{23}^i \\ \sigma_{31}^i & \sigma_{32}^i & \sigma_{33}^i \end{bmatrix} = R \begin{bmatrix} \sigma_{11}^j & \sigma_{12}^j & \sigma_{13}^j \\ \sigma_{21}^j & \sigma_{22}^j & \sigma_{23}^j \\ \sigma_{31}^j & \sigma_{32}^j & \sigma_{33}^j \end{bmatrix} R^T. \tag{2.11}$$

In the new stress tensor, only six stress components are independent and they are written as,

$$\sigma_{11}^i = \cos^2\beta\,\sigma_{11}^j + \sin^2\beta\,\sigma_{33}^j + \sin 2\beta\,\sigma_{13}^j$$

$$\sigma_{22}^{i} = sin^2\,\beta\, sin^2\,\theta\,\sigma_{11}^{j} + cos^2\,\theta\,\sigma_{22}^{j} + cos^2\,\beta\, sin^2\,\theta\,\sigma_{33}^{j} + sin\,\beta\, sin\,2\theta\,\sigma_{12}^{j}$$
$$- sin\,2\beta\, sin^2\,\theta\,\sigma_{13}^{j} - cos\,\beta\, sin\,2\theta\,\sigma_{23}^{j}$$

$$\sigma_{33}^{i} = sin^2\,\beta\, cos^2\,\theta\,\sigma_{11}^{j} + sin^2\,\theta\,\sigma_{22}^{j} + cos^2\,\beta\, cos^2\,\theta\,\sigma_{33}^{j} - sin\,\beta\, sin\,2\theta\,\sigma_{12}^{j}$$
$$- sin\,2\beta\, cos^2\,\theta\,\sigma_{13}^{j} + cos\,\beta\, sin\,2\theta\,\sigma_{23}^{j}$$

$$\sigma_{12}^{i} = \frac{1}{2} sin\,2\beta\, sin\,\theta\,\sigma_{11}^{j} - \frac{1}{2} sin\,2\beta\, sin\,\theta\,\sigma_{33}^{j} + cos\,\beta\, cos\,\theta\,\sigma_{12}^{j} - cos\,2\beta\, sin\,\theta\,\sigma_{13}^{j}$$
$$+ sin\,\beta\, cos\,\theta\,\sigma_{23}^{j}$$

$$\sigma_{13}^{i} = -\frac{1}{2} sin\,2\beta\, cos\,\theta\,\sigma_{11}^{j} + \frac{1}{2} sin\,2\beta\, cos\,\theta\,\sigma_{33}^{j} + cos\,\beta\, sin\,\theta\,\sigma_{12}^{j} + cos\,2\beta\, cos\,\theta\,\sigma_{13}^{j}$$
$$+ sin\,\beta\, sin\,\theta\,\sigma_{23}^{j}$$

$$\sigma_{23}^{i} = -\frac{1}{2} sin^2\,\beta\, sin\,2\theta\,\sigma_{11}^{j} + \frac{1}{2} sin\,2\theta\,\sigma_{22}^{j} - \frac{1}{2} cos^2\,\beta\, sin\,2\theta\,\sigma_{33}^{j} - sin\,\beta\, cos\,2\theta\,\sigma_{12}^{j}$$
$$+ \frac{1}{2} sin\,2\beta\, sin\,2\theta\,\sigma_{13}^{j} + cos\,\beta\, cos\,2\theta\,\sigma_{23}^{j}.$$

…… (2.12)

If only vertical fractures exist in this model, we have $\beta \neq 0°, \theta = 0°$ and six stress components can be written as,

$$\sigma_{11}^{i} = cos^2\,\beta\,\sigma_{11}^{j} + sin^2\,\beta\,\sigma_{33}^{j} + sin\,2\beta\,\sigma_{13}^{j}$$

$$\sigma_{22}^{i} = \sigma_{22}^{j}$$

$$\sigma_{33}^{i} = sin^2\,\beta\,\sigma_{11}^{j} + cos^2\,\beta\,\sigma_{33}^{j} - sin\,2\beta\,\sigma_{13}^{j}$$

$$\sigma_{12}^{i} = \sigma_{21}^{i} = cos\,\beta\,\sigma_{12}^{j} + sin\,\beta\,\sigma_{23}^{j}$$

$$\sigma_{13}^{i} = \sigma_{31}^{i} = -\frac{1}{2} sin\,2\beta\,\sigma_{11}^{j} + \frac{1}{2} sin\,2\beta\,\sigma_{33}^{j} + cos\,2\beta\,\sigma_{13}^{j}$$

$$\sigma_{23}^{i} = \sigma_{32}^{i} = -\sin\beta\,\sigma_{12}^{j} + \cos\beta\,\sigma_{23}^{j}.$$

…… (2.13)

If only horizontal fractures exist in this model, we have $\beta = 0°, \theta \neq 0°$ and six stress components can be represented as,

$$\sigma_{11}^{i} = \sigma_{11}^{j}$$

$$\sigma_{22}^{i} = \cos^2\theta\,\sigma_{22}^{j} + \sin^2\theta\,\sigma_{33}^{j} - \sin 2\theta\,\sigma_{23}^{j}$$

$$\sigma_{33}^{i} = \sin^2\theta\,\sigma_{22}^{j} + \cos^2\theta\,\sigma_{33}^{j} + \sin 2\theta\,\sigma_{23}^{j}$$

$$\sigma_{12}^{i} = \cos\theta\,\sigma_{12}^{j} - \sin\theta\,\sigma_{13}^{j}$$

$$\sigma_{13}^{i} = \sin\theta\,\sigma_{12}^{j} + \cos\theta\,\sigma_{13}^{j}$$

$$\sigma_{23}^{i} = \frac{1}{2}\sin 2\theta\,\sigma_{22}^{j} - \frac{1}{2}\sin 2\theta\,\sigma_{33}^{j} + \cos 2\theta\,\sigma_{23}^{j}.$$

…… (2.14)

To be more general, the normal stress and two shear stresses on element i with arbitrary strike and dip angles can be written as,

$$\sigma_{33}^{i} = \sin^2\gamma\cos^2\varphi\,\sigma_{11}^{j} + \sin^2\varphi\,\sigma_{22}^{j} + \cos^2\gamma\cos^2\varphi\,\sigma_{33}^{j} - \sin\gamma\sin 2\varphi\,\sigma_{12}^{j} - \sin 2\gamma\cos^2\varphi\,\sigma_{13}^{j} + \cos\gamma\sin 2\varphi\,\sigma_{23}^{j}$$

$$\tau_{13}^{i} = -\frac{1}{2}\sin 2\gamma\cos\varphi\,\sigma_{11}^{j} + \frac{1}{2}\sin 2\gamma\cos\varphi\,\sigma_{33}^{j} + \cos\gamma\sin\varphi\,\sigma_{12}^{j} + \cos 2\gamma\cos\varphi\,\sigma_{13}^{j} + \sin\gamma\sin\varphi\,\sigma_{23}^{j}$$

$$\tau_{23}^{i} = -\frac{1}{2}\sin^2\gamma\sin 2\varphi\,\sigma_{11}^{j} + \frac{1}{2}\sin 2\varphi\,\sigma_{22}^{j} - \frac{1}{2}\cos^2\gamma\sin 2\varphi\,\sigma_{33}^{j} - \sin\gamma\cos 2\varphi\,\sigma_{12}^{j} + \frac{1}{2}\sin 2\gamma\sin 2\varphi\,\sigma_{13}^{j} + \cos\gamma\cos 2\varphi\,\sigma_{23}^{j}$$

$$\gamma = \beta_i - \beta_j, \varphi = \theta_i - \theta_j.$$

…… (2.15)

Use Eq. (2.3) as mentioned above and use the terms D_{SL}, D_{SH}, D_{NN} to refer to D_1, D_2, D_3,

$$\sigma_{SL}^{i} = \tau_{13}^{i} = -\frac{1}{2} sin\,2\gamma\, cos\,\varphi\, \sigma_{11}^{j} + \frac{1}{2} sin\,2\gamma\, cos\,\varphi\, \sigma_{33}^{j} + cos\,\gamma\, sin\,\varphi\, \sigma_{12}^{j}$$

$$+ cos\,2\gamma\, cos\,\varphi\, \sigma_{13}^{j} + sin\,\gamma\, sin\,\varphi\, \sigma_{23}^{j}$$

$$= C_r \left(-\frac{1}{2} sin\,2\gamma\, cos\,\varphi\, [2J_8 - x_3 J_{10}] + \frac{1}{2} sin\,2\gamma\, cos\,\varphi\, [-x_3 J_{16}] \right.$$

$$+ cos\,\gamma\, sin\,\varphi\, [(1-\upsilon) J_9 - x_3 J_{11}] + cos\,2\gamma\, cos\,\varphi\, [J_6 + \upsilon J_5 - x_3 J_{12}]$$

$$\left. + sin\,\gamma\, sin\,\varphi\, [-\upsilon J_7 - x_3 J_{19}] \right) D_{SL}$$

$$+ C_r \left(-\frac{1}{2} sin\,2\gamma\, cos\,\varphi\, [2\upsilon J_9 - x_3 J_{11}] + \frac{1}{2} sin\,2\gamma\, cos\,\varphi\, [-x_3 J_{17}] \right.$$

$$+ cos\,\gamma\, sin\,\varphi\, [(1-\upsilon) J_8 - x_3 J_{13}] + cos\,2\gamma\, cos\,\varphi\, [-\upsilon J_7 - x_3 J_{19}]$$

$$\left. + sin\,\gamma\, sin\,\varphi\, [J_6 + \upsilon J_4 - x_3 J_{15}] \right) D_{SH}$$

$$+ C_r \left(-\frac{1}{2} sin\,2\gamma\, cos\,\varphi\, [J_6 + (1-2\upsilon) J_5 - x_3 J_{12}] \right.$$

$$+ \frac{1}{2} sin\,2\gamma\, cos\,\varphi\, [J_6 - x_3 J_{18}] + cos\,\gamma\, sin\,\varphi\, [-(1-2\upsilon) J_7 - x_3 J_{19}]$$

$$\left. + cos\,2\gamma\, cos\,\varphi\, [-x_3 J_{16}] + sin\,\gamma\, sin\,\varphi\, [-x_3 J_{17}] \right) D_{NN}$$

…… (2.16)

$$\sigma_{SH}^{i} = \tau_{23}^{i} = -\frac{1}{2}sin^2\gamma\, sin\, 2\varphi\, \sigma_{11}^{j} + \frac{1}{2}sin\, 2\varphi\, \sigma_{22}^{j} - \frac{1}{2}cos^2\gamma\, sin\, 2\varphi\, \sigma_{33}^{j}$$

$$- sin\,\gamma\, cos\, 2\varphi\, \sigma_{12}^{j} + \frac{1}{2}sin\, 2\gamma\, sin\, 2\varphi\, \sigma_{13}^{j} + cos\,\gamma\, cos\, 2\varphi\, \sigma_{23}^{j}$$

$$= C_r\left(-\frac{1}{2}sin^2\gamma\, sin\, 2\varphi\, [2J_8 - x_3J_{10}] + \frac{1}{2}sin\, 2\varphi\, [2\upsilon J_8 - x_3J_{13}]\right.$$

$$-\frac{1}{2}cos^2\gamma\, sin\, 2\varphi\, [-x_3J_{16}] - sin\,\gamma\, cos\, 2\varphi\, [(1-\upsilon)J_9 - x_3J_{11}]$$

$$\left.+\frac{1}{2}sin\, 2\gamma\, sin\, 2\varphi\, [J_6 + \upsilon J_5 - x_3J_{12}] + cos\,\gamma\, cos\, 2\varphi\, [-\upsilon J_7 - x_3J_{19}]\right) D_{SL}$$

$$+ C_r\left(-\frac{1}{2}sin^2\gamma\, sin\, 2\varphi\, [2\upsilon J_9 - x_3J_{11}] + \frac{1}{2}sin\, 2\varphi\, [2J_9 - x_3J_{14}]\right.$$

$$-\frac{1}{2}cos^2\gamma\, sin\, 2\varphi\, [-x_3J_{17}] - sin\,\gamma\, cos\, 2\varphi\, [(1-\upsilon)J_8 - x_3J_{13}]$$

$$\left.+\frac{1}{2}sin\, 2\gamma\, sin\, 2\varphi\, [-\upsilon J_7 - x_3J_{19}] + cos\,\gamma\, cos\, 2\varphi\, [J_6 + \upsilon J_4 - x_3J_{15}]\right) D_{SH}$$

$$+ C_r\left(-\frac{1}{2}sin^2\gamma\, sin\, 2\varphi\, [J_6 + (1-2\upsilon)J_5 - x_3J_{12}]\right.$$

$$+\frac{1}{2}sin\, 2\varphi\, [J_6 + (1-2\upsilon)J_4 - x_3J_{15}] - \frac{1}{2}cos^2\gamma\, sin\, 2\varphi\, [J_6 - x_3J_{18}]$$

$$- sin\,\gamma\, cos\, 2\varphi\, [-(1-2\upsilon)J_7 - x_3J_{19}] + \frac{1}{2}sin\, 2\gamma\, sin\, 2\varphi\, [-x_3J_{16}]$$

$$\left.+ cos\,\gamma\, cos\, 2\varphi\, [-x_3J_{17}]\right) D_{NN}$$

…… (2.17)

$$\sigma_{NN}^{i} = \sigma_{33}^{i} = sin^2\gamma\, cos^2\varphi\, \sigma_{11}^{j} + sin^2\varphi\, \sigma_{22}^{j} + cos^2\gamma\, cos^2\varphi\, \sigma_{33}^{j} - sin\gamma\, sin\,2\varphi\, \sigma_{12}^{j}$$
$$- sin\,2\gamma\, cos^2\varphi\, \sigma_{13}^{j} + cos\gamma\, sin\,2\varphi\, \sigma_{23}^{j}$$
$$= C_r(sin^2\gamma\, cos^2\varphi\, [2J_8 - x_3J_{10}] + sin^2\varphi\, [2\upsilon J_8 - x_3J_{13}]$$
$$+ cos^2\gamma\, cos^2\varphi\, [-x_3J_{16}] - sin\gamma\, sin\,2\varphi\, [(1-\upsilon)J_9 - x_3J_{11}]$$
$$- sin\,2\gamma\, cos^2\varphi\, [J_6 + \upsilon J_5 - x_3J_{12}] + cos\gamma\, sin\,2\varphi\, [-\upsilon J_7 - x_3J_{19}])D_{SL}$$
$$+ C_r(sin^2\gamma\, cos^2\varphi\, [2\upsilon J_9 - x_3J_{11}] + sin^2\varphi\, [2J_9 - x_3J_{14}]$$
$$+ cos^2\gamma\, cos^2\varphi\, [-x_3J_{17}] - sin\gamma\, sin\,2\varphi\, [(1-\upsilon)J_8 - x_3J_{13}]$$
$$- sin\,2\gamma\, cos^2\varphi\, [-\upsilon J_7 - x_3J_{19}] + cos\gamma\, sin\,2\varphi\, [J_6 + \upsilon J_4 - x_3J_{15}])D_{SH}$$
$$+ C_r(sin^2\gamma\, cos^2\varphi\, [J_6 + (1-2\upsilon)J_5 - x_3J_{12}]$$
$$+ sin^2\varphi\, [J_6 + (1-2\upsilon)J_4 - x_3J_{15}] + cos^2\gamma\, cos^2\varphi\, [J_6 - x_3J_{18}]$$
$$- sin\gamma\, sin\,2\varphi\, [-(1-2\upsilon)J_7 - x_3J_{19}] - sin\,2\gamma\, cos^2\varphi\, [-x_3J_{16}]$$
$$+ cos\gamma\, sin\,2\varphi\, [-x_3J_{17}])D_{NN}.$$

$$C_r = \frac{G}{4\pi(1-\nu)}$$

…… (2.18)

where G is the shear modulus and ν is the Poisson's ratio.

In term of the boundary influence coefficients matrix, each element of matrix is written as:

$$A_{SL,SL} = C_r\left(-\frac{1}{2}sin\,2\gamma\, cos\,\varphi\, [2J_8 - x_3J_{10}] + \frac{1}{2}sin\,2\gamma\, cos\,\varphi\, [-x_3J_{16}]\right.$$
$$+ cos\gamma\, sin\,\varphi\, [(1-\upsilon)J_9 - x_3J_{11}] + cos\,2\gamma\, cos\,\varphi\, [J_6 + \upsilon J_5 - x_3J_{12}]$$
$$\left. + sin\gamma\, sin\,\varphi\, [-\upsilon J_7 - x_3J_{19}]\right)$$

$$A_{SL,SH} = C_r\left(-\frac{1}{2}sin\,2\gamma\,cos\,\varphi\,[2vJ_9 - x_3J_{11}] + \frac{1}{2}sin\,2\gamma\,cos\,\varphi\,[-x_3J_{17}]\right.$$
$$+ cos\,\gamma\,sin\,\varphi\,[(1-v)J_8 - x_3J_{13}] + cos\,2\gamma\,cos\,\varphi\,[-vJ_7 - x_3J_{19}]$$
$$\left.+ sin\,\gamma\,sin\,\varphi\,[J_6 + vJ_4 - x_3J_{15}]\right)$$

$$A_{SL,NN} = C_r\left(-\frac{1}{2}sin\,2\gamma\,cos\,\varphi\,[J_6 + (1-2v)J_5 - x_3J_{12}] + \frac{1}{2}sin\,2\gamma\,cos\,\varphi\,[J_6 - x_3J_{18}]\right.$$
$$+ cos\,\gamma\,sin\,\varphi\,[-(1-2v)J_7 - x_3J_{19}] + cos\,2\gamma\,cos\,\varphi\,[-x_3J_{16}]$$
$$\left.+ sin\,\gamma\,sin\,\varphi\,[-x_3J_{17}]\right)$$

$$A_{SH,SL} = C_r\left(-\frac{1}{2}sin^2\,\gamma\,sin\,2\varphi\,[2J_8 - x_3J_{10}] + \frac{1}{2}sin\,2\varphi\,[2vJ_8 - x_3J_{13}]\right.$$
$$-\frac{1}{2}cos^2\,\gamma\,sin\,2\varphi\,[-x_3J_{16}] - sin\,\gamma\,cos\,2\varphi\,[(1-v)J_9 - x_3J_{11}]$$
$$\left.+\frac{1}{2}sin\,2\gamma\,sin\,2\varphi\,[J_6 + vJ_5 - x_3J_{12}] + cos\,\gamma\,cos\,2\varphi\,[-vJ_7 - x_3J_{19}]\right)$$

$$A_{SH,SH} = C_r\left(-\frac{1}{2}sin^2\,\gamma\,sin\,2\varphi\,[2vJ_9 - x_3J_{11}] + \frac{1}{2}sin\,2\varphi\,[2J_9 - x_3J_{14}]\right.$$
$$-\frac{1}{2}cos^2\,\gamma\,sin\,2\varphi\,[-x_3J_{17}] - sin\,\gamma\,cos\,2\varphi\,[(1-v)J_8 - x_3J_{13}]$$
$$\left.+\frac{1}{2}sin\,2\gamma\,sin\,2\varphi\,[-vJ_7 - x_3J_{19}] + cos\,\gamma\,cos\,2\varphi\,[J_6 + vJ_4 - x_3J_{15}]\right)$$

$$A_{SH,NN} = C_r \left(-\frac{1}{2} sin^2 \gamma \, sin \, 2\varphi \, [J_6 + (1-2v)J_5 - x_3 J_{12}] \right.$$

$$+ \frac{1}{2} sin \, 2\varphi \, [J_6 + (1-2v)J_4 - x_3 J_{15}] - \frac{1}{2} cos^2 \gamma \, sin \, 2\varphi \, [J_6 - x_3 J_{18}]$$

$$- sin \, \gamma \, cos \, 2\varphi \, [-(1-2v)J_7 - x_3 J_{19}] + \frac{1}{2} sin \, 2\gamma \, sin \, 2\varphi \, [-x_3 J_{16}]$$

$$\left. + cos \, \gamma \, cos \, 2\varphi \, [-x_3 J_{17}] \right)$$

$$A_{NN,SL} = C_r (sin^2 \gamma \, cos^2 \varphi \, [2J_8 - x_3 J_{10}] + sin^2 \varphi \, [2vJ_8 - x_3 J_{13}]$$

$$+ cos^2 \gamma \, cos^2 \varphi \, [-x_3 J_{16}] - sin \, \gamma \, sin \, 2\varphi \, [(1-v)J_9 - x_3 J_{11}]$$

$$- sin \, 2\gamma \, cos^2 \varphi \, [J_6 + vJ_5 - x_3 J_{12}] + cos \, \gamma \, sin \, 2\varphi \, [-vJ_7 - x_3 J_{19}])$$

$$A_{NN,SH} = C_r (sin^2 \gamma \, cos^2 \varphi \, [2vJ_9 - x_3 J_{11}] + sin^2 \varphi \, [2J_9 - x_3 J_{14}]$$

$$+ cos^2 \gamma \, cos^2 \varphi \, [-x_3 J_{17}] - sin \, \gamma \, sin \, 2\varphi \, [(1-v)J_8 - x_3 J_{13}]$$

$$- sin \, 2\gamma \, cos^2 \varphi \, [-vJ_7 - x_3 J_{19}] + cos \, \gamma \, sin \, 2\varphi \, [J_6 + vJ_4 - x_3 J_{15}])$$

$$A_{NN,NN} = C_r (sin^2 \gamma \, cos^2 \varphi \, [J_6 + (1-2v)J_5 - x_3 J_{12}]$$

$$+ sin^2 \varphi \, [J_6 + (1-2v)J_4 - x_3 J_{15}] + cos^2 \gamma \, cos^2 \varphi \, [J_6 - x_3 J_{18}]$$

$$- sin \, \gamma \, sin \, 2\varphi \, [-(1-2v)J_7 - x_3 J_{19}] - sin \, 2\gamma \, cos^2 \varphi \, [-x_3 J_{16}]$$

$$+ cos \, \gamma \, sin \, 2\varphi \, [-x_3 J_{17}])$$

…… (2.19)

According to coordinate transformation, the induced normal stress and two shear stresses for a given element are calculated by summarizing contributions of displacement discontinuities of all boundary elements. The matrix equation can be formulated as,

$$\begin{bmatrix} \sigma_{SL}^i \\ \sigma_{SH}^i \\ \sigma_N^i \end{bmatrix} = \begin{bmatrix} A_{SL,SL}^{ik} & A_{SL,SH}^{ik} & A_{SL,NN}^{ik} \\ A_{SH,SL}^{ik} & A_{SH,SH}^{ik} & A_{SH,NN}^{ik} \\ A_{NN,SL}^{ik} & A_{NN,SH}^{ik} & A_{NN,NN}^{ik} \end{bmatrix} \begin{bmatrix} D_{SL}^k \\ D_{SH}^k \\ D_{NN}^k \end{bmatrix}, \quad (2.20)$$

where D_{SL}^{k} is the shear displacement discontinuity of element *k* in the fracture length direction, D_{SH}^{k} is the shear displacement discontinuity of element *k* in the fracture height direction, D_{NN}^{k} is the normal displacement discontinuity of element *k*. In addition, $(\sigma_{NN})^{i}, (\sigma_{SL})^{i}, (\sigma_{SH})^{i}$ represent the normal stress and shear stresses in fracture length and height directions at element *i*, respectively.

After calculating the displacement discontinuity values of all boundary elements, then the stresses at any point *P* in the body frame can be determined by the following equations,

$$\sigma_{XX}{}^{P} = cos^2\beta\,\sigma_{11} + sin^2\beta\,sin^2\theta\,\sigma_{22} + sin^2\beta\,cos^2\theta\,\sigma_{33} + sin\,2\beta\,sin\,\theta\,\sigma_{12} - sin\,2\beta\,cos\,\theta\,\sigma_{13} - sin^2\beta\,sin\,2\theta\,\sigma_{23}$$

$$\sigma_{YY}{}^{P} = sin^2\beta\,\sigma_{11} + cos^2\beta\,sin^2\theta\,\sigma_{22} + cos^2\beta\,cos^2\theta\,\sigma_{33} - sin\,2\beta\,sin\,\theta\,\sigma_{12} + sin\,2\beta\,cos\,\theta\,\sigma_{13} - cos^2\beta\,sin\,2\theta\,\sigma_{23}$$

$$\sigma_{ZZ}{}^{P} = cos^2\theta\,\sigma_{22} + sin^2\theta\,\sigma_{33} + sin\,2\theta\,\sigma_{23}$$

$$\sigma_{XY}{}^{P} = \frac{1}{2}sin\,2\beta\,\sigma_{11} - \frac{1}{2}sin\,2\beta\,sin^2\theta\,\sigma_{22} - \frac{1}{2}sin\,2\beta\,cos^2\theta\,\sigma_{33} - cos\,2\beta\,sin\,\theta\,\sigma_{12} + cos\,2\beta\,cos\,\theta\,\sigma_{13} + \frac{1}{2}sin\,2\beta\,sin\,2\theta\,\sigma_{23}$$

$$\sigma_{XZ}{}^{P} = \frac{1}{2}sin\,\beta\,sin\,2\theta\,\sigma_{22} - \frac{1}{2}sin\,\beta\,sin\,2\theta\,\sigma_{33} + cos\,\beta\,cos\,\theta\,\sigma_{12} + cos\,\beta\,sin\,\theta\,\sigma_{13} - sin\,\beta\,cos\,2\theta\,\sigma_{23}$$

$$\sigma_{YZ}{}^{P} = -\frac{1}{2}cos\,\beta\,sin\,2\theta\,\sigma_{22} + \frac{1}{2}cos\,\beta\,sin\,2\theta\,\sigma_{33} + sin\,\beta\,cos\,\theta\,\sigma_{12} + sin\,\beta\,sin\,\theta\,\sigma_{13} + cos\,\beta\,cos\,2\theta\,\sigma_{23}$$

…… (2.21)

$$\sigma_{XX}{}^{P} = cos^2\beta\,\{C_rD_1[2J_8 - x_3J_{10}] + C_rD_2[2vJ_9 - x_3J_{11}]$$
$$+ C_rD_3[J_6 + (1-2v)J_5 - x_3J_{12}]\}$$
$$+ sin^2\beta\,sin^2\theta\,\{C_rD_1[2vJ_8 - x_3J_{13}] + C_rD_2[2J_9 - x_3J_{14}]$$
$$+ C_rD_3[J_6 + (1-2v)J_4 - x_3J_{15}]\}$$
$$+ sin^2\beta\,cos^2\theta\,\{C_rD_1[-x_3J_{16}] + C_rD_2[-x_3J_{17}] + C_rD_3[J_6 - x_3J_{18}]\}$$
$$+ sin\,2\beta\,sin\,\theta\,\{C_rD_1[(1-v)J_9 - x_3J_{11}] + C_rD_2[(1-v)J_8 - x_3J_{13}]$$
$$+ C_rD_3[-(1-2v)J_7 - x_3J_{19}]\}$$
$$- sin\,2\beta\,cos\,\theta\,\{C_rD_1[J_6 + vJ_5 - x_3J_{12}] + C_rD_2[-vJ_7 - x_3J_{19}]$$
$$+ C_rD_3[-x_3J_{16}]\}$$
$$- sin^2\beta\,sin\,2\theta\,\{C_rD_1[-vJ_7 - x_3J_{19}] + C_rD_2[J_6 + vJ_4 - x_3J_{15}]$$
$$+ C_rD_3[-x_3J_{17}]\}$$
$$= C_r(cos^2\beta\,[2J_8 - x_3J_{10}] + sin^2\beta\,sin^2\theta\,[2vJ_8 - x_3J_{13}]$$
$$+ sin^2\beta\,cos^2\theta\,[-x_3J_{16}] + sin\,2\beta\,sin\,\theta\,[(1-v)J_9 - x_3J_{11}]$$
$$- sin\,2\beta\,cos\,\theta\,[J_6 + vJ_5 - x_3J_{12}] - sin^2\beta\,sin\,2\theta\,[-vJ_7 - x_3J_{19}])D_1$$
$$+ C_r(cos^2\beta\,[2vJ_9 - x_3J_{11}] + sin^2\beta\,sin^2\theta\,[2J_9 - x_3J_{14}]$$
$$+ sin^2\beta\,cos^2\theta\,[-x_3J_{17}] + sin\,2\beta\,sin\,\theta\,[(1-v)J_8 - x_3J_{13}]$$
$$- sin\,2\beta\,cos\,\theta\,[-vJ_7 - x_3J_{19}] - sin^2\beta\,sin\,2\theta\,[J_6 + vJ_4 - x_3J_{15}])D_2$$
$$+ C_r(cos^2\beta\,[J_6 + (1-2v)J_5 - x_3J_{12}]$$
$$+ sin^2\beta\,sin^2\theta\,[J_6 + (1-2v)J_4 - x_3J_{15}] + sin^2\beta\,cos^2\theta\,[J_6 - x_3J_{18}]$$
$$+ sin\,2\beta\,sin\,\theta\,[-(1-2v)J_7 - x_3J_{19}] - sin\,2\beta\,cos\,\theta\,[-x_3J_{16}]$$
$$- sin^2\beta\,sin\,2\theta\,[-x_3J_{17}])D_3$$

…… (2.22)

$$\sigma_{YY}{}^{P} = sin^2\beta\,\{C_rD_1[2J_8 - x_3J_{10}] + C_rD_2[2\upsilon J_9 - x_3J_{11}]$$
$$+ C_rD_3[J_6 + (1-2\upsilon)J_5 - x_3J_{12}]\} + cos^2\beta\,sin^2\theta\,\{C_rD_1[2\upsilon J_8 - x_3J_{13}]$$
$$+ C_rD_2[2J_9 - x_3J_{14}] + C_rD_3[J_6 + (1-2\upsilon)J_4 - x_3J_{15}]\}$$
$$+ cos^2\beta\,cos^2\theta\,\{C_rD_1[-x_3J_{16}] + C_rD_2[-x_3J_{17}] + C_rD_3[J_6 - x_3J_{18}]\}$$
$$- sin\,2\beta\,sin\,\theta\,\{C_rD_1[(1-\upsilon)J_9 - x_3J_{11}] + C_rD_2[(1-\upsilon)J_8 - x_3J_{13}]$$
$$+ C_rD_3[-(1-2\upsilon)J_7 - x_3J_{19}]\} + sin\,2\beta\,cos\,\theta\,\{C_rD_1[J_6 + \upsilon J_5 - x_3J_{12}]$$
$$+ C_rD_2[-\upsilon J_7 - x_3J_{19}] + C_rD_3[-x_3J_{16}]\}$$
$$- cos^2\beta\,sin\,2\theta\,\{C_rD_1[-\upsilon J_7 - x_3J_{19}] + C_rD_2[J_6 + \upsilon J_4 - x_3J_{15}]$$
$$+ C_rD_3[-x_3J_{17}]\}$$
$$= C_r(sin^2\beta\,[2J_8 - x_3J_{10}] + cos^2\beta\,sin^2\theta\,[2\upsilon J_8 - x_3J_{13}]$$
$$+ cos^2\beta\,cos^2\theta\,[-x_3J_{16}] - sin\,2\beta\,sin\,\theta\,[(1-\upsilon)J_9 - x_3J_{11}]$$
$$+ sin\,2\beta\,cos\,\theta\,[J_6 + \upsilon J_5 - x_3J_{12}] - cos^2\beta\,sin\,2\theta\,[-\upsilon J_7 - x_3J_{19}])D_1$$
$$+ C_r(sin^2\beta\,[2\upsilon J_9 - x_3J_{11}] + cos^2\beta\,sin^2\theta\,[2J_9 - x_3J_{14}]$$
$$+ cos^2\beta\,cos^2\theta\,[-x_3J_{17}] - sin\,2\beta\,sin\,\theta\,[(1-\upsilon)J_8 - x_3J_{13}]$$
$$+ sin\,2\beta\,cos\,\theta\,[-\upsilon J_7 - x_3J_{19}] - cos^2\beta\,sin\,2\theta\,[J_6 + \upsilon J_4 - x_3J_{15}])D_2$$
$$+ C_r(sin^2\beta\,[J_6 + (1-2\upsilon)J_5 - x_3J_{12}]$$
$$+ cos^2\beta\,sin^2\theta\,[J_6 + (1-2\upsilon)J_4 - x_3J_{15}] + cos^2\beta\,cos^2\theta\,[J_6 - x_3J_{18}]$$
$$- sin\,2\beta\,sin\,\theta\,[-(1-2\upsilon)J_7 - x_3J_{19}] + sin\,2\beta\,cos\,\theta\,[-x_3J_{16}]$$
$$- cos^2\beta\,sin\,2\theta\,[-x_3J_{17}])D_3$$

…… (2.23)

$$\sigma_{ZZ}{}^{P} = cos^2\,\theta\,\{C_r D_1[2vJ_8 - x_3 J_{13}] + C_r D_2[2J_9 - x_3 J_{14}]$$

$$+ C_r D_3[J_6 + (1-2v)J_4 - x_3 J_{15}]\} + sin^2\,\theta\,\{C_r D_1[-x_3 J_{16}]$$

$$+ C_r D_2[-x_3 J_{17}] + C_r D_3[J_6 - x_3 J_{18}]\} + sin\,2\theta\,\{C_r D_1[-vJ_7 - x_3 J_{19}]$$

$$+ C_r D_2[J_6 + vJ_4 - x_3 J_{15}] + C_r D_3[-x_3 J_{17}]\}$$

$$= C_r(cos^2\,\theta\,[2vJ_8 - x_3 J_{13}] + sin^2\,\theta\,[-x_3 J_{16}]$$

$$+ sin\,2\theta\,[-vJ_7 - x_3 J_{19}])D_1$$

$$+ C_r(cos^2\,\theta\,[2J_9 - x_3 J_{14}] + sin^2\,\theta\,[-x_3 J_{17}]$$

$$+ sin\,2\theta\,[J_6 + vJ_4 - x_3 J_{15}])D_2$$

$$+ C_r(cos^2\,\theta\,[J_6 + (1-2v)J_4 - x_3 J_{15}] + sin^2\,\theta\,[J_6 - x_3 J_{18}]$$

$$+ sin\,2\theta\,[-x_3 J_{17}])D_3$$

…… (2.24)

$$\sigma_{XY}{}^{P} = \frac{1}{2} sin\, 2\beta \,\{C_r D_1[2J_8 - x_3 J_{10}] + C_r D_2[2\upsilon J_9 - x_3 J_{11}]$$

$$+ C_r D_3[J_6 + (1-2\upsilon)J_5 - x_3 J_{12}]\} - \frac{1}{2} sin\, 2\beta\, sin^2\, \theta\, \{C_r D_1[2\upsilon J_8 - x_3 J_{13}]$$

$$+ C_r D_2[2J_9 - x_3 J_{14}] + C_r D_3[J_6 + (1-2\upsilon)J_4 - x_3 J_{15}]\}$$

$$- \frac{1}{2} sin\, 2\beta\, cos^2\, \theta\, \{C_r D_1[-x_3 J_{16}] + C_r D_2[-x_3 J_{17}] + C_r D_3[J_6 - x_3 J_{18}]\}$$

$$- cos\, 2\beta\, sin\, \theta\, \{C_r D_1[(1-\upsilon)J_9 - x_3 J_{11}] + C_r D_2[(1-\upsilon)J_8 - x_3 J_{13}]$$

$$+ C_r D_3[-(1-2\upsilon)J_7 - x_3 J_{19}]\} + cos\, 2\beta\, cos\, \theta\, \{C_r D_1[J_6 + \upsilon J_5 - x_3 J_{12}]$$

$$+ C_r D_2[-\upsilon J_7 - x_3 J_{19}] + C_r D_3[-x_3 J_{16}]\}$$

$$+ \frac{1}{2} sin\, 2\beta\, sin\, 2\theta\, \{C_r D_1[-\upsilon J_7 - x_3 J_{19}] + C_r D_2[J_6 + \upsilon J_4 - x_3 J_{15}]$$

$$+ C_r D_3[-x_3 J_{17}]\}$$

$$= C_r \left(\frac{1}{2} sin\, 2\beta\, [2J_8 - x_3 J_{10}] - \frac{1}{2} sin\, 2\beta\, sin^2\, \theta\, [2\upsilon J_8 - x_3 J_{13}]\right.$$

$$- \frac{1}{2} sin\, 2\beta\, cos^2\, \theta\, [-x_3 J_{16}] - cos\, 2\beta\, sin\, \theta\, [(1-\upsilon)J_9 - x_3 J_{11}]$$

$$\left. + cos\, 2\beta\, cos\, \theta\, [J_6 + \upsilon J_5 - x_3 J_{12}] + \frac{1}{2} sin\, 2\beta\, sin\, 2\theta\, [-\upsilon J_7 - x_3 J_{19}]\right) D_1$$

$$+ C_r \left(\frac{1}{2} sin\, 2\beta\, [2\upsilon J_9 - x_3 J_{11}] - \frac{1}{2} sin\, 2\beta\, sin^2\, \theta\, [2J_9 - x_3 J_{14}]\right.$$

$$- \frac{1}{2} sin\, 2\beta\, cos^2\, \theta\, [-x_3 J_{17}] - cos\, 2\beta\, sin\, \theta\, [(1-\upsilon)J_8 - x_3 J_{13}]$$

$$\left. + cos\, 2\beta\, cos\, \theta\, [-\upsilon J_7 - x_3 J_{19}] + \frac{1}{2} sin\, 2\beta\, sin\, 2\theta\, [J_6 + \upsilon J_4 - x_3 J_{15}]\right) D_2$$

$$+ C_r \left(\frac{1}{2} sin\, 2\beta\, [J_6 + (1-2\upsilon)J_5 - x_3 J_{12}]\right.$$

$$-\frac{1}{2}sin\,2\beta\,sin^2\,\theta\,[J_6+(1-2v)J_4-x_3J_{15}]$$

$$-\frac{1}{2}sin\,2\beta\,cos^2\,\theta\,[J_6-x_3J_{18}]-cos\,2\beta\,sin\,\theta\,[-(1-2v)J_7-x_3J_{19}]$$

$$+cos\,2\beta\,cos\,\theta\,[-x_3J_{16}]+\frac{1}{2}sin\,2\beta\,sin\,2\theta\,[-x_3J_{17}]\Big)D_3$$

…… (2.25)

$$\sigma_{XZ}{}^{P} = \frac{1}{2} sin\,\beta\, sin\,2\theta\,\{C_r D_1[2vJ_8 - x_3 J_{13}] + C_r D_2[2J_9 - x_3 J_{14}]$$

$$+ C_r D_3[J_6 + (1-2v)J_4 - x_3 J_{15}]\} - \frac{1}{2} sin\,\beta\, sin\,2\theta\,\{C_r D_1[-x_3 J_{16}]$$

$$+ C_r D_2[-x_3 J_{17}] + C_r D_3[J_6 - x_3 J_{18}]\}$$

$$+ cos\,\beta\, cos\,\theta\,\{C_r D_1[(1-v)J_9 - x_3 J_{11}] + C_r D_2[(1-v)J_8 - x_3 J_{13}]$$

$$+ C_r D_3[-(1-2v)J_7 - x_3 J_{19}]\} + cos\,\beta\, sin\,\theta\,\{C_r D_1[J_6 + vJ_5 - x_3 J_{12}]$$

$$+ C_r D_2[-vJ_7 - x_3 J_{19}] + C_r D_3[-x_3 J_{16}]\}$$

$$- sin\,\beta\, cos\,2\theta\,\{C_r D_1[-vJ_7 - x_3 J_{19}] + C_r D_2[J_6 + vJ_4 - x_3 J_{15}]$$

$$+ C_r D_3[-x_3 J_{17}]\}$$

$$= C_r \left(\frac{1}{2} sin\,\beta\, sin\,2\theta\,[2vJ_8 - x_3 J_{13}] - \frac{1}{2} sin\,\beta\, sin\,2\theta\,[-x_3 J_{16}]\right.$$

$$+ cos\,\beta\, cos\,\theta\,[(1-v)J_9 - x_3 J_{11}] + cos\,\beta\, sin\,\theta\,[J_6 + vJ_5 - x_3 J_{12}]$$

$$\left. - sin\,\beta\, cos\,2\theta\,[-vJ_7 - x_3 J_{19}]\right) D_1$$

$$+ C_r \left(\frac{1}{2} sin\,\beta\, sin\,2\theta\,[2J_9 - x_3 J_{14}] - \frac{1}{2} sin\,\beta\, sin\,2\theta\,[-x_3 J_{17}]\right.$$

$$+ cos\,\beta\, cos\,\theta\,[(1-v)J_8 - x_3 J_{13}] + cos\,\beta\, sin\,\theta\,[-vJ_7 - x_3 J_{19}]$$

$$\left. - sin\,\beta\, cos\,2\theta\,[J_6 + vJ_4 - x_3 J_{15}]\right) D_2$$

$$+ C_r \left(\frac{1}{2} sin\,\beta\, sin\,2\theta\,[J_6 + (1-2v)J_4 - x_3 J_{15}]\right.$$

$$- \frac{1}{2} sin\,\beta\, sin\,2\theta\,[J_6 - x_3 J_{18}] + cos\,\beta\, cos\,\theta\,[-(1-2v)J_7 - x_3 J_{19}]$$

$$\left. + cos\,\beta\, sin\,\theta\,[-x_3 J_{16}] - sin\,\beta\, cos\,2\theta\,[-x_3 J_{17}]\right) D_3$$

…… (2.26)

$$\sigma_{YZ}{}^{P} = -\frac{1}{2}\cos\beta\,\sin 2\theta\,\{C_r D_1[2\upsilon J_8 - x_3 J_{13}] + C_r D_2[2J_9 - x_3 J_{14}]$$

$$+ C_r D_3[J_6 + (1-2\upsilon)J_4 - x_3 J_{15}]\} + \frac{1}{2}\cos\beta\,\sin 2\theta\,\{C_r D_1[-x_3 J_{16}]$$

$$+ C_r D_2[-x_3 J_{17}] + C_r D_3[J_6 - x_3 J_{18}]\}$$

$$+ \sin\beta\,\cos\theta\,\{C_r D_1[(1-\upsilon)J_9 - x_3 J_{11}] + C_r D_2[(1-\upsilon)J_8 - x_3 J_{13}]$$

$$+ C_r D_3[-(1-2\upsilon)J_7 - x_3 J_{19}]\} + \sin\beta\,\sin\theta\,\{C_r D_1[J_6 + \upsilon J_5 - x_3 J_{12}]$$

$$+ C_r D_2[-\upsilon J_7 - x_3 J_{19}] + C_r D_3[-x_3 J_{16}]\}$$

$$+ \cos\beta\,\cos 2\theta\,\{C_r D_1[-\upsilon J_7 - x_3 J_{19}] + C_r D_2[J_6 + \upsilon J_4 - x_3 J_{15}]$$

$$+ C_r D_3[-x_3 J_{17}]\}$$

$$= C_r\left(-\frac{1}{2}\cos\beta\,\sin 2\theta\,[2\upsilon J_8 - x_3 J_{13}] + \frac{1}{2}\cos\beta\,\sin 2\theta\,[-x_3 J_{16}]\right.$$

$$+ \sin\beta\,\cos\theta\,[(1-\upsilon)J_9 - x_3 J_{11}] + \sin\beta\,\sin\theta\,[J_6 + \upsilon J_5 - x_3 J_{12}]$$

$$\left.+ \cos\beta\,\cos 2\theta\,[-\upsilon J_7 - x_3 J_{19}]\right) D_1$$

$$+ C_r\left(-\frac{1}{2}\cos\beta\,\sin 2\theta\,[2J_9 - x_3 J_{14}] + \frac{1}{2}\cos\beta\,\sin 2\theta\,[-x_3 J_{17}]\right.$$

$$+ \sin\beta\,\cos\theta\,[(1-\upsilon)J_8 - x_3 J_{13}] + \sin\beta\,\sin\theta\,[-\upsilon J_7 - x_3 J_{19}]$$

$$\left.+ \cos\beta\,\cos 2\theta\,[J_6 + \upsilon J_4 - x_3 J_{15}]\right) D_2$$

$$+ C_r\left(-\frac{1}{2}\cos\beta\,\sin 2\theta\,[J_6 + (1-2\upsilon)J_4 - x_3 J_{15}]\right.$$

$$+ \frac{1}{2}\cos\beta\,\sin 2\theta\,[J_6 - x_3 J_{18}] + \sin\beta\,\cos\theta\,[-(1-2\upsilon)J_7 - x_3 J_{19}]$$

$$\left.+ \sin\beta\,\sin\theta\,[-x_3 J_{16}] + \cos\beta\,\cos 2\theta\,[-x_3 J_{17}]\right) D_3$$

…… (2.27)

From Eqs. (2.21) to (2.26), we have $D_1 = D_{SL}, D_2 = D_{SH}, D_3 = D_{NN}$.

2.1.2 Non-dimensionalization

It is of great importance to consider the non-dimensionlization for 3D DDM. We firstly selected a fracture height H as the reference length and the non-dimensional coordinates would be written as,

$$\tilde{x}_1 = \frac{1}{\mathrm{H}} x_1, \ \ \tilde{x}_2 = \frac{1}{\mathrm{H}} x_2, \ \ \tilde{x}_3 = \frac{1}{\mathrm{H}} x_3 \tag{2.28}$$

Then a reference pressure P was chosen to do non-dimensionalization for the three components of stresses as,

$$\tilde{\sigma}_{SL} = \frac{1}{P}\sigma_{SL}, \ \ \tilde{\sigma}_{SH} = \frac{1}{P}\sigma_{SH}, \ \ \tilde{\sigma}_{NN} = \frac{1}{P}\sigma_{NN} \tag{2.29}$$

Three components of non-dimensional displacement discontinuities were written as below,

$$\widetilde{D}_{SL} = \frac{E}{HP} D_{SL}, \ \ \widetilde{D}_{SH} = \frac{E}{HP} D_{SH}, \ \ \widetilde{D}_{NN} = \frac{E}{HP} D_{NN} \tag{2.30}$$

where E is the Young's modulus.

According to the coordinate transformation, we can determine the normalized induced normal stress $\tilde{\sigma}_{NN}$ and shear stresses $\tilde{\sigma}_{SL}$, $\tilde{\sigma}_{SH}$ for a given element by summarizing contributions of normalized displacement discontinuities of all N elements, as shown,

$$\tilde{\sigma}_{SL}^{i} = \sum_{j=1}^{N} \tilde{A}_{SL,SL}^{ij} \widetilde{D}_{SL}^{j} + \sum_{j=1}^{N} \tilde{A}_{SL,SH}^{ij} \widetilde{D}_{SH}^{j} + \sum_{j=1}^{N} \tilde{A}_{SL,NN}^{ij} \widetilde{D}_{NN}^{j}$$

$$\tilde{\sigma}_{SH}^{i} = \sum_{j=1}^{N} \tilde{A}_{SH,SL}^{ij} \widetilde{D}_{SL}^{j} + \sum_{j=1}^{N} \tilde{A}_{SH,SH}^{ij} \widetilde{D}_{SH}^{j} + \sum_{j=1}^{N} \tilde{A}_{SH,NN}^{ij} \widetilde{D}_{NN}^{j}$$

$$\tilde{\sigma}_{NN}^{i} = \sum_{j=1}^{N} \tilde{A}_{NN,SL}^{ij} \widetilde{D}_{SL}^{j} + \sum_{j=1}^{N} \tilde{A}_{NN,SH}^{ij} \widetilde{D}_{SH}^{j} + \sum_{j=1}^{N} \tilde{A}_{NN,NN}^{ij} \widetilde{D}_{NN}^{j}$$

…… (2.31)

We can reformulated Eq. (2.31) as a non-dimensional form,

$$\begin{bmatrix} \tilde{\sigma}_{SL}^{i} \\ \tilde{\sigma}_{SH}^{i} \\ \tilde{\sigma}_{N}^{i} \end{bmatrix} = \begin{bmatrix} \tilde{A}_{SL,SL}^{ij} & \tilde{A}_{SL,SH}^{ij} & \tilde{A}_{SL,NN}^{ij} \\ \tilde{A}_{SH,SL}^{ij} & \tilde{A}_{SH,SH}^{ij} & \tilde{A}_{SH,NN}^{ij} \\ \tilde{A}_{NN,SL}^{ij} & \tilde{A}_{NN,SH}^{ij} & \tilde{A}_{NN,NN}^{ij} \end{bmatrix} \begin{bmatrix} \widetilde{D}_{SL}^{j} \\ \widetilde{D}_{SH}^{j} \\ \widetilde{D}_{NN}^{j} \end{bmatrix},$$

…… (2.32)

where $\widetilde{D}_{SL}^{j}$ is the normalized shear displacement discontinuity of element *j* in the fracture length direction, $\widetilde{D}_{SH}^{j}$ is the normalized shear displacement discontinuity of element *j* in the fracture height direction, $\widetilde{D}_{NN}^{j}$ is the normalized normal displacement discontinuity of element *j*. Moreover, $\tilde{\sigma}_{SL}^{i}, \tilde{\sigma}_{SH}^{i}, \tilde{\sigma}_{NN}^{i}$ are normalized normal stress and normalized shear stresses in fracture length and height directions at element *i*, respectively. Based on a given stress boundary condition on fractures, normalized displacement discontinuities can be calculated using Eq. (2.32).

2.1.3 Flowchart of 3D DDM

Figure 2.3 describes the flowchart of our rock deformation model. First, we did fracture discretization, which meshed the target fractures with prescribed boundary elements, then we made coordinate transformation and stress tensor transformation, which considering fractures with arbitrary strike angle and dip angle in three dimensions. Next, we determined the stresses on the boundary condition and then obtained the influence

coefficient matrix. Finally, a solver was applied to calculate the three normalized displacement discontinuities.

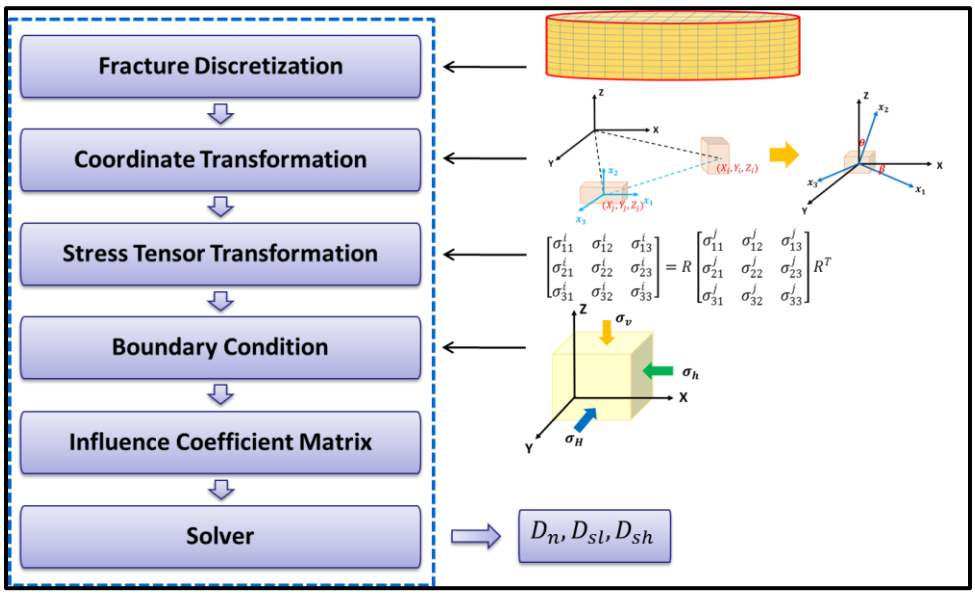

Figure 2.3: Flowchart of our rock deformation model based on 3D DDM

2.2 Model Validation

2.2.1 Comparison with an Analytical Solution

3D DDM can be utilized to calculate displacement discontinuities and induced stresses for fractures. To validate the 3D model with a 2D analytical solution, we calculated normal displacement discontinuity and induced stresses for a plane-strain fracture using both methods. Parameters of a plane-strain vertical fracture are given in Table 2.1. To satisfy the assumption of plane-strain on the vertical plane, the total fracture length is 2000 ft, which is much larger than the fracture height. The analytical solution of

opening along a fracture (Sneddon 1951; Crouch and Starfield 1983) can be written as,

$$w = u(x, 0^-) - u(x, 0^+) = -\frac{2Pb(1-\nu)}{G}\sqrt{1-\frac{x^2}{b^2}} \tag{2.33}$$

where P is the net pressure within the fracture, b is half length of the fracture, x is the location along the fracture length.

Comparison of the normal displacement discontinuity is shown in Figure 2.4, which illustrates that the solution given by 3D DDM shows good agreement with the 2D analytical solution. The fracture width decreases from the fracture center to the tips. Figure 2.5 indicates induced stresses normal to the vertical fracture plane at the center of the fracture. The solid lines represent the solution by 3D DDM and the dashed lines represent the 2D analytical solution. The normal horizontal stress is the stress normal to the vertical fracture plane, the lateral horizontal stress is the stress along the fracture length direction, and the vertical stress is the stress along the fracture height direction. With the increment of the distance normal to the fracture, induced stresses attenuate along the center line. The induced stresses reach their maximum values on the fracture. The lateral horizontal stress is the product of Poisson's ratio and the sum of the normal horizontal stress and the vertical stress. The numerical solution from 3D DDM has a good match with the 2D analytical solution as shown in the figures.

Parameter	Value	Unit
Vertical fracture length	2000	ft
Vertical fracture height	100	ft
Net pressure	1500	psi
Young's modulus	3.00E+06	psi
Poisson's ratio	0.25	

Table 2.1− Parameters of a vertical fracture for validation.

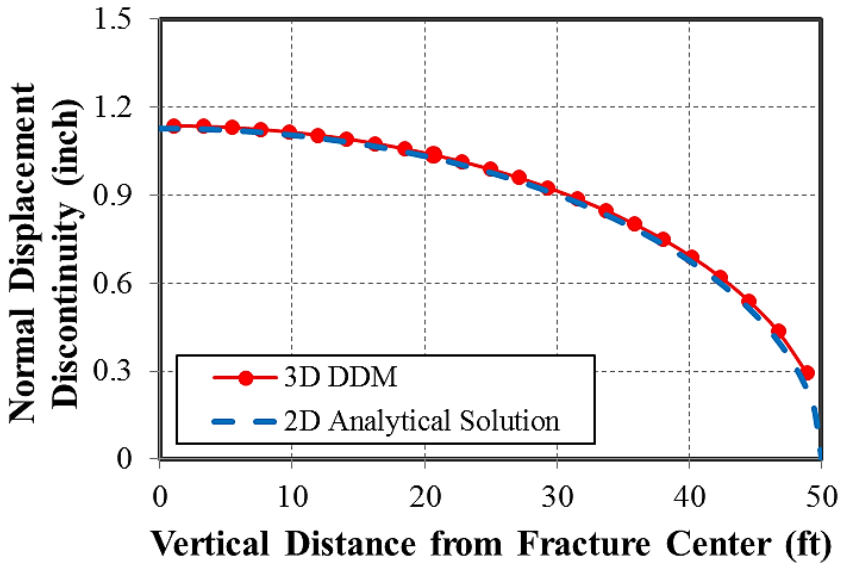

Figure 2.4: Normal displacement discontinuity along vertical direction starting from fracture center (Tang et al. 2017).

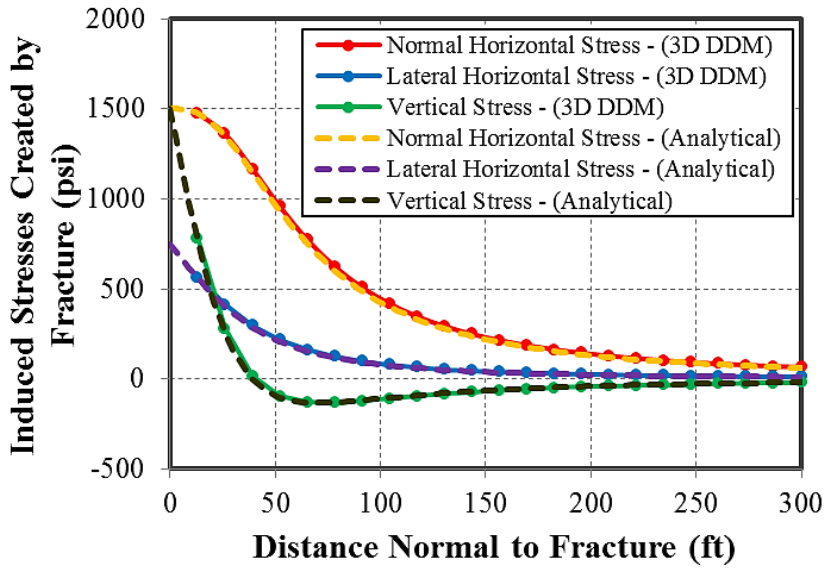

Figure 2.5: Induced stresses normal to the vertical fracture (Tang et al. 2017).

2.2.2 Comparison between Horizontal and Vertical Fractures

The dimension of a vertical fracture is shown in Figure 2.6 (a) and the vertical fracture was rotated 90^{o} to be a horizontal fracture as described in Figure 2.6 (b). The two fractures have identical fracture geometry and net pressure. The parameters are given in Table 2.2. The normal displacement discontinuity (i.e. fracture width) of both vertical and horizontal fractures were calculated using 3D DDM and shown in Figure 2.7 and Figure 2.8. Due to the fact of the same dimension and net pressure within fractures for the two cases, the calculated fracture width should be identical after coordinate transformation. Figure 2.7 illustrates width profile along the shorter dimension (100 ft) for both vertical and horizontal fractures and shows that the width is exactly the same for both cases. Figure 2.8 gives width profile along the dimension of 400 ft and also shows identical width for both fractures, as can be theoretically expected. Through this comparison study, we further

validated our model and proved that 3D DDM can be used to calculate displacement discontinuities for fractures in 3D space.

Parameter	Value	Unit
Vertical fracture length	400	ft
Vertical fracture height	100	ft
Horizontal fracture length in x direction	400	ft
Horizontal fracture length in y direction	100	ft
Net pressure within fractures	1000	psi

Table 2.2−Five required parameters of a single fracture case.

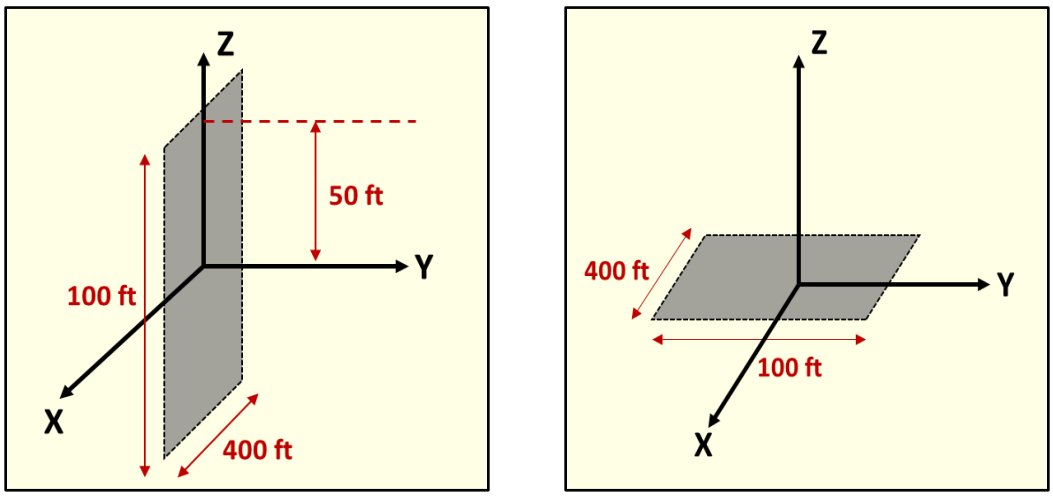

Figure 2.6: Sketch of vertical and horizontal fractures with the same dimension - (a). Dimension of a vertical fracture and (b). Dimension of a horizontal fracture (Tang and Wu 2018).

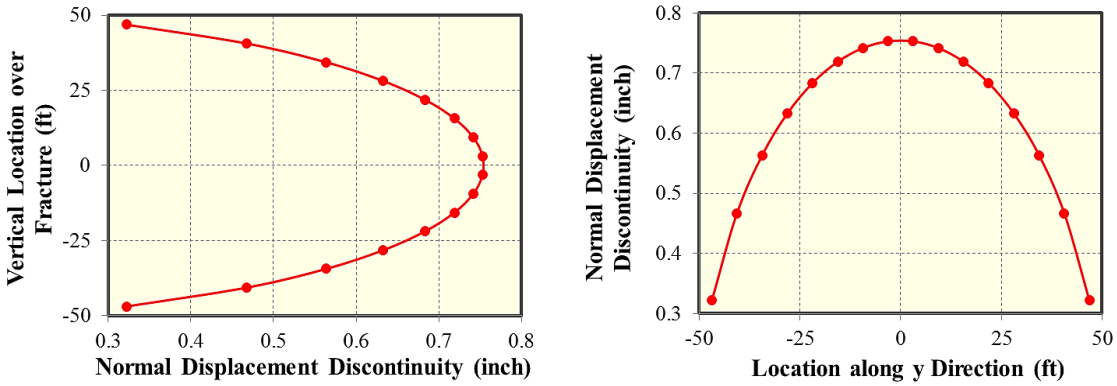

Figure 2.7: (a). Normal displacement discontinuity of the vertical fracture along the z direction; (b). Normal displacement discontinuity of the horizontal fracture along the y direction (Tang and Wu 2018).

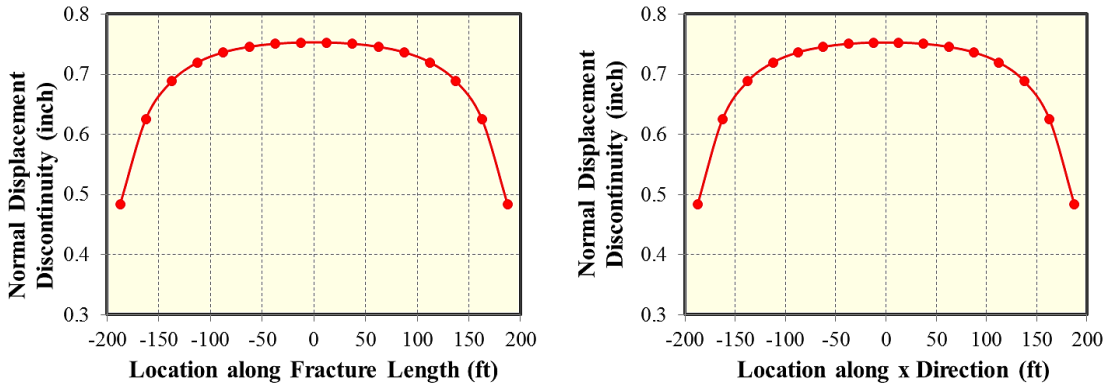

Figure 2.8: (a). Normal displacement discontinuity of the vertical fracture along the x direction; (b). Normal displacement discontinuity of the horizontal fracture along the x direction (Tang and Wu 2018).

2.3 Different Fracture Geometry Analysis

The fully 3DDDM can deal with the mechanical interaction between hydraulic fractures and pre-existing discontinuities such as weakly bedding planes, joints or veins in 3D space. The cases of different fracture geometries show how to calculate the fracture opening and shear displacements of the horizontal interfaces, which help to analyze the

sliding along the horizontal interface, fracture re-initiation from the horizontal interface and also the diversion of viscous fluid flow at fracture junctions if a coupled fracture propagation model is developed (Chuprakov et al. 2013), and further estimate the fracture height containment. In this section, different fracture geometries were prescribed with the combination of vertical and horizontal fractures to investigate the effects of opening interfaces on fracture geometry. Cases of a symmetric crossing-shaped fracture, a T-shaped fracture, an I-shaped fracture and a complex fracture geometry with offsets were analyzed. Young's modulus and Poisson's ratio used in all cases are 3.0E6 psi and 0.25, respectively.

2.3.1 Symmetric Crossing-shaped Fracture Geometry

In this subsection, we assembled vertical and horizontal fractures together to investigate effects of an opening interface. A horizontal fracture represents a weak interface and is opened and crossed by a vertical fracture. A symmetric crossing-shaped fracture is shown in Figure 2.9. All required parameters are listed in Table 2.3. Generally, the overburden vertical stress is larger than the minimum horizontal stress in unconventional reservoirs. We assumed uniform fluid pressure within vertical and horizontal fractures, which implies that net pressure within fractures is different. In this section, it is assumed that net pressure within the vertical fracture is 1000 psi, while the net pressure within the horizontal fractures is 500 psi. Additionally, "DNN" represents the normal displacement discontinuity of vertical fractures, and the normal displacement discontinuity of horizontal fractures is abbreviated to "NDD" in all figures.

Normalized width profiles of the vertical fracture along the fracture height direction and the length direction are given in Figures 2.10 (a) and 2.10 (b). The red color represents the width profile of the vertical fracture in the case of symmetric crossing-shaped fracture (Figure 2.9) under the influence of a horizontal fracture. “DNN-Single” means the width profile of a single vertical fracture without the effect of a horizontal fracture. The net pressure within this single vertical fracture is the same as in the vertical fracture in Figure 2.9. Figures 2.10 (a) and 2.10 (b) show that the normalized width of the vertical fracture under the effect of a horizontal fracture is relatively smaller than that of a single vertical fracture. According to Figure 2.12 (b), the induced normal stress acting on normalized x-z plane (σ_{yy}) generated by the horizontal fracture, behaves as a compressive stress in the region of the vertical fracture (x axis is from -2 to 2, z axis is from -0.5 to 0.5). Because of additional compressive stress exerted on the vertical fracture, fracture width is reduced in the case of symmetric crossing-shaped fracture. Moreover, the maximum fracture width is obtained at the fracture center no matter which direction we chose.

Figures 2.11 (a) and 2.11 (b) show the normalized displacement discontinuities of the horizontal fracture along x and y directions, respectively. “NDD-Single” represents the width of a single horizontal fracture without the influence of the vertical fracture and has the same net pressure with the horizontal fracture in Figure 2.9. “SDD-X” and “SDD-Y” are shear displacement discontinuities of the horizontal fracture in x and y directions, respectively. From Figures 2.11 (a) and 2.11 (b), the opening of the horizontal fracture under the effect of the vertical fracture is also less than the opening of a single horizontal

fracture, as a result of compressive stress induced by the vertical fracture (Figure 2.12 (a)). When a horizontal fracture is totally symmetrical with a vertical fracture as depicted in Figure 2.9, shear displacement discontinuities of this horizontal fracture are zero in both x and y directions. In x direction, the fracture width decays with farther distance from x = 0. The minimum width is obtained at the fracture tip. Generally, fracture width monotonically decreases from fracture center to a tip for the single fracture case. However, Figure 2.11 (b) presents a new perspective about width distribution of a horizontal fracture under the influence of a vertical fracture. The stress contour map in Figure 2.12 (a) can be used to make an explanation, which shows the additional normal stress acting on normalized x-y plane (σ_{zz}) induced by the vertical fracture. The induced normal stress is negative (tensile stress) from y = -1.0 to y = -0.5. Then it becomes positive (compressive stress) in the range of y = -0.5 to y = 0.5. The sign of the stress changes to negative again from y = 0.5 to y = 1.0. Thus, the formation of fracture width "trough" is due to the positive induced normal stress which behaves as a compressive stress acting on the middle section of the horizontal fracture.

Parameter	Value	Unit
Vertical fracture length	400	ft
Vertical fracture height	100	ft
Net pressure for vertical fracture	1000	psi
Horizontal fracture length in x direction	400	ft
Horizontal fracture length in y direction	200	ft
Net pressure for horizontal fracture	500	psi

Table 2.3−Six required parameters of a symmetric crossing-shaped fracture case.

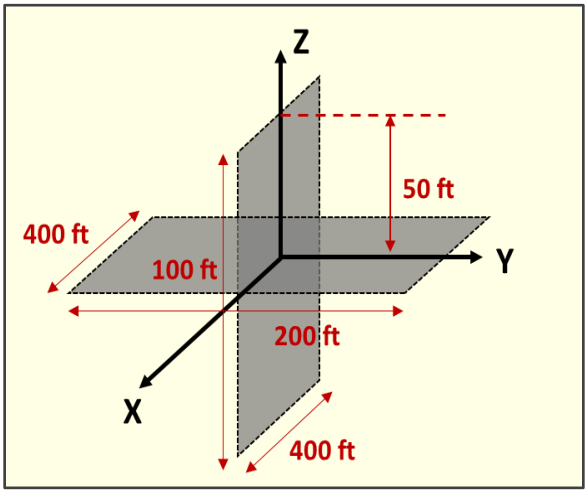

Figure 2.9: The dimension of a symmetric crossing-shaped fracture (Tang and Wu 2018).

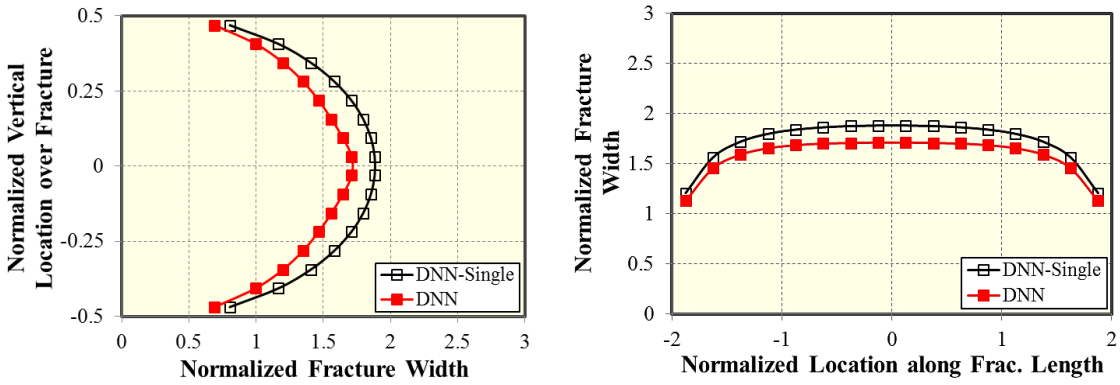

Figure 2.10: (a). Normalized normal displacement discontinuity of the vertical fracture along the z direction; (b). Normalized normal displacement discontinuity of the vertical fracture along the x direction (Tang and Wu 2018).

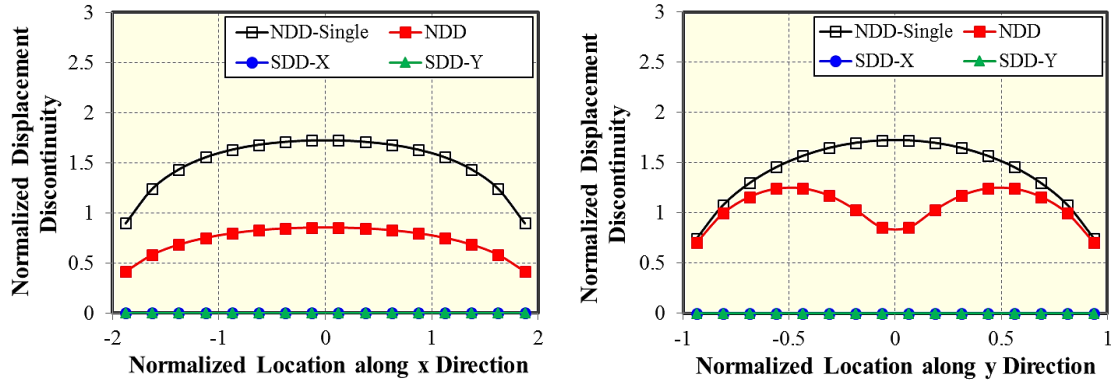

Figure 2.11: (a). Normalized displacement discontinuities of the horizontal fracture along the x direction; (b). Normalized displacement discontinuities of the horizontal fracture along the y direction (Tang and Wu 2018).

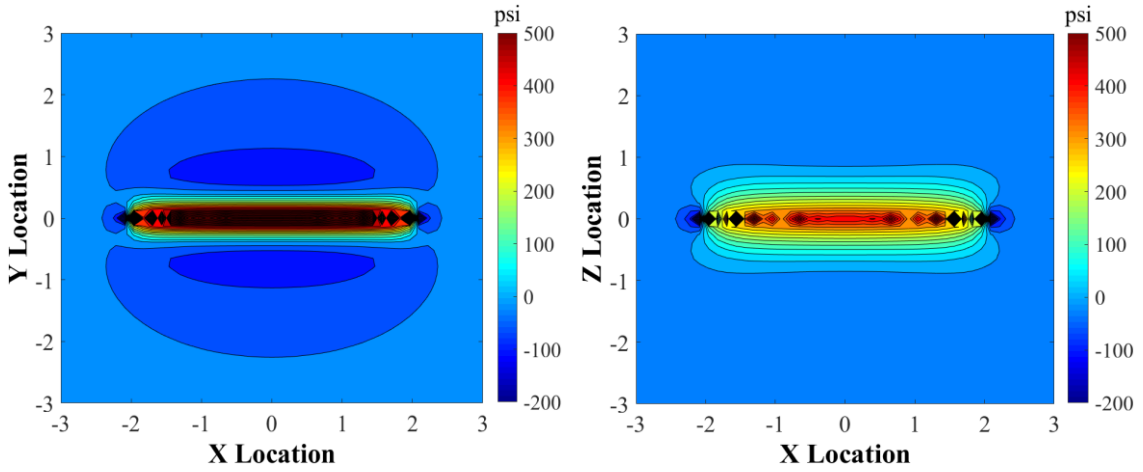

Figure 2.12: (a). Normal stress (σ_{zz}) acting on normalized x-y plane induced by the vertical fracture; (b). Normal stress (σ_{yy}) acting on normalized x-z plane induced by the horizontal fracture (Tang and Wu 2018).

2.3.2 T-shaped Fracture Geometry

In this case, we combined a vertical fracture and a horizontal fracture together to create two types of fracture geometries illustrated in Figures 2.13 (a) and 2.13 (b). Figure 2.13 (a) shows an asymmetric crossing-shaped fracture and Figure 2.13 (b) presents a T-shaped fracture. Combined with the symmetric crossing-shaped fracture in the second case, there are three different fracture geometries. The only difference among them is the distance between the wellbore location and the horizontal fracture, which plays a significant role in determining the step-overs mechanism of the vertical fracture when it contacts with the weakly bedding interface. The horizontal fracture is regarded as opening of a bedding interface and the vertical fracture would either be arrested or step over the interface. A concept named interfacial sliding distance is studied in this case. All required parameters for this case are the same with the parameters in Table 2.3.

Figure 2.14 (a) shows the normalized width profiles of the vertical fracture along the vertical direction for three fracture geometries: a symmetric crossing-shaped fracture, an asymmetric crossing-shaped fracture, and a T-shaped fracture. The case of a symmetric crossing-shaped fracture (Figure 2.9) is regarded as a reference for the analysis of displacement discontinuities. When the vertical fracture intersects with a weak interface in the case of asymmetric crossing-shaped fracture, shear displacements are induced on the interface and result in a jump of fracture width on the vertical fracture at the crossing position of the interface (z = 0.25). This width jump can be defined as interfacial sliding distance which can be quantified by 3D DDM. For this case, width of the vertical fracture begins to increase from bottom location (z = -0.5) and reaches its maximum value at the location of the bedding interface (z = 0.25). A decrement of fracture width begins from the interface position to the upper tip of the vertical fracture (z = 0.5). Previously some researchers studied the physical mechanisms of the formation of T-shaped fractures (Chuprakov and Prioul 2015; Li et al. 2018a; Li et al. 2018b). In the T-shaped geometry, the vertical fracture is arrested by the weak horizontal interface. Width of the vertical fracture monotonically increases from the bottom position (z = -0.5) to the position at the weak interface (z = 0.5). From Figure 2.14 (a), we can observe that width of the vertical fracture along fracture height increases with the increment of distance between the horizontal interface and the center of the vertical fracture. Figure 2.14 (b) also indicates that the normalized width profile of the vertical fracture along fracture length at z = 0 has a positive correlation with the distance between the vertical fracture center and the weak interface.

All results above can be explained by the shear displacement discontinuities of the horizontal fracture segment. Figure 2.11 (b)**,** Figures 2.15 (b) and 2.15 (d) illustrate shear displacement discontinuities of the horizontal fracture along the y direction for a symmetric crossing-shaped fracture, an asymmetric crossing-shaped fracture, and a T-shaped fracture, respectively. The difference among these three fracture geometries is the distance between the center of the vertical fracture and the weak horizontal interface. The width profile of the vertical fracture for the case of a symmetric crossing-shaped fracture is continuous at the location of the horizontal interface due to zero shear displacement discontinuities along the horizontal segment (Figure 2.11 (b)). When the location of the weak interface moves to z = 0.25, a jump of vertical fracture width is induced at the interface due to the non-zero shear displacement discontinuity (i.e. SDD-Y) (Figure 2.15 (b)). As the weak interface approximates z = 0.5, the shear displacement discontinuity continues increasing. The maximum SDD-Y is obtained when a T-shaped fracture forms. Moreover, the interfacial sliding distance also reaches its maximum in the case of the T-shaped fracture. SDD-Y of the horizontal fracture segment along the y direction is used to determine the interfacial sliding distance along the horizontal interface and the width profile of the vertical fracture along the height direction.

The normalized width profiles of vertical fractures along the dimension of 400 ft are delineated in Figure 2.14 (b). Along this direction, each fracture geometry obtains its minimum width at the fracture tip and maximum value at the center of the fracture. Additionally, we observe that the symmetric crossing-shaped fracture case has the smallest fracture width compared with the other two cases. Figures 2.15 (a) through 2.15 (d)

illustrate normalized displacement discontinuities of horizontal fractures for the asymmetric crossing-shaped geometry, the T-shaped geometry and a single fracture geometry, respectively. It's worth mentioning that the horizontal fracture in the single fracture geometry has the same net pressure (500 psi) with the net pressure of the horizontal fracture in the other two geometries. From the figures, we find that the width profiles of a single horizontal fracture in both x and y directions are larger than that of the other two geometries, which having a similar trend with the results in Figures 2.11 (a) and 2.11 (b). In addition, the T-shaped geometry has a larger shear displacement discontinuities (SDD-X and SDD-Y) in comparison with the asymmetric crossing-shaped geometry.

In this case, we investigated the effect of the distance between the vertical fracture center and the horizontal interface, which is equivalent to the distance between the wellbore location and the interface during hydraulic fracture treatments. The larger the interfacial sliding distance, the more difficult the vertical fracture continues to propagate, which implies that the vertical fracture tends to be arrested by the interface when the wellbore is far away from the interface. Hence, if a hydraulic fracture intends to cross an interface and grows into the upper layer, the injection location should be closer to the interface.

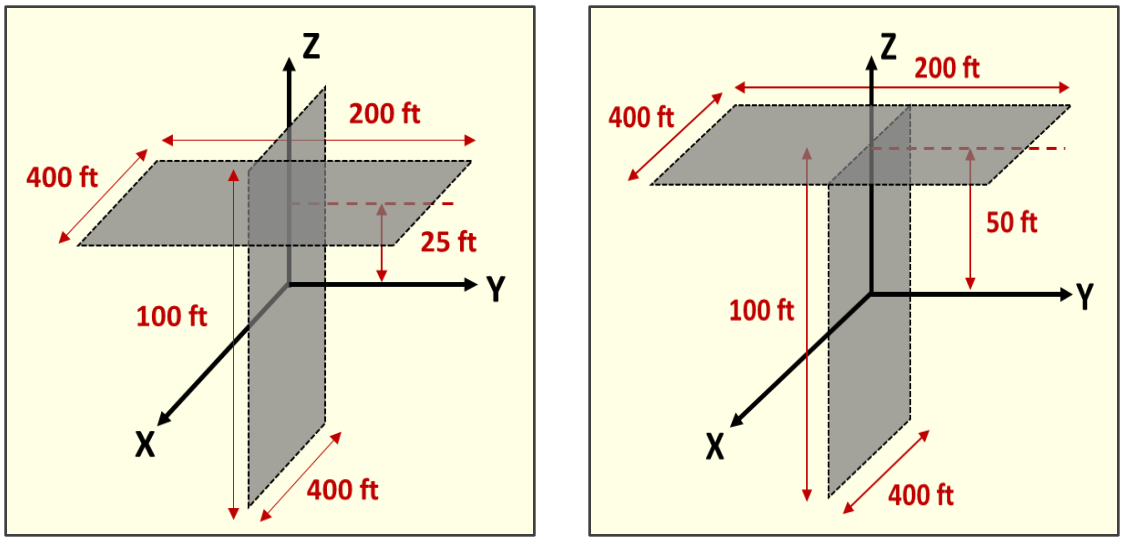

Figure 2.13: The dimension of an asymmetric crossing-shaped fracture and a T-shaped fracture - (a). Dimension of an asymmetric crossing-shaped fracture; (b). Dimension of a T-shaped fracture (Tang and Wu 2018).

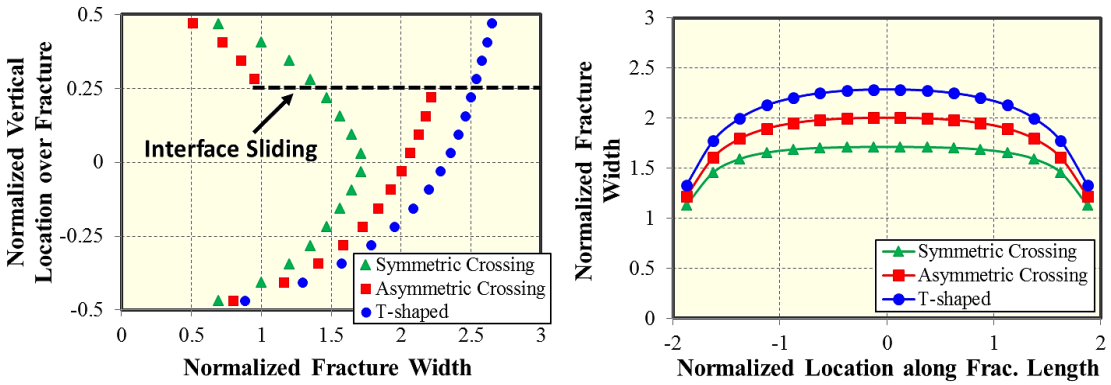

Figure 2.14: (a). Normalized normal displacement discontinuity of the vertical fracture along the z direction; (b). Normalized normal displacement discontinuity of the vertical fracture along the x direction (Tang and Wu 2018).

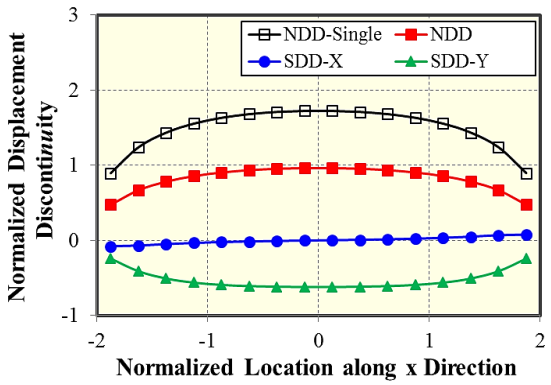

(a). Asymmetric crossing-shaped fracture – normalized displacement discontinuities of the horizontal fracture along the x direction.

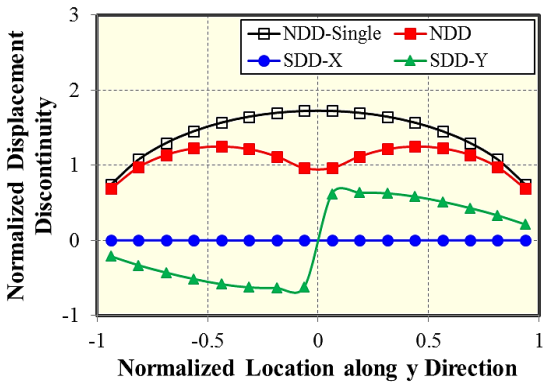

(b). Asymmetric crossing-shaped fracture – normalized displacement discontinuities of the horizontal fracture along the y direction

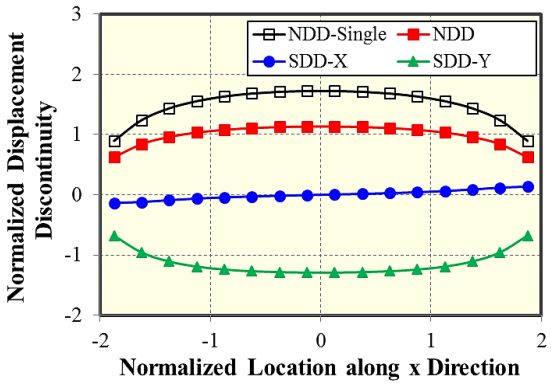

(c). T-shaped fracture – normalized displacement discontinuities of the horizontal fracture along the x direction.

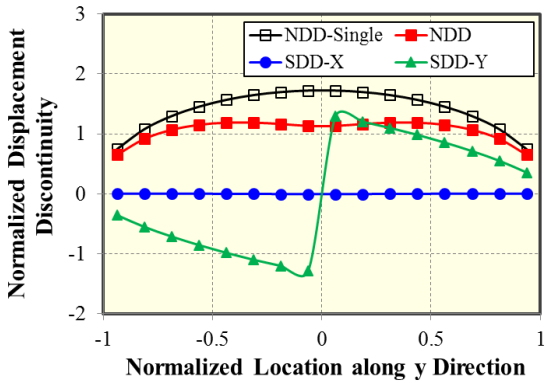

(d). T-shaped fracture – normalized displacement discontinuities of the horizontal fracture along the y direction.

Figure 2.15: Normalized displacement discontinuities of horizontal fractures in Figure 2.14 (Tang and Wu 2018).

The schematic diagram of the asymmetric crossing-shaped geometry could be depicted in Figure 2.16 (a). This figure shows a vertical fracture interacts with a weak horizontal interface and then steps over it. The fracture tip is arrested by the interface until

sufficient elastic strain energy is accumulated for crossing the interface (Chuprakov and Prioul 2015). During this process, some energy would be used for the shear sliding along the horizontal interface. Directions of sliding along two faces of the horizontal interface are labeled as the red arrows in Figure 2.16 (b). The face at the lower side of the interface behaves as outward sliding, while the face at the upper side slips inward. Therefore, the opening of vertical fracture at the lower side of the interface would increase, while at the upper side the vertical fracture width is reduced. This is why a jump of fracture width is generated in the vertical fracture. This width reduction above the weak interface can hinder fracture height growth, which regards as a primary mechanism of fracture height containment.

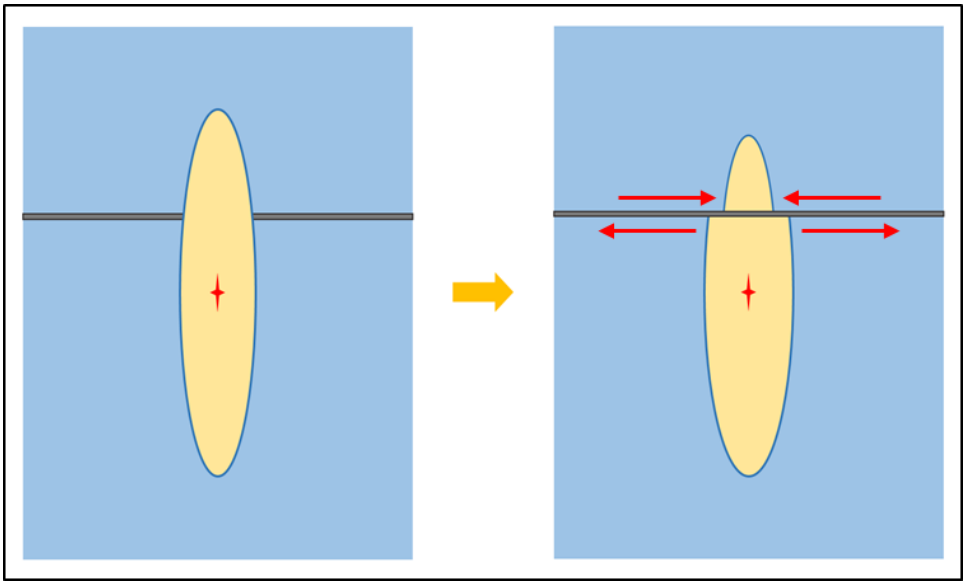

Figure 2.16: Schematic diagram of a vertical fracture interacted with a weak horizontal interface. (a). Without considering the shear sliding along the horizontal interface; (b). Consider the shear sliding along the horizontal interface (Tang and Wu 2018).

2.3.3 I-shaped Fracture Geometry

The formation pervasively contains multiple bedding layers with stress and modulus contrast. Hence, analysis of a static fracture geometry with multiple horizontal interfaces would provide a more reliable guideline for explaining the physical mechanisms of step-overs, sliding, and branching when the vertical fracture contacts with the bedding interfaces. Compared with the third case, one more horizontal fracture was added. An I-shaped fracture consists of one vertical fracture and two horizontal fractures (upper and lower horizontal fractures). The parameters for this case is the same with the parameters in the third case. For upper and lower horizontal fractures, the geometric dimension and net pressure within the fracture are the same. Figure 2.17 shows two different fracture geometries**,** a symmetric crossing-shaped fracture with two horizontal segments and an I-shaped fracture. Normalized normal displacement discontinuity of the vertical fracture along the dimension of 100 ft is illustrated in Figure 2.18 (a), which includes three fracture geometries: a symmetric crossing-shaped geometry with one horizontal segment (Figure 2.9), a symmetric crossing-shaped geometry with two horizontal segments and an I-shaped geometry. The symmetric crossing-shaped geometry with one horizontal segment is regarded as a referential geometry. Figures 2.18 (a) and 2.18 (b) indicates that the width profile of the vertical fracture in the referential geometry is smaller compared to the other two fracture geometries.

For the symmetric crossing-shaped geometry with two horizontal segments, the upper and lower horizontal fractures are located at z = 0.25 and z = -0.25, respectively. At these two locations, a jump of fracture width is observed. In this geometry, the upper and

lower horizontal fractures are regarded as two symmetric horizontal interfaces and the vertical fracture would step over these two interfaces after enough elastic strain energy has been built up. The interfacial sliding distance at two given interfaces is identical and is almost half the maximum width of the vertical fracture from the calculated results by 3D DDM. For I-shaped geometry, both tips of the vertical fracture are arrested by the two symmetric horizontal interfaces. The fracture termination is caused by the enhanced interface sliding, which dissipates energy for propagating through the interface. The fracture width almost has no change along the vertical direction as a result of the outward interface sliding along two horizontal segments.

From Figures 2.18 (a) and 2.18 (b), we can observe that the vertical fracture width in the I-shaped geometry is larger than that of the crossing-shaped geometry because of larger shear displacement discontinuity of the horizontal fracture along the y direction (SDD-Y) as illustrated in Figures 2.19 (b) and 2.19 (d). The previous case indicates that SDD-Y has a positive correlation with the distance between the horizontal fracture segment and the center of the vertical fracture. Hence, SDD-Y reaches its maximum value when the vertical fracture is arrested by the horizontal interface.

Figures 2.19 (a) through 2.19 (d) illustrate normalized displacement discontinuities of the upper horizontal fracture for a symmetric crossing-shaped fracture with two horizontal segments, an I-shaped fracture, and a single horizontal fracture, respectively. The single horizontal fracture has the same net pressure (500 psi) with the net pressure of the horizontal fracture as in the other two fracture geometries. We find that the width profiles of the single horizontal fracture in both x and y directions are larger than that of

the other two fracture geometries, which is similar with Figures 2.15 (a) through 2.15 (d). In Figure 2.19, the upper horizontal fracture in the I-shaped geometry has larger displacement discontinuities in both x and y directions compared with the symmetric crossing-shaped geometry. Above results are due to the reason that fracture termination by weak horizontal interfaces depletes more strain energy for sliding along the interfaces, and thus a larger interfacial sliding distance would be created. The symmetric crossing-shaped fracture would consume more energy for initiating new fracture from the horizontal interface and less energy would be used for interface sliding. The width profiles of the vertical fracture for the two different geometries are also used to validate the results above.

Only normalized displacement discontinuities of the upper horizontal fracture are shown in Figure 2.19. The plots of normalized displacement discontinuities of lower horizontal fracture are not shown in this case due to the fact that the lower and upper horizontal fractures have the identical absolute value of shear displacement discontinuities, but opposite direction.

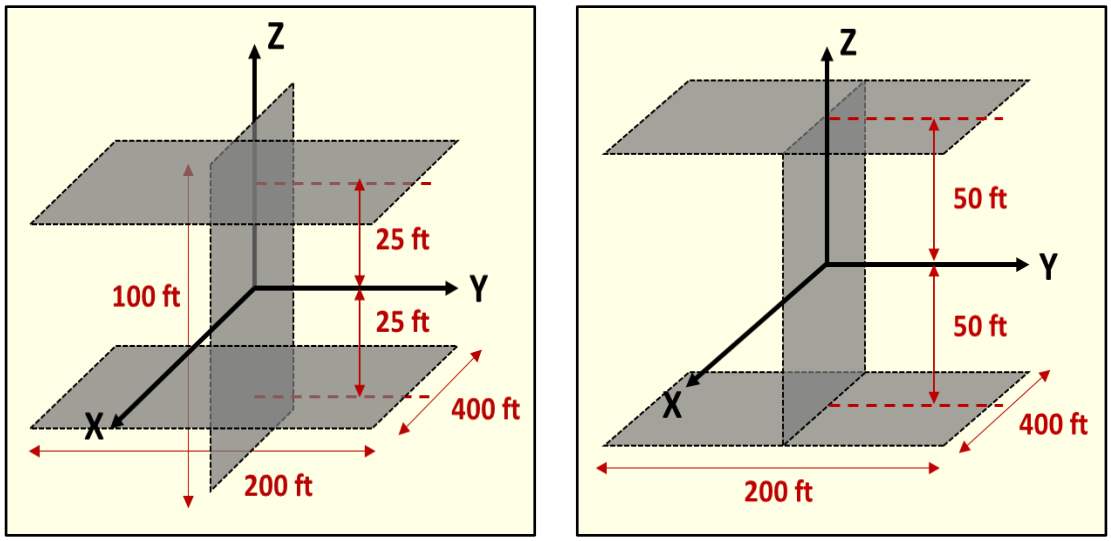

Figure 2.17: The dimension of a symmetric crossing-shaped fracture and an I-shaped fracture. (a) The dimension of a symmetric crossing-shaped fracture; (b). The dimension of I-shaped fracture (Tang and Wu 2018).

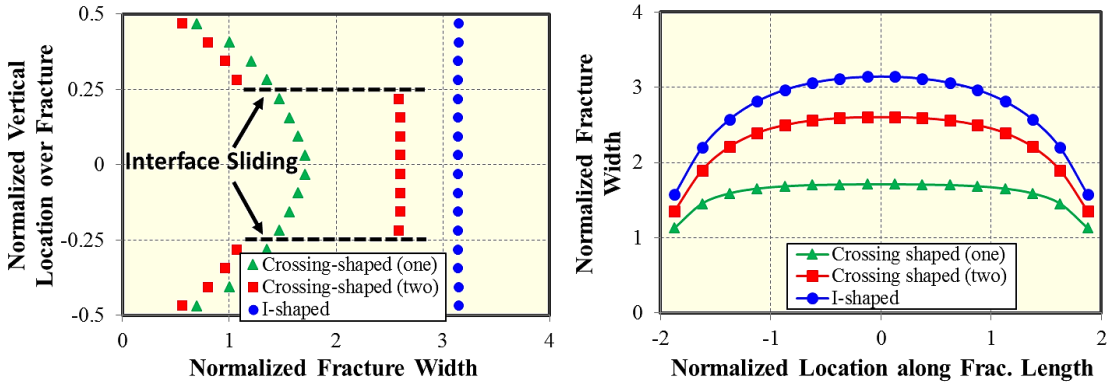

Figure 2.18: (a). Normalized normal displacement discontinuity of vertical fracture along the z direction; (b). Normalized normal displacement discontinuity of vertical fracture along the x direction (Tang and Wu 2018).

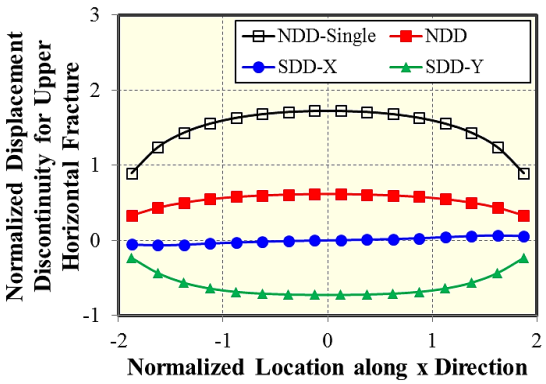

(a). Symmetric crossing-shaped fracture with two horizontal fracture segments - normalized displacement discontinuities of the upper horizontal fracture along the x direction.

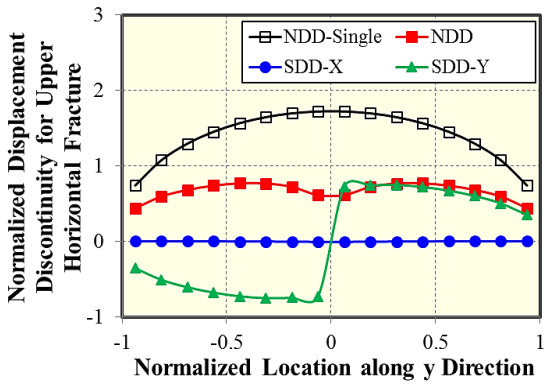

(b). Symmetric crossing-shaped fracture with two horizontal fracture segments - normalized displacement discontinuities of the upper horizontal fracture along the y direction.

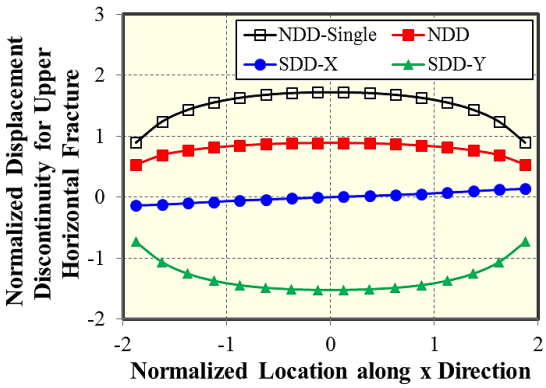

(c). I-shaped fracture - normalized displacement discontinuities of the upper horizontal fracture along the x direction.

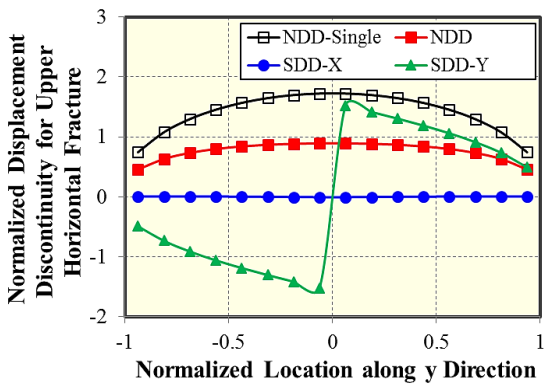

(d). I-shaped fracture - normalized displacement discontinuities of the upper horizontal fracture along the y direction.

Figure 2.19: Normalized Displacement discontinuities of the upper horizontal fracture (Tang and Wu 2018).

2.3.4 Complex Fracture Geometry with Offsets

When fracture propagates vertically and contacts with horizontal interfaces, ledges or offsets would be created along interfaces. In this case, a complex fracture geometry

with offsets is combined with five vertical fractures and two horizontal fractures, as depicted in Figure 2.20. The vertical fracture in the middle of the prescribed geometry is called the central vertical fracture, with the length as 400 ft and the height as 100 ft. The other four vertical fractures on the edge are called up-left, up-right, down-left and down-right vertical fracture, respectively. These four vertical fractures have the same geometric dimension: fracture length is 400 ft and fracture height is 50 ft. The two horizontal fractures with identical dimension are named as upper horizontal fracture and lower horizontal fracture. Additionally, net pressure within all vertical fractures is 1000 psi and net pressure within all horizontal fractures is 500 psi. In Figure 2.20, the lateral distance between the central vertical fracture and any vertical fractures on the side is defined as the offset, which is prescribed as 100 ft in this case.

The normalized width profile of down-right, central, and up-right vertical fractures along the vertical direction is given in Figure 2.21, which illustrates that average fracture width of the central vertical fracture is much larger than that of vertical fractures on the edge, as a result of large shear displacements of the horizontal fracture along the y direction. Considering the symmetry of this complex fracture geometry, Figure 2.22 only shows normalized displacement discontinuities of the fractures above the upper horizontal fracture, which include the up-left vertical fracture, the up-right vertical fracture and the upper horizontal fracture. From Figures 2.22 (a) and 2.22 (c), Figures 2.22 (b) and 2.22 (d), we can observe that the width of the up-left fracture along lateral and vertical directions is the same with that of the up-right fracture. The shear displacement discontinuities of these two vertical fractures along lateral and vertical directions have the

same absolute value but opposite directions due to the fact that the direction of interface sliding is opposite. Figures 2.22 (e) and 2.22 (f) show the normalized displacement discontinuities of the upper horizontal fracture along the x and y directions at z = 50 ft, respectively. Results indicate that the shear displacement discontinuity in the y direction is larger than the opening of the horizontal fracture segment, which implies that more propagation energy is consumed for interfacial sliding, rather than opening of the horizontal fracture. The shear displacement discontinuities of the interfaces would influence the path of fluid flow and further hinder the fracture height growth. Additionally, proppant transportation within such fracture geometry is also affected due to the fact that the opening of the horizontal interface is extremely small, which is difficult for proppant passing through (Cohen et al. 2017).

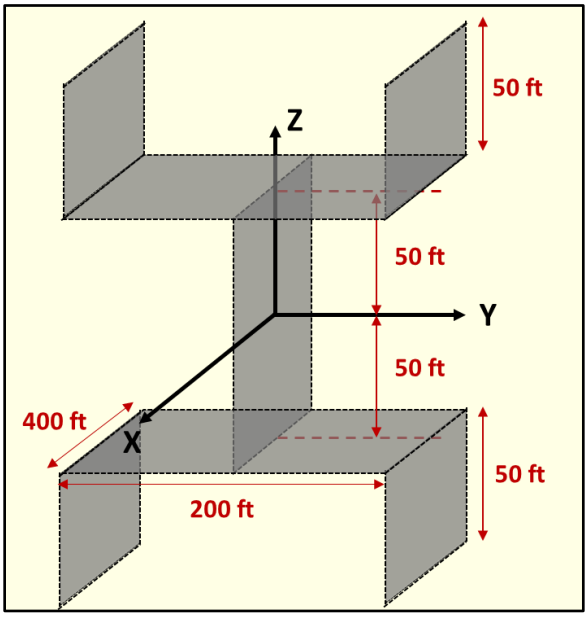

Figure 2.20: The dimension of a complex fracture geometry with offsets (Tang and Wu 2018).

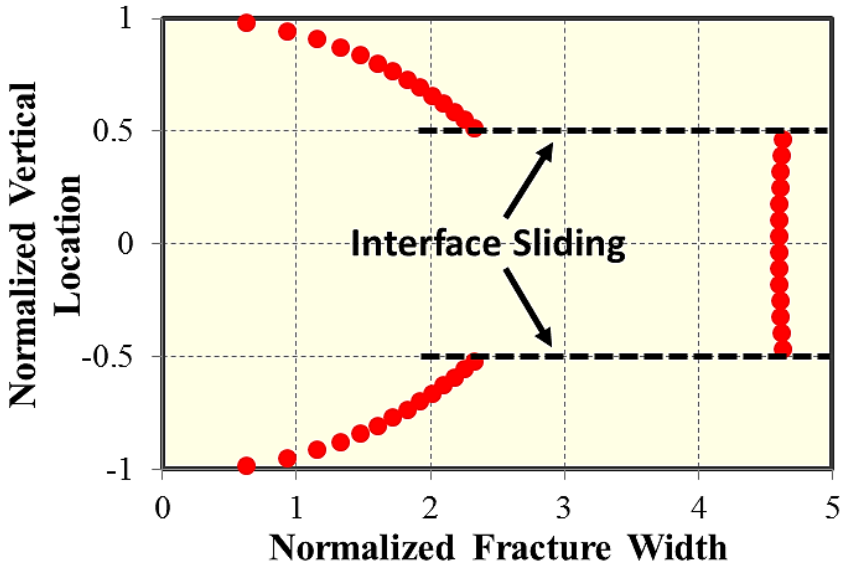

Figure 2.21: Normalized normal displacement discontinuity of down-right, central, and up-right vertical fractures along the z direction (Tang and Wu 2018).

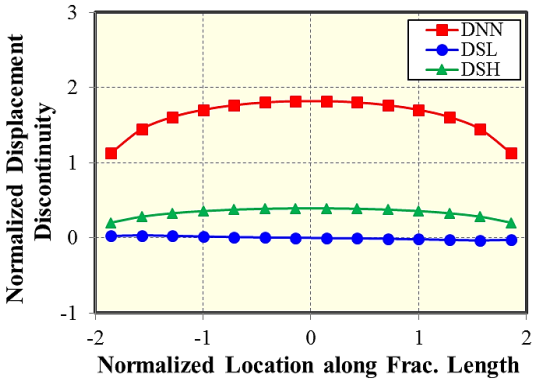

(a). Normalized displacement discontinuities of up-left vertical fracture along the x direction.

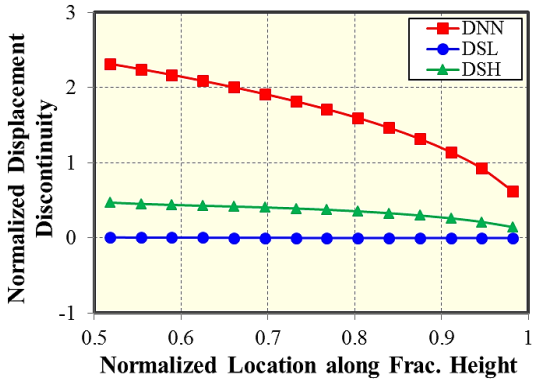

(b). Normalized displacement discontinuities of up-left vertical fracture along the z direction.

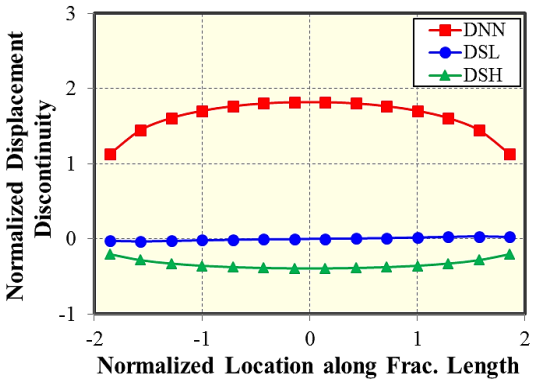

(c). Normalized displacement discontinuities of up-right vertical fracture along the x direction.

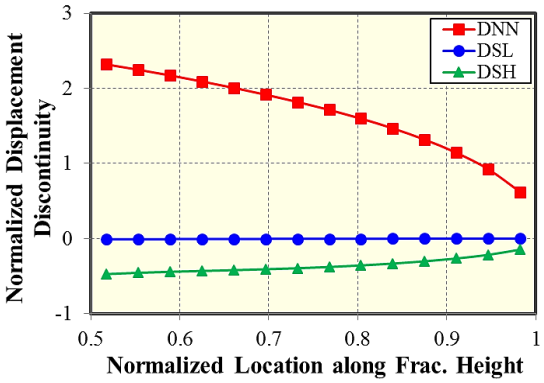

(d). Normalized displacement discontinuities of up-right vertical fracture along the z direction.

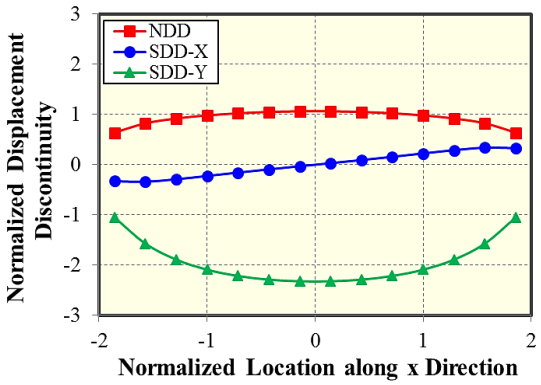

(e). Normalized displacement discontinuities of upper horizontal fracture along the x direction.

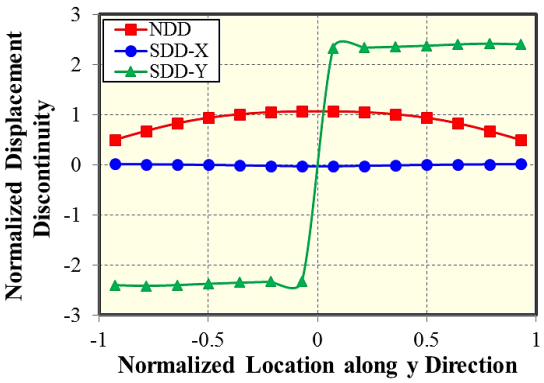

(f). Normalized displacement discontinuities of upper horizontal fracture along the y direction.

Figure 2.22: Normalized displacement discontinuities of fracture segments above the upper horizontal fracture (Tang and Wu 2018).

2.4 Conclusion

In this chapter, a fully 3D DDM was developed to investigate the interaction of a vertical fracture and interfaces with arbitrary angles in three dimensions, which is in

application of fracture height growth in laminated shale reservoirs. Five different prescribed fracture geometries with the combination of a vertical fracture and horizontal interfaces were investigated to study the effects of weak horizontal interfaces on distributions of displacement discontinuities. The following conclusions can be drawn from this study:

(1) A good match of fracture width and induced stresses between a 2D analytical solution and 3D DDM was obtained for a single fracture. The same results of displacement discontinuities were obtained for horizontal and vertical fractures with identical dimensions and net pressure.

(2) Fracture width profile of the vertical fracture along the height direction is changed by opening of a weak horizontal interface. A width jump is induced and width is greatly reduced across the interface. This width reduction hinders vertical fracture propagation in the height direction, which is regarded as another primary mechanism of fracture height containment.

(3) Shear displacement discontinuities induced on the horizontal interface is the root cause of width jump along the vertical fracture. With the increment of the distance between the wellbore location and the horizontal interface, shear displacement discontinuities become larger, resulting in greater width jump. This indicates that the vertical fracture is easier to be arrested as the wellbore location is far away from the interface. Selecting an optimal landing location of horizontal wellbore can minimize the fracture height containment.

(4) Compared to a single horizontal fracture case, the opening of a horizontal fracture crossed by a vertical fracture greatly decreases as a result of the opening of the vertical

fracture and shear displacement discontinuities along the horizontal fracture, which has an intensive effect on the proppant transport within the fracture.

(5) Although the fluid flow is not considered in this chapter, the analysis of different fracture geometries at the static condition provides a fundamental understanding of the effect of interface slippage on fracture height containment. Dynamic fracture growth as well as fluid flow diversion and proppant transport at fracture junction require further work of coupling this 3D model and fluid flow.

3. SENSITIVITY ANALYSIS

In this chapter, we would separately discuss the cases of the orthogonal approach angle with the bedding plane and the non-orthogonal cases. Approach angle, is defined as the intersection angle between the initial fracture direction and the bedding plane. In each case, sensitivity analysis of different parameters would be done to investigate its impact on the width profiles of the vertical fracture and the bedding plane and also the shear displacement discontinuities along the bedding plane.

3.1 Orthogonal Approach Angle with Bedding Plane

In this section, we investigated cases of orthogonal approach angle with bedding plane. In other words, the bedding plane (interface) is horizontally distributed. There are the case of one vertical fracture and one interface, the case of multiple vertical fractures and one interface and that of single vertical fracture and multiple interfaces. The fracture geometry in each case is pre-determined. The required parameters are given in Table 3.1. Generally, the overburden vertical stress is larger than the minimum horizontal stress in unconventional reservoirs. We assumed uniform fluid pressure within vertical and horizontal fractures, which implies that net pressure (fluid pressure minus the stress normal to the fracture) within vertical fractures is larger than that in horizontal fractures.

---

*Part of this section is reprinted with permission from "Investigate Effects of Weak Bedding Interfaces on Fracture Geometry in Unconventional Reservoirs" by J. Tang, K. Wu, B. Zeng, H. Huang, X. Hu, X. Guo, L. Zuo, 2017. Journal of Petroleum Science and Engineering, Copyright [2017] by Elsevier.

Parameter	Value	Unit
Vertical fracture length	400	ft
Vertical fracture height	100	ft
Net pressure for vertical fracture	1000	psi
Horizontal fracture length in x direction	400	ft
Horizontal fracture length in y direction	200	ft
Net pressure for horizontal fracture	500	psi
Distance between center of vertical fracture and horizontal interface	25	ft
Young's modulus	3.0E6	psi
Poisson's ratio	0.25	dimensionless

Table 3.1−Required parameters of an asymmetric crossing-shaped fracture case (Tang et al. 2017).

The fracture geometry is given in Figures 3.1 and 3.2, showing a 3D view and a front view of this asymmetric crossing-shaped fracture. The horizontal fracture segment is regarded as the opening of a bedding interface and vertical fracture would cross the interface. In the following sub-sections (except the section of fracture spacing), we did sensitivity analysis of parameters such as half-length of horizontal interface, fracture height, differential stresses (net pressure difference between the vertical fracture and horizontal interface), Young's modulus, Poisson's ratio, and also investigated their impacts on the displacement discontinuity profiles of the vertical fracture and the horizontal interface.

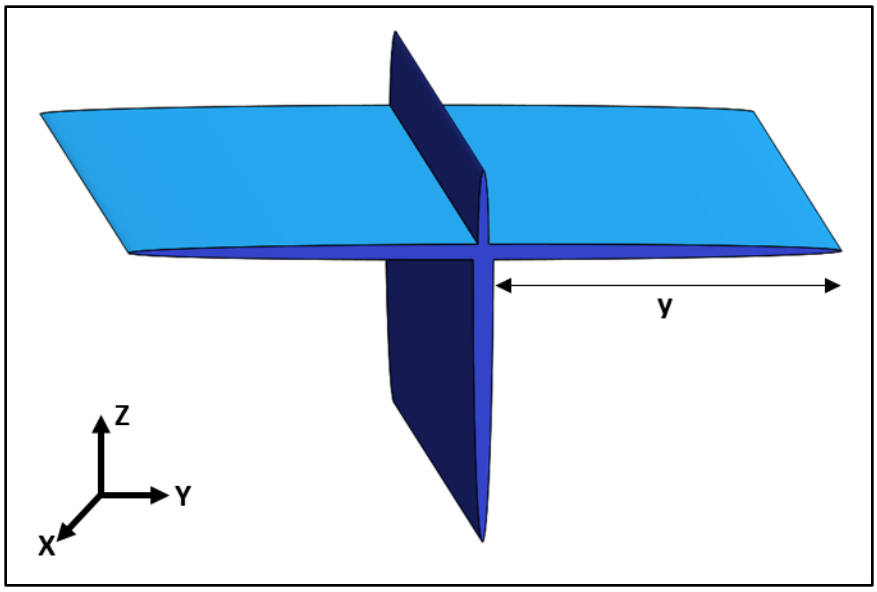

Figure 3.1: The geometry of an asymmetric crossing-shaped fracture (one vertical fracture and one horizontal interface) (Tang et al. 2017).

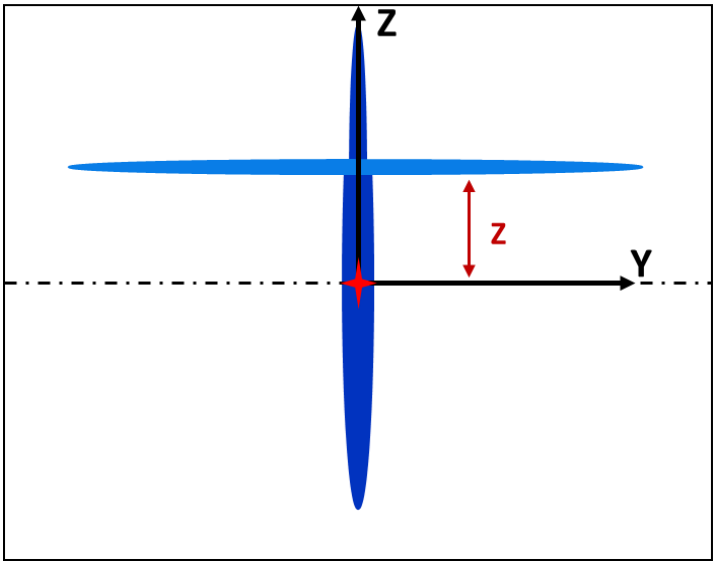

Figure 3.2: Front view of an asymmetric crossing-shaped fracture (varying distance between center of the vertical fracture and the horizontal fracture) (Tang et al. 2017).

3.1.1 Half-Length of Horizontal Interface

In this subsection, the effect of half-length of the horizontal fracture segment (y) was investigated. The distance between the center of the vertical fracture and the horizontal interface is prescribed as 25 ft (Z = 25ft). All required parameters for this case are listed in Table 3.1, except the horizontal fracture length in the y direction shown in Figure 3.1.

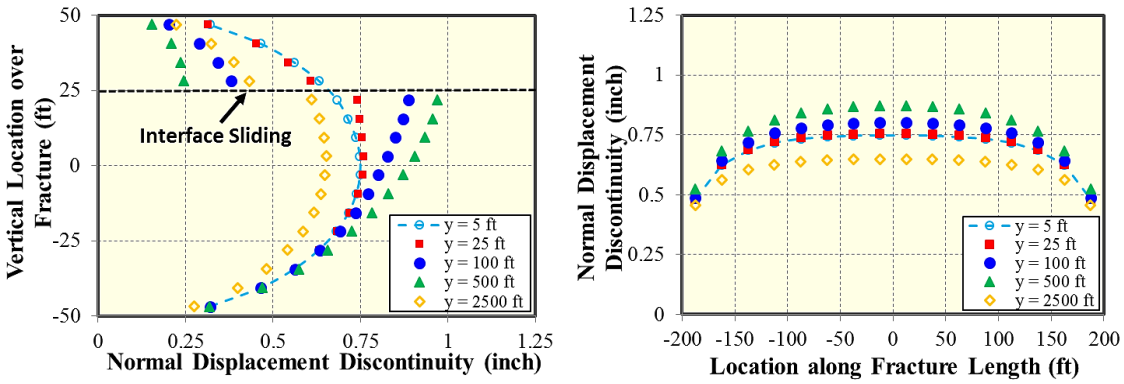

Figure 3.3: (a) Impact of half-length of the horizontal fracture segment on fracture width along the vertical direction; (b) Impact of half-length of the horizontal fracture segment on fracture width along the fracture length direction (Tang et al. 2017).

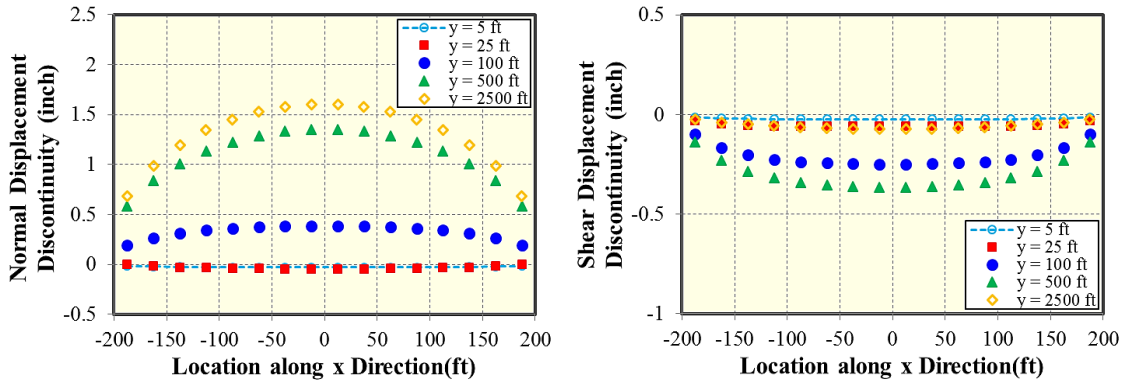

Figure 3.4: (a) Impact of half-length of the horizontal fracture segment on the opening of the horizontal interface along the x direction; (b) Impact of half-length of the horizontal

fracture segment on the shear displacement discontinuity of the horizontal interface along the x direction (Tang et al. 2017).

Figures 3.3 (a) and 3.3 (b) shows the width profile of the vertical fracture along the vertical and the length directions with five different half-lengths of the horizontal fracture, respectively. The fracture width is continuous at the crossing position when the half-length of the horizontal fracture segment is 5 ft (y = 5 ft). This is because the shear displacement along the horizontal interface approximates zero, as depicted in Figure 3.4 (b). The significant dimensional difference between the vertical fracture and the horizontal interface indicates that the effect of the horizontal interface can be neglected. As the half-length increases, the shear displacement becomes larger and a jump of fracture width on the vertical fracture increases (Figure 3.3 (a)). This result indicates that the fracture height containment is more likely as half-length of the horizontal fracture segment (such as natural fracture, fault or other discontinuity) becomes larger. However, vertical fracture width starts to decrease when half-length of the horizontal fracture segment reaches a large value (i.e. y = 2500 ft). From y = 500 ft to y = 2500 ft, the value of shear displacement along horizontal interface falls sharply and thus the interfacial sliding distance is also reduced. This is because the asymmetric crossing-shaped fracture is dominated by the horizontal fracture when the dimension of the vertical fracture is much smaller than that of the horizontal fracture. Figure 3.4 (a) illustrates opening of the horizontal fracture segment (along with the x direction). Because the compressive stress induced by the vertical fracture is large, the horizontal interface is closed when half-length of horizontal fracture segment is small (i.e. y = 5 ft and y = 25 ft). When the size of horizontal fracture

segment becomes larger, the horizontal interface can be opened as a result of decrement of the compressive stress induced by the vertical fracture.

3.1.2 Fracture Height

In this subsection, we first studied the effect of distance between the center of the vertical fracture and the horizontal interface, which is equivalent to the distance between the injection point and the interface during hydraulic fracture treatments. The normal displacement discontinuity (i.e. fracture width) of the vertical fracture with different Z/H, named as the ratio of the distance between the center of the vertical fracture and the horizontal interface to the fracture height, is shown in Figure 3.5. In Figure 3.5 (a), there is a jump of fracture width on the vertical fracture at the crossing position of the interface due to the shear displacements along the horizontal interface. This width jump is defined as an interfacial sliding distance which can be quantified by 3D DDM. We could calculate the approximate value of interfacial sliding distance as 0.235 inches, 0.507 inches and 0.826 inches when Z/H is 0.1, 0.25 and 0.4, respectively, which indicates that interfacial sliding distance has a positive correlation with the Z/H ratio. Moreover, Figures 3.6 (a) and 3.6 (b) elaborates the shear displacement discontinuities in the y direction (along with the horizontal interface), which also demonstrates that shear sliding increases with the increment of the distance. Therefore, we could infer that the interfacial sliding distance is greatest when the fracture tip contacts with the horizontal interface (Z/H = 0.5). Figure 3.5 (b) illustrates the width profile of the vertical fracture along the length direction, which does not show obvious width alteration with the increment of the Z/H ratio. Figure 3.7

describes the normal displacement discontinuity of the horizontal interface along the x and the y directions, respectively. In Figure 3.7 (a), the opening of the horizontal interface along the x direction increases with the distance. However, a "trough" of fracture width can be observed in the range of y = -50 ft to y = 50 ft (Figure 3.7 (b)), as a result of positive normal stress induced by the vertical fracture behaving as a compressive stress which acting on the middle section of horizontal interface. With the increment of the distance, the normal stress induced by the vertical fracture decreases.

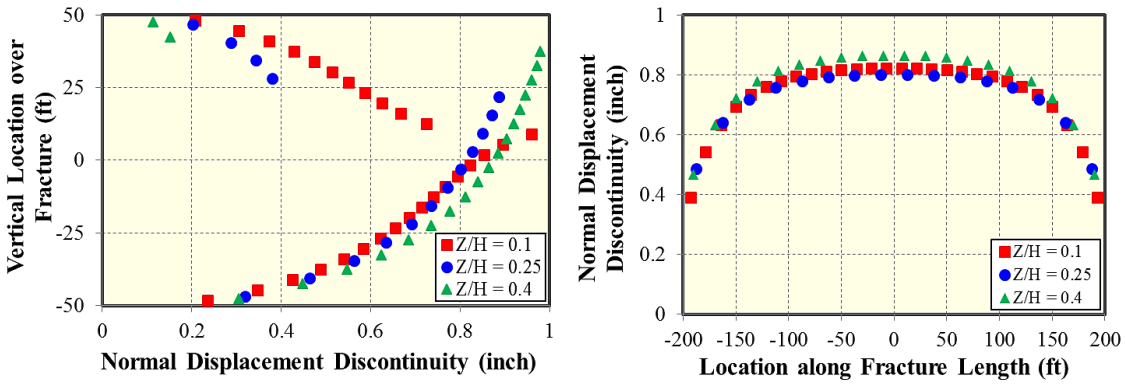

Figure 3.5: (a) Impact of Z/H on fracture width along the vertical direction; (b) Impact of Z/H on fracture width along the fracture length direction (Tang et al. 2017).

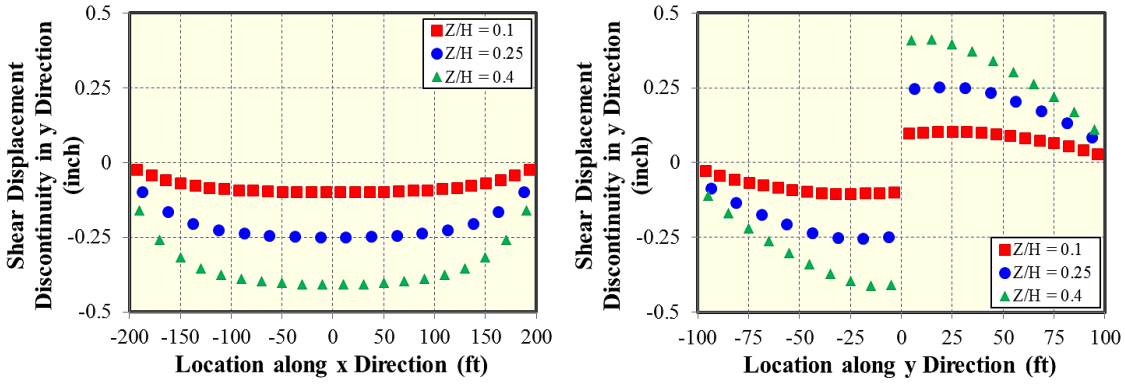

Figure 3.6: (a) Impact of Z/H on shear displacement discontinuity of the horizontal interface along the x direction; (b) Impact of Z/H on shear displacement discontinuity of the horizontal interface along the y direction (Tang et al. 2017).

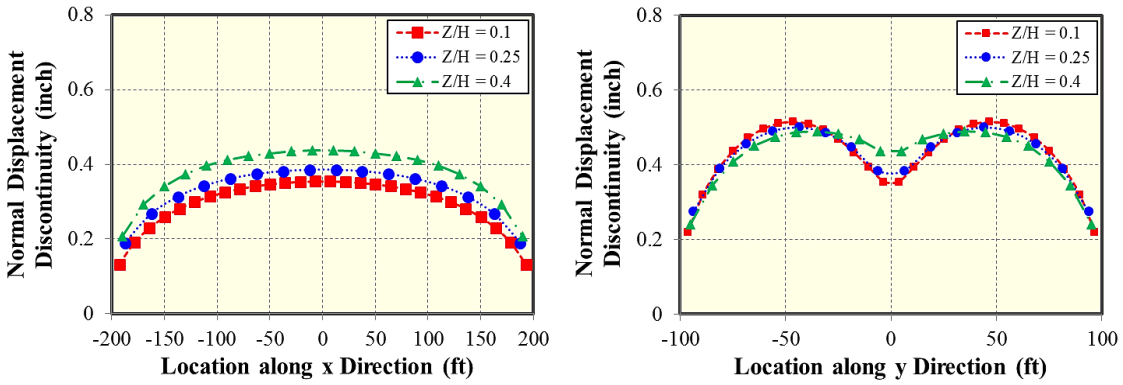

Figure 3.7: (a) Impact of Z/H on the opening of the horizontal interface along the x direction; (b) Impact of Z/H on the opening of the horizontal interface along the y direction (Tang et al. 2017).

If we consider a fracture propagating from the injection point, the Z/H ratio would always equal 0.5. When the fracture tip contacts with the horizontal interface, and the interfacial sliding distance would reach its maximum value. In order to test whether the distance between the injection point and the horizontal interface would affect the likelihood of fracture arrest, cases with different fracture height (50 ft, 100 ft, 200ft) are investigated and the horizontal interface is always placed at the upper tip of the fracture (Z/H = 0.5). Figure 3.8 (a) illustrates the impact of fracture height on the width profile of the vertical fracture along the vertical direction, which indicates that the fracture width grows monotonically from lower tip to upper tip and the maximum value of the interfacial sliding distance is obtained at the location of the interface. Additionally, it reveals that the interfacial sliding distance along the interface is positively correlated with the pre-determined fracture height. The larger the interfacial sliding distance, the easier the

vertical fracture tends to be arrested by the interface when the injection point is far away from the interface. Impact of fracture height (H) on the opening of the horizontal interface (along with the y direction) is shown in Figure 3.8 (b). Along the interface, minimum normal displacement discontinuity is obtained at two tips and the maximum value is between the tip and the center point. A "trough" of opening is observed in the range of y = -25 ft to y = 25 ft, as a result a compressive stress acting in the middle section of the horizontal interface. With the increment of pre-determined fracture height, the opening of the horizontal interface decreases. Figures 3.9 (a) and 3.9 (b) illustrate the shear displacement discontinuities of the horizontal interface in the x and y directions, respectively, which is under the impact of different fracture heights. We could observe a positive relationship between the shear displacement discontinuity of the interface and the pre-determined fracture height, which proves that the fracture is more easily to be arrested by the interface when the injection point is far away from the horizontal interface.

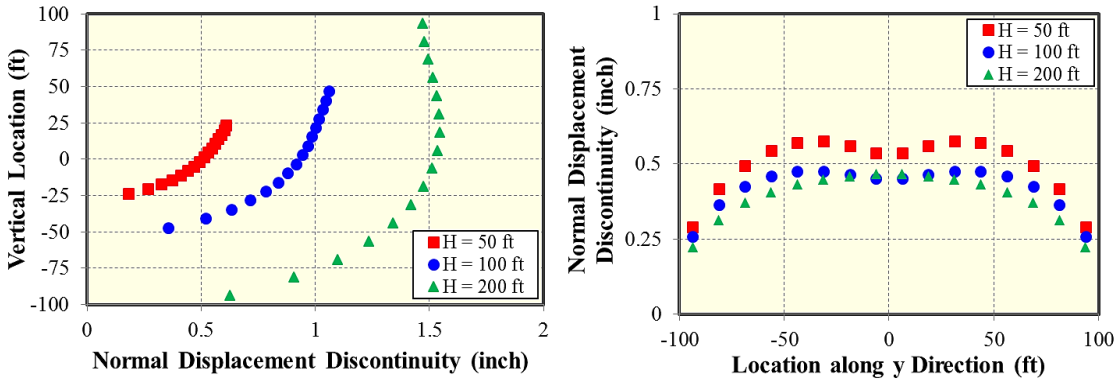

Figure 3.8: (a) Impact of fracture height on fracture width along the vertical direction; (b) Impact of fracture height on the opening of the horizontal interface along the y direction (Tang et al. 2017).

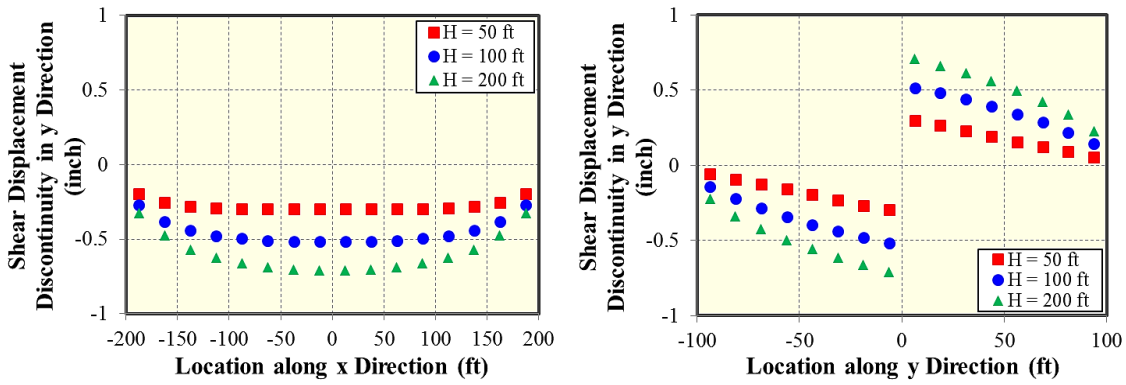

Figure 3.9: (a) Impact of fracture height on shear displacement discontinuity of the horizontal interface along the x direction; (b) Impact of fracture height on shear displacement discontinuity of the horizontal interface along the y direction (Tang et al. 2017).

3.1.3 Differential Stress

The net pressure within fracture segments also plays an important role in determining the fracture width distribution. The distance between the center of the vertical fracture and the horizontal interface is 25 ft. Other required parameters are shown in Table 3.1. Figures 3.10 (a) and 3.10 (b) elaborate the normal displacement discontinuity of the vertical fracture along the vertical and the length directions, respectively. In this study, we kept the fluid pressure as a constant and only adjust the value of the overburden stress (S_v) and the horizontal minimum stress (S_{hmin}). P_{nh} represents the net pressure within the horizontal fracture segment and P_{nv} is the net pressure within the vertical fracture. Additionally, the net pressure difference between the vertical fracture and the horizontal interface is kept as 500 psi, which means that the stress difference between Sv and Shmin is kept as 500 psi ($S_v > S_{hmin}$).

From the figure, we can find that both fracture width and interfacial sliding distance along the horizontal interface increase with the increment of net pressure. The opening of the horizontal fracture segment along the large dimension (400 ft) and the small dimension (200 ft) are shown in Figures 3.11 (a) and 3.11 (b). When the net pressure within the horizontal fracture segment equals to zero, the opening of the horizontal interface is negative, which means the two surfaces of the horizontal interface compress each other and the interface is kept as closed status (Shen et al. 2015). This is due to that no fluid infiltration occurs in the horizontal fracture segment and this segment is also under the influence of compressive stress induced by the vertical fracture. As the net pressure within the vertical fracture and horizontal fracture segment simultaneously increase, the horizontal interface can be opened gradually. Moreover, the augment of net pressure within the fracture segment also explains why the opening of the horizontal interface increases. Figure 3.12 depicts the distribution of shear displacement discontinuities along the x and the y directions, respectively. We can observe that shear displacements along the horizontal interface are positively correlated with the net pressure within fracture segments. According to the result, it implies that the vertical fracture is much easier to be arrested by the horizontal interface with the increment of pumping pressure, although it makes the width of fracture segments much larger.

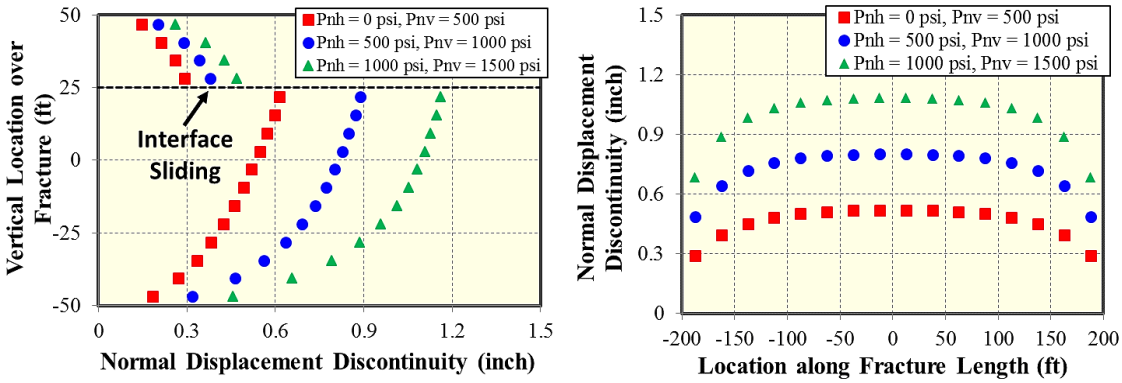

Figure 3.10: (a) Impact of net pressure on fracture width along the vertical direction; (b) Impact of net pressure on fracture width along the fracture length direction (Tang et al. 2017).

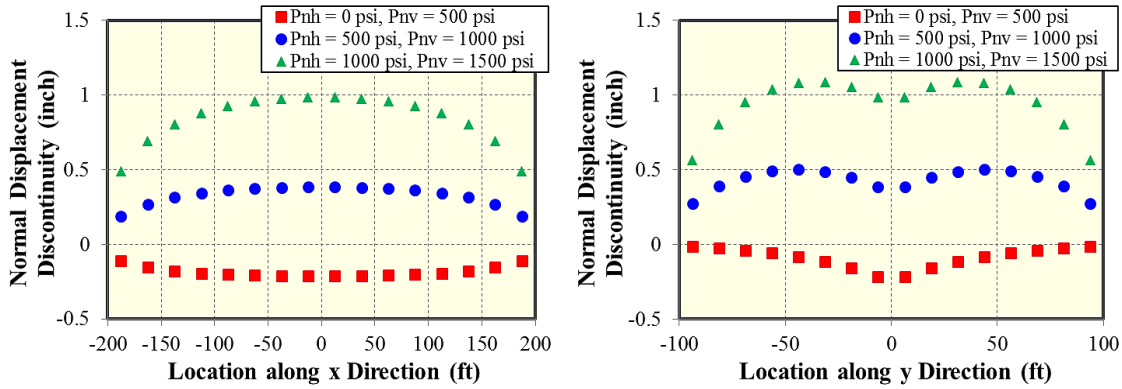

Figure 3.11: (a) Impact of net pressure on the opening of the horizontal interface along the x direction; (b) Impact of net pressure on the opening of the horizontal interface along the y direction (Tang et al. 2017).

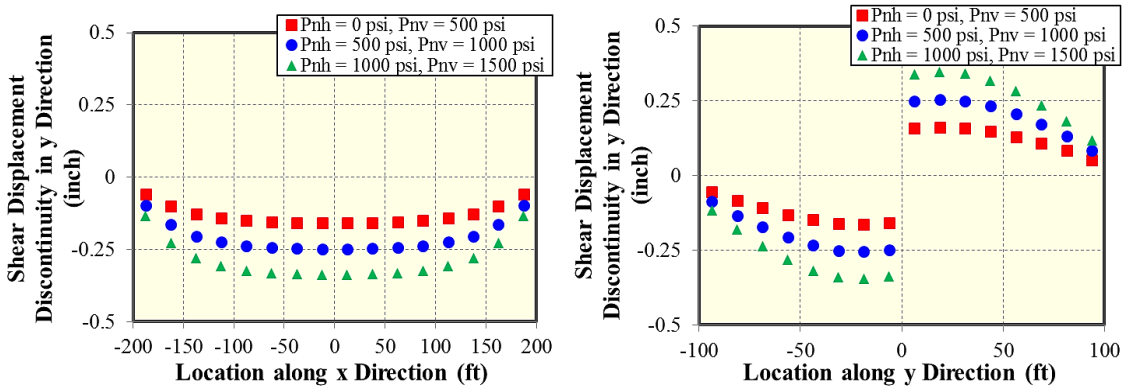

Figure 3.12: (a) Impact of net pressure on shear displacement discontinuity of the horizontal interface along the x direction; (b) Impact of net pressure on shear displacement discontinuity of the horizontal interface along the y direction (Tang et al. 2017).

3.1.4 Young's Modulus

Different Young's modulus' (YM) result in different net pressures within the fracture if the coupled rock deformation and fluid flow model is used. In this paper, the net pressure within the fracture is kept as a constant value and we mainly focus on the effect of Young's modulus on fracture width and shear displacements along the horizontal interface. In this case, we used the Young's Modulus as 1.0E6 psi, 3.0E6 psi and 6.0E6 psi and kept other parameters the same with that in Table 3.1. The distance between vertical fracture center and the horizontal interface is 25 ft. From Figure 3.13, we observe that the vertical fracture width decreases as Young's Modulus becomes larger. Additionally, we find a negative correlation between interfacial sliding distance and Young's modulus, as a result of decrement of shear displacements (y direction) along the horizontal interface when Young's Modulus increases, which depicted in Figure 3.15. With the augment of Young's Modulus, its effect on fracture width distribution becomes very obvious. Figures 3.14 (a) and 3.14 (b) illustrate the fracture width profile of horizontal

interface along the x and the y directions, respectively. The opening of the horizontal interface would increase as the decreasing of Young's Modulus. At the same time, the width "trough" becomes more evident due to the fact that the compressive stress induced by the vertical fracture which acting on the middle section of horizontal fracture segment, becomes larger. The observation reveals that formation properties such as Young's Modulus play an important role in determining the width of the vertical fracture and also the fracture height growth. During hydraulic fracturing treatment, shale formation with large Young's Modulus should be utilized to decrease the fracture height containment induced by the horizontal interface.

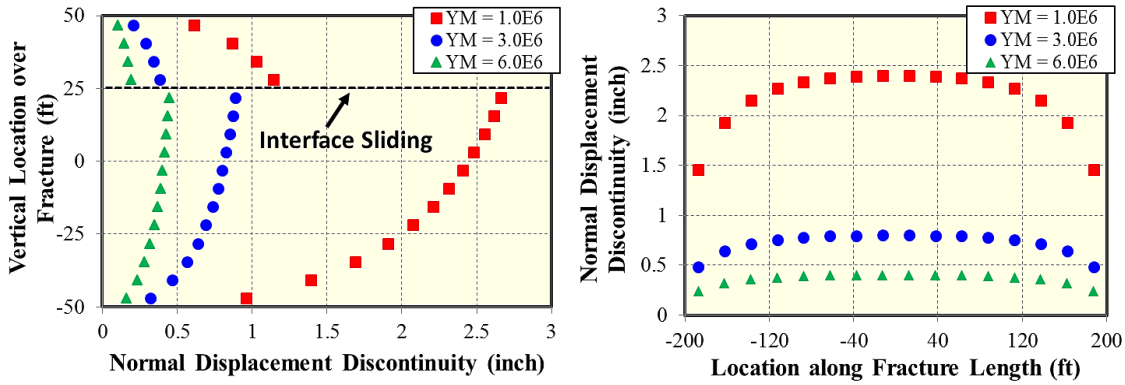

Figure 3.13: (a) Impact of Young's modulus on fracture width along the vertical direction; (b) Impact of Young's modulus on fracture width along the fracture length direction (Tang et al. 2017).

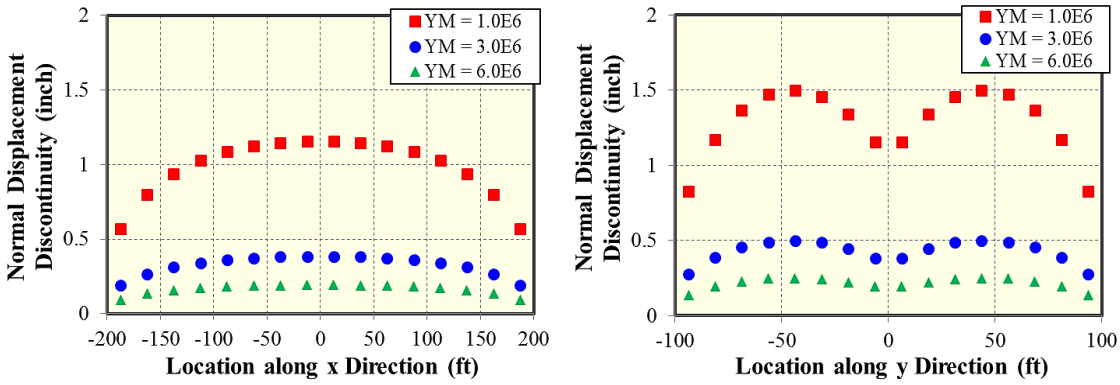

Figure 3.14: (a) Impact of Young's modulus on the opening of the horizontal interface along the x direction; (b) Impact of Young's modulus on the opening of the horizontal interface along the y direction (Tang et al. 2017).

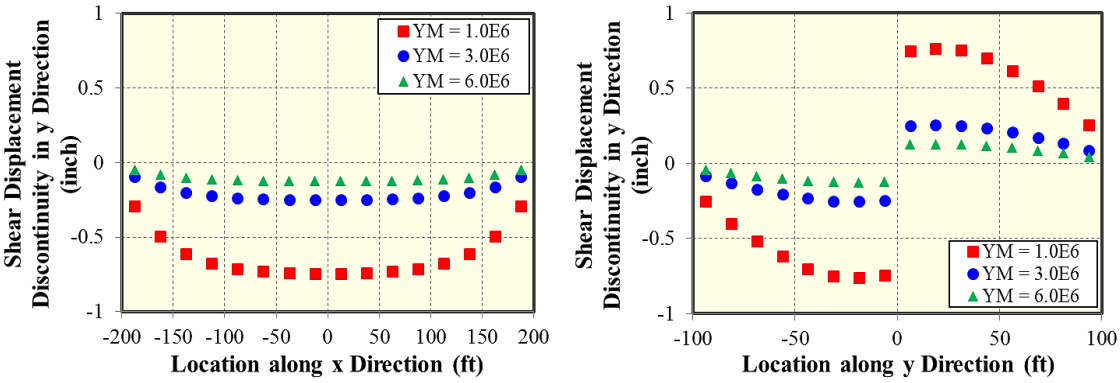

Figure 3.15: (a) Impact of Young's modulus on shear displacement discontinuity of the horizontal interface along the x direction; (b) Impact of Young's modulus on shear displacement discontinuity of the horizontal interface along the y direction (Tang et al. 2017).

3.1.5 Poisson's Ratio

Poisson's ratio (PR) also plays an important role in the fracture propagation with bedding interfaces. Figures 3.16 (a) and 3.16 (b) illustrate the impact of varying Poisson's ratio on the normal displacement discontinuity of the vertical fracture along the vertical and length directions, respectively. A result is observed that the interfacial sliding distance

is negatively correlated with Poisson's ratio. Hence, a smaller Poisson's ratio, which leading to less magnitude of the compressive horizontal stress induced by the opening of the horizontal interface, then determine much larger width of the vertical fracture at the intersection between the fracture and the interface. Figure 3.17 shows the opening of the horizontal interface would increase as Poisson's ratio decreases. Figures 3.18 (a) and 3.18 (b) indicate the impact of Poisson's ratio on the profile of the shear displacement discontinuity along the x and y directions, respectively. The maximum value is obtained at the interface center and the minimum value is achieved at two tips. Along the y direction, the sign of the shear displacement discontinuity is suddenly changed from negative to positive at the location y = 0. Additionally, Figure 18 also shows that Poisson's ratio slightly affects the shear displacement discontinuity of the horizontal interface.

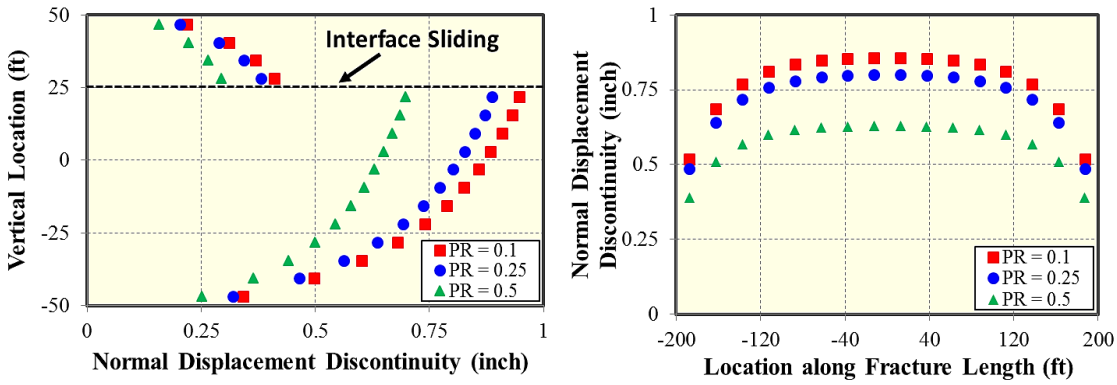

Figure 3.16: (a) Impact of Poisson's ratio on fracture width along the vertical direction; (b) Impact of Poisson's ratio on fracture width along the fracture length direction (Tang et al. 2017).

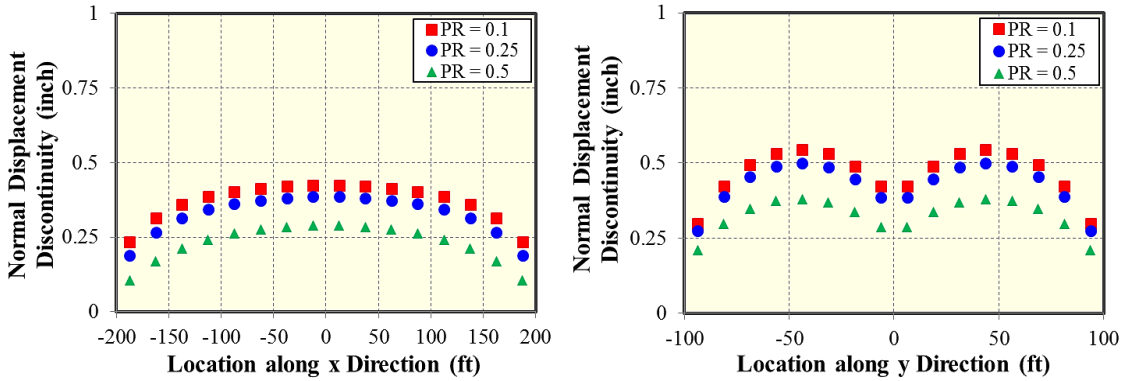

Figure 3.17: (a) Impact of Poisson's ratio on the opening of the horizontal interface along the x direction; (b) Impact of Poisson's ratio on the opening of the horizontal interface along the y direction (Tang et al. 2017).

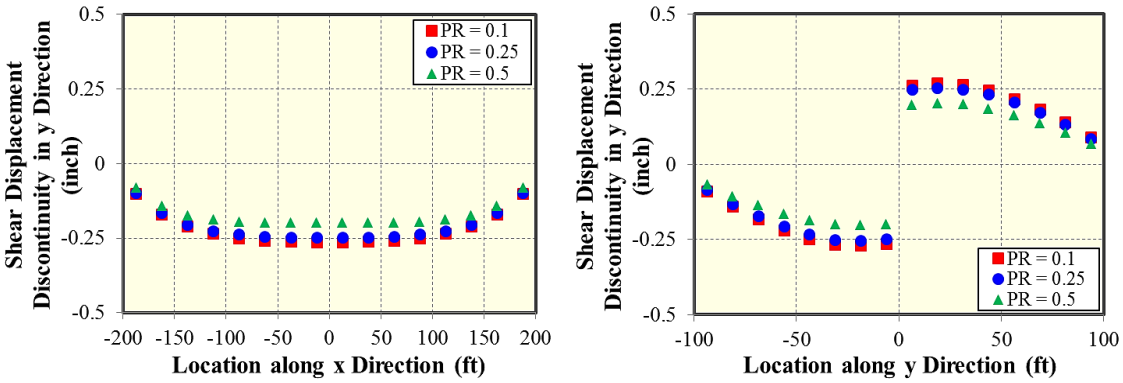

Figure 3.18: (a) Impact of Poisson's ratio on shear displacement discontinuity of the horizontal interface along the x direction; (b) Impact of Poisson's ratio on shear displacement discontinuity of the horizontal interface along the y direction (Tang et al. 2017).

3.1.6 Fracture Spacing

In this subsection, two fracture geometries with two vertical fractures and one horizontal interface were investigated. The only difference of the two fracture geometries is the distance between the center of each vertical fracture and the horizontal interface. We analyzed effects of the opening interface on width profiles of multiple fractures. Figure

3.19 shows an asymmetric crossing-shaped fracture geometry with two vertical fractures and one horizontal interface. Other parameters are shown in Table 3.1. The front view of this fracture geometry is depicted in Figure 3.20. The varying parameter in this case is the distance between two adjoining vertical fracture (fracture spacing), which is defined as d_s.

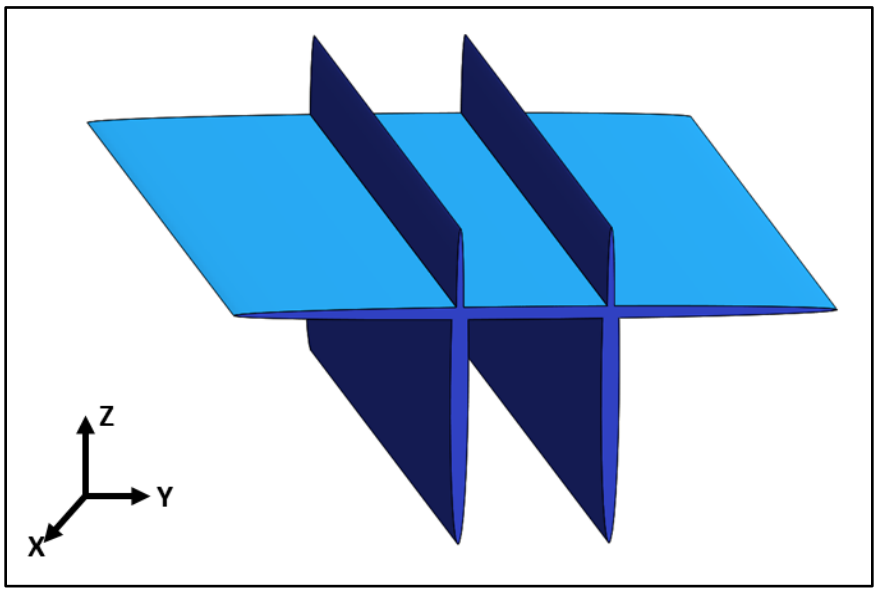

Figure 3.19: The geometry of an asymmetric crossing-shaped fracture with two vertical fractures and one horizontal interface (Tang et al. 2017).

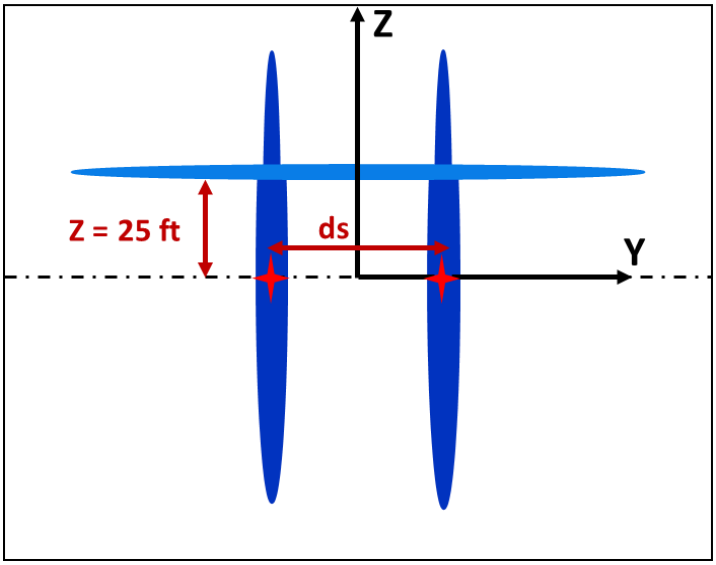

Figure 3.20: Front view of the asymmetric crossing-shaped fracture in Fig. 21 (Tang et al. 2017).

Figure 3.21 indicates the width profiles of vertical fracture (left) with three different fracture spacing, 50 ft, 100 ft and 150 ft. A geometry of two vertical fractures (100 ft fracture spacing) without a horizontal interface is regarded as a referential geometry, labeled as a black color. Compared with referential geometry, the geometry of two vertical fractures with 100 ft fracture spacing has smaller fracture width under the interaction with the horizontal interface. From the Figure 3.21 (a), we observed that vertical fracture width increases when the fracture spacing increases. However, the interfacial sliding distance along the interface decreases at the same time. In this case, the length of the interface is pre-determined and a larger fracture spacing means that the two vertical fractures intersect closer to the interface tips. The lateral distance between one interface tip and the neighboring vertical fracture can be regarded as the half effective length of the horizontal interface. Thus, the shorter effective length of the horizontal

interface creates a lower shear displacement. Figure 3.21 (b) also shows a positive correlation between vertical fracture width along fracture length direction and fracture spacing due to attenuation of stress shadow effects with the increasing of fracture spacing. Due to symmetry, two vertical fractures have the same width profile. Figure 3.22 only delineates the shear displacement discontinuities of the left vertical fracture along the fracture height and the fracture length directions, respectively. When fracture spacing d_s is 100 ft, the fracture geometry with an interface has larger shear displacements along both directions, compared with the geometry without an interface, which demonstrates that the horizontal interface has a significant impact on the shear displacement discontinuity of the vertical fracture. We also investigated that shear displacement discontinuities of the vertical fracture have a positive relation with fracture spacing according to Figure 3.22. Additionally, the sign of shear displacement discontinuity along the vertical direction is negative below the horizontal interface and turns to be positive above the interface, which indicates that the horizontal interface alters the direction of shear sliding along the vertical fracture.

The width profiles of the horizontal interface along the x and the y directions are shown in Figure 3.23. With the attenuation of stress shadow effect caused by the increment of fracture spacing, the width of vertical fractures increases and opening of the horizontal interface is amplified at the same time. In Figure 3.23 (b), a width "trough" is generated at the intersection point of the vertical fracture and horizontal interface, as a result of large compressive stress induced by the vertical fracture. Figure 3.24 (a) illustrates that shear displacement discontinuity along the x direction of the horizontal interface approximates

zero for different fracture spacing. Figure 3.24 (b) shows shear displacement discontinuity along the y direction of the horizontal interface varying with the fracture spacing. The shear sliding direction along the horizontal interface is changed twice at the intersection points of vertical fractures and horizontal interface.

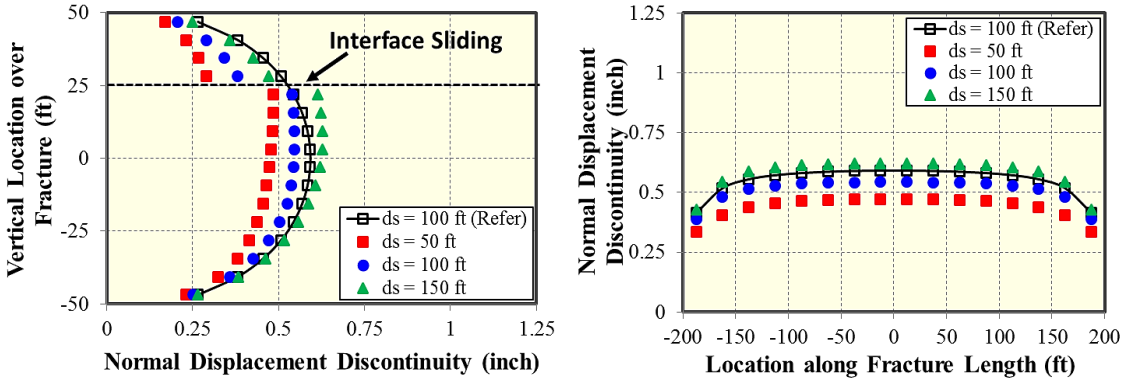

Figure 3.21: (a) Impact of fracture spacing on fracture width along the vertical direction; (b) Impact of fracture spacing on fracture width along the fracture length direction (Tang et al. 2017).

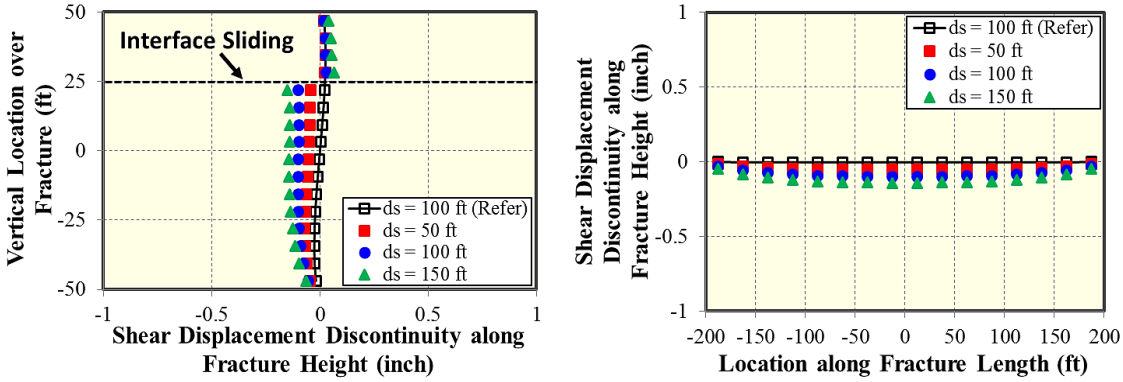

Figure 3.22: (a) Impact of fracture spacing on shear displacement discontinuity of the vertical fracture along the fracture height direction; (b) Impact of fracture spacing on shear displacement discontinuity of the vertical fracture along the fracture length direction (Tang et al. 2017).

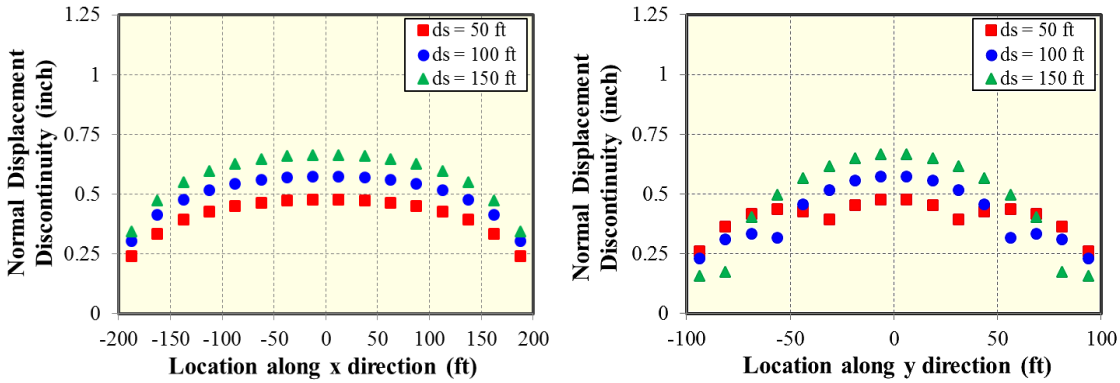

Figure 3.23: (a) Impact of fracture spacing on the opening of the horizontal interface along the x direction; (b) Impact of fracture spacing on the opening of the horizontal interface along the y direction (Tang et al. 2017).

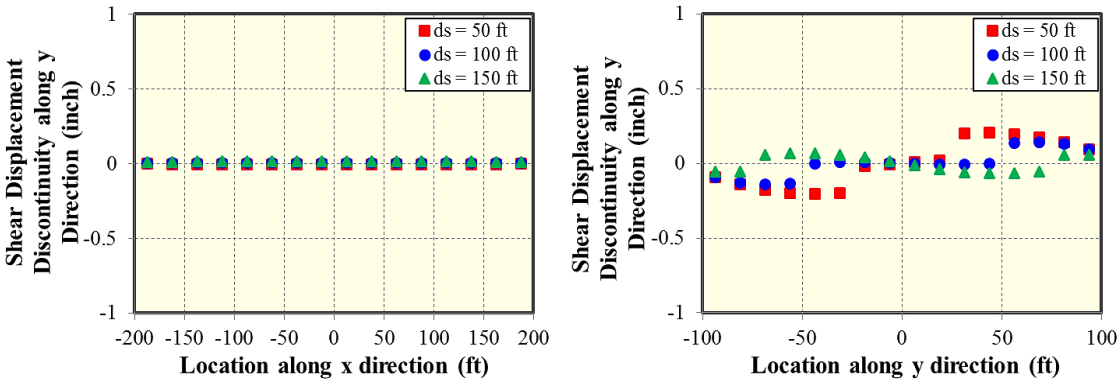

Figure 3.24: (a) Impact of fracture spacing on shear displacement discontinuity of the horizontal interface along the x direction; (b) Impact of fracture spacing on shear displacement discontinuity of the horizontal interface along the y direction (Tang et al. 2017).

The only difference between Figure 3.19 and Figure 3.25 is the distance between the center of vertical fractures and position of the horizontal interface. Other required parameters are the same as the previous case. In this case, we moved up the horizontal interface (Z = 50 ft) to make the vertical fracture arrested by the interface. Figure 3.26 reveals a front view of a Π-shaped fracture. We studied its effect of fracture spacing on

displacement discontinuities for vertical fractures and the horizontal interface. In Figure 3.27, it shows width distribution of left vertical fracture along the longer dimension (400 ft) and the shorter dimension (100 ft), respectively. Three different fracture spacings are given in each subplot. From Figure 3.27 (a), the vertical fracture width increases from the lower tip to the center of fracture, and then gradually decreases from the center to the upper tip. When fracture width reaches its maximum at a certain position, it is then restricted and starts to decrease until vertical fractures are arrested by the horizontal interface. Additionally, Figures 3.27 (a) and 3.27 (b) both indicate a positive correlation between vertical fracture width and fracture spacing. This is due to the decay of stress shadow effects with enhancement of fracture spacing. The direction of shear sliding along the vertical fracture is determined by the sign of shear displacement discontinuities of the vertical fracture. From Figure 3.28 (a), the vertical fracture slips in one direction and reaches its maximum sliding at the crossing position with the horizontal interface (Z = 50 ft). Compared with the slip along the fracture height direction, the sliding along the fracture length direction has a maximum value at the center of vertical fracture as depicted in Figure 3.28 (b). Moreover, Figure 3.28 elaborates a positive relation between shear displacement discontinuities of vertical fractures and fracture spacing.

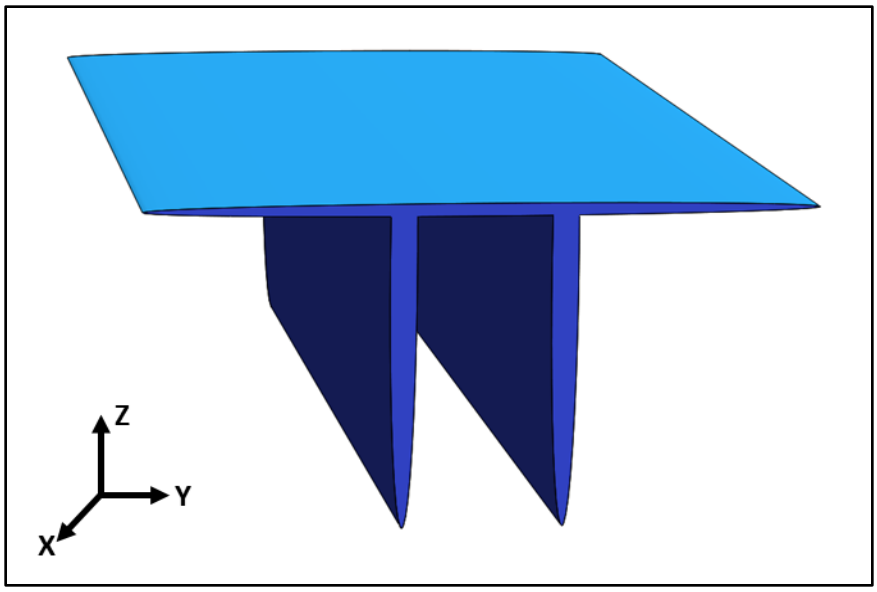

Figure 3.25: The geometry of a Π-shaped fracture (two vertical fractures and one horizontal interface) (Tang et al. 2017).

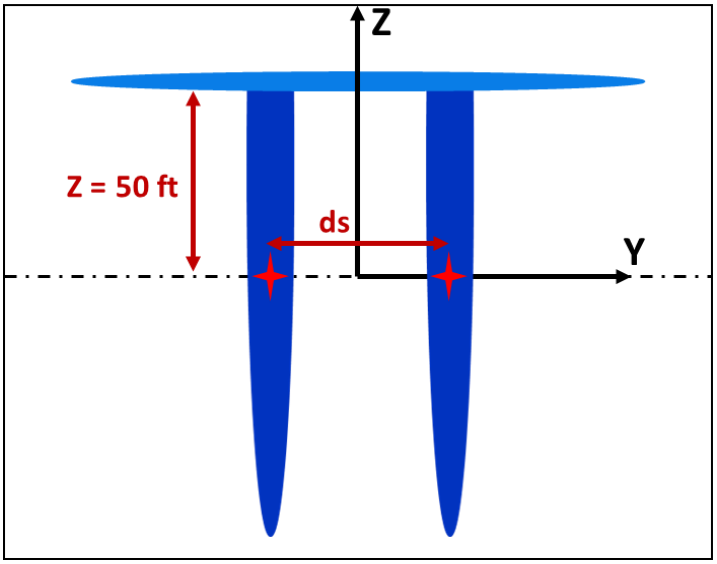

Figure 3.26: Front view of a Π-shaped fracture (The distance between two adjacent vertical fractures is variable) (Tang et al. 2017).

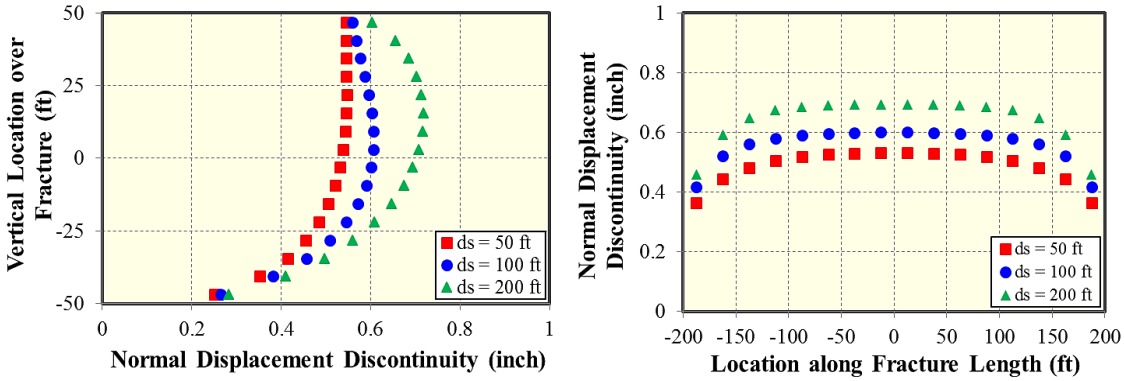

Figure 3.27: (a) Impact of fracture spacing on fracture width along the vertical direction; (b) Impact of fracture spacing on fracture width along the fracture length direction (Tang et al. 2017).

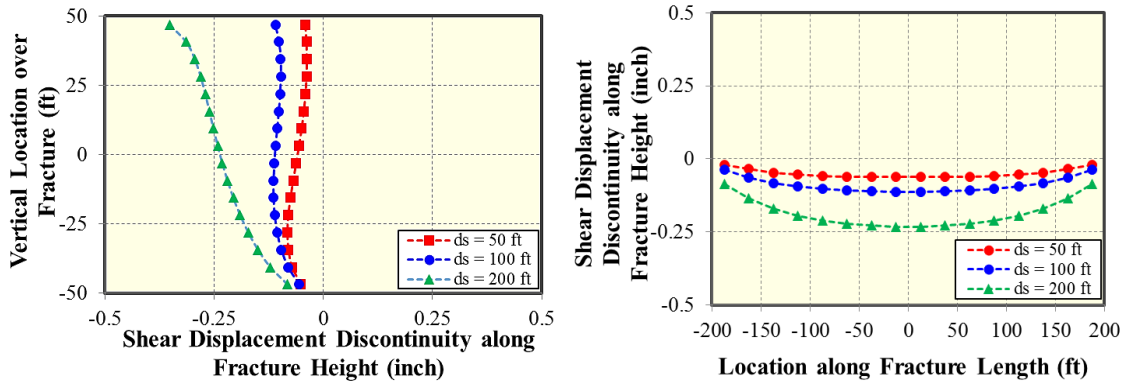

Figure 3.28: (a) Impact of fracture spacing on shear displacement discontinuity of the vertical fracture along the fracture height direction; (b) Impact of fracture spacing on shear displacement discontinuity of the vertical fracture along the fracture length direction (Tang et al. 2017).

Normal displacement discontinuity and shear displacement discontinuities of the horizontal interface are shown in Figures 3.29 and 3.30, respectively. Figure 3.29 illustrates opening of the horizontal interface increases as fracture spacing increases. In Figure 3.29 (b), a sudden jump of the interface opening appears at each intersection point,

probably due to an intensive decrement of compressive stress induced by vertical fracture. When fracture spacing increases as 200 ft, the two upper tips of vertical fractures coincide with endpoints of the horizontal interface and no width jump occurs along the interface, which makes opening distribution of the horizontal interface is continuous. Along the x direction, the shear displacement discontinuity approximates zero and varies slightly as the alteration of fracture spacing, which is depicted in Figure 3.30 (a). Figure 3.30 (b) shows the shear displacement discontinuity along the y direction. The direction of shear sliding along the interface changes at each intersection point. The maximum shear displacement discontinuity is obtained at the two intersection points, which has equivalent magnitude but opposite direction. The minimum value stays in the middle of the horizontal interface.

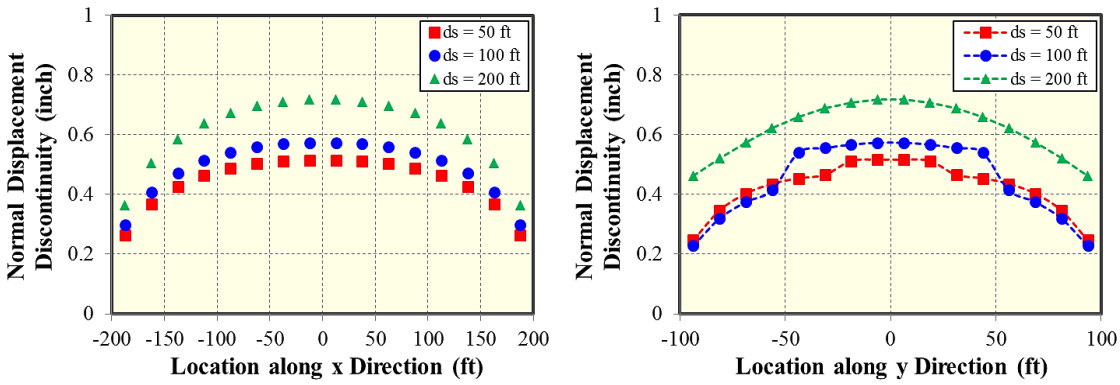

Figure 3.29: (a) Impact of fracture spacing on the opening of the horizontal interface along the x direction; (b) Impact of fracture spacing on the opening of the horizontal interface along the y direction (Tang et al. 2017).

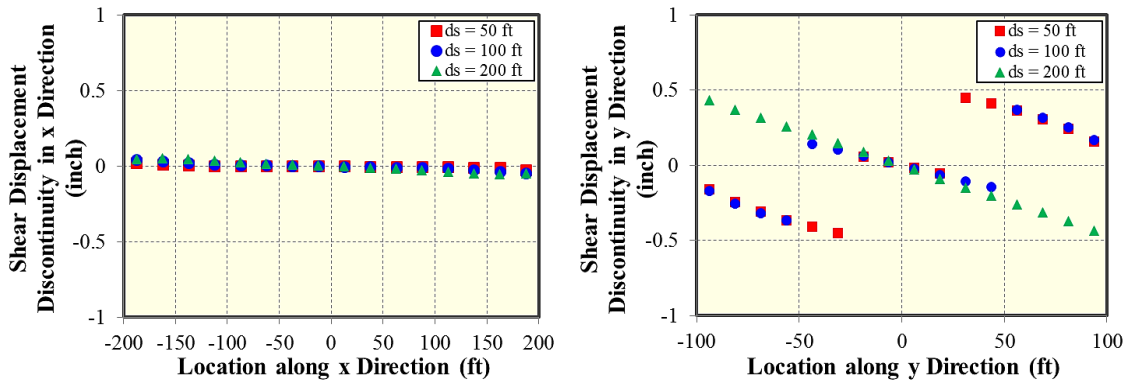

Figure 3.30: (a) Impact of fracture spacing on shear displacement discontinuity of the horizontal interface along the x direction; (b) Impact of fracture spacing on shear displacement discontinuity of the horizontal interface along the y direction (Tang et al. 2017).

3.2 Non-orthogonal Approach Angle with the Bedding Plane

In the real world, some multi-layered bedding planes, regarded as frictional discontinuities, are not horizontally distributed in the formation. In this subsection, we did sensitivity analysis of approach angle, Z/H ratio (the ratio of the distance between the center of the vertical fracture and the horizontal interface to the pre-determined fracture height), fluid pressure, Young's modulus and Poisson's ratio, and investigated their impacts on the normalized width profiles of the vertical fracture along the z direction and the x direction, normalized opening of the inclined interface along the interface and normalized shear displacement discontinuity along the interface. The selected pre-determined fracture geometries for each case are illustrated in Figure 3.31. These two crossing-shaped fracture geometries in Figure 3.31 both consist of a vertical fracture and an inclined bedding plane with approach angle α. Figure 3.31 (a) reveals that the injection source locates at the bedding plane. There has a distance z between the injection point and

the center of the bedding plane in Figure 3.31 (b). All required parameters are given in Table 3.1.

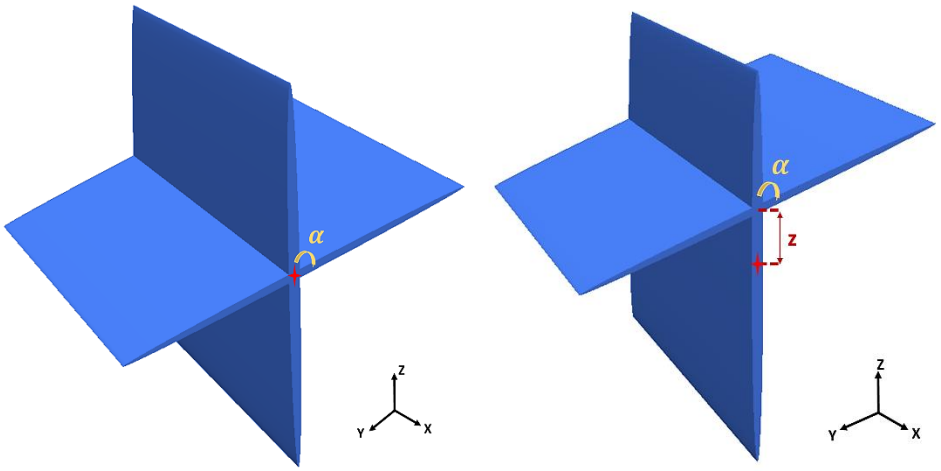

Figure 3.31: Sketch of a crossing-shaped fracture geometry consisting of a vertical fracture and an inclined bedding plane with approach angle α: (a) Injection point locates at the bedding plane; (b) Injection point has a z distance from the center of the bedding plane.

3.2.1 Approach Angle

Approach angle is defined as the intersection angle between the initial fracture direction and the bedding plane. In this subsection, we selected the fracture geometry shown in Figure 3.31 (a) and then chose different approach angles (α) to analyze the induced normal and shear stresses, the openings of the vertical fracture and oblique interface and also the shear displacement discontinuity along the oblique interface. Figures 3.32, 3.33 and 3.34 elaborates the contour map of normalized induced stresses acting on the normalized x-y plane when the approach angle $\alpha = 15°$, $\alpha = 30°$ and $\alpha = 45°$, respectively. The left figure depicts the normalized induced normal stress σ_{zz} acting on x-

y plane and the normalized induced shear stress τ_{xy} is shown in the right figures. Positive stress behaves as a compressive stress and negative value as a tensile stress.

Figure 3.35 (a) indicates the impact of approach angle on the normalized fracture width along the z direction. In this figure, we can observe that the vertical fracture width has a negative correlation with the approach angle. In other words, the minimum averaged fracture width can be obtained when the vertical fracture orthogonally contacts with the bedding plane. Width profile of the vertical fracture along the x direction is described in Figure 3.35 (b). Similarly, the vertical fracture width decreases as the increment of approach angle. Moreover, an unconspicuous width "trough" in the middle section of vertical fracture length can be observed if the approach angle is non-orthogonal, as a result of the induced compressive stress increases in that region. Figure 3.36 (a) and Figure 3.36 (b) illustrate the normalized opening of the interface and the normalized shear displacement discontinuity along the interface (x direction), respectively. In Figure 3.36 (a), the opening of the interface is positively correlated with the approach angle. When the approach angle is small ($\alpha = 15°$ and $\alpha = 30°$), a width "crest" is created in the region (-0.4, 0.4), due to the fact that the compressive stress induced by the vertical fracture suddenly decreases in this range. The width "crest" becomes a "trough" as the approach angle gradually increases to 45°. With the increment of the approach angle from 45° to 90°, the width "trough" becomes deeper because of a sudden increment of compressive stress acting on the bedding plane. Lee et al. (2018) indicated that hydraulic fracture with a larger approach angle has a wider width at the junction area of the hydraulic fracture and oblique vein, in the simulation results for veins with two different approach angles of 30°

and 45°. Moreover, from three left figures of Figures 3.32, 3.33 and 3.34, we can observe that the normalized induced compressive stress along the x direction decreases with the increment of approach angle from 15° to 45°, which also demonstrates that the opening of the interface is positively correlated with the approach angle. Figure 3.36 (b) indicates that a shear displacement discontinuity is created when the vertical fracture interacts with the oblique interface. There is no shear displacement discontinuity when the approach angle is orthogonal. We also observed that shear displacement discontinuity increases as the increment of the approach angle. Additionally, a "trough" of shear displacement discontinuity appears in the middle section area along the y direction. With increment of the approach angle, the curvature of this "trough" becomes larger. Simulation results from Lee et al. (2018) illustrated that more shear cracks would aggregate at the junction area with a larger approach angle, which also demonstrates the positive correlation between the shear sliding along the interface and approach angle in the non-orthogonal case. In addition, three right figures of Figures 3.32, 3.33 and 3.34 illustrate the normalized induced shear stress τ_{xy} along the interface becomes larger as the approaching angle increases from 15° to 45°, which also explains the "trough" depth of the shear displacement discontinuity is positively correlated with the approach angle. From Figure 3.36, we knew that larger shear displacement discontinuity makes the opening of the interface smaller. It demonstrates that the bedding plane is much more difficult to be opened and shear sliding also occurs more easily along the interface when the vertical fracture interacts with an oblique interface.

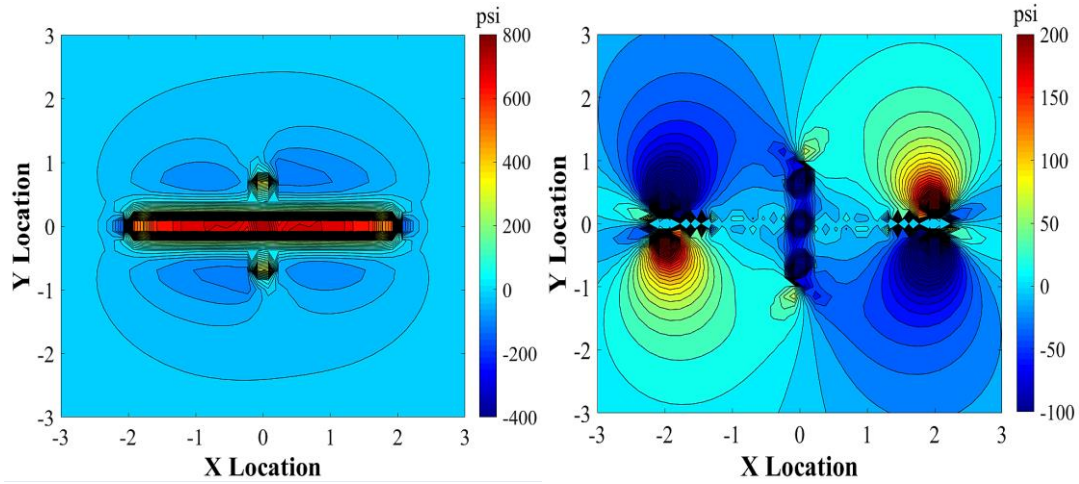

Figure 3.32: Induced stresses acting on normalized x-y plane induced by crossing-shaped fracture when approach angle $\alpha = 15°$ (a) Induced normal stress (σ_{zz}); (b) Induced shear stress (τ_{xy}).

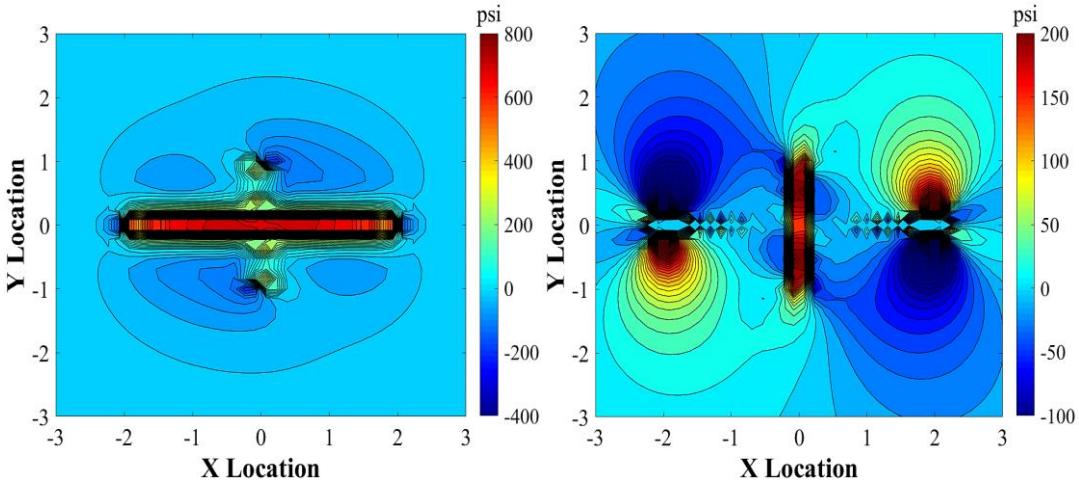

Figure 3.33: Induced stresses acting on normalized x-y plane induced by crossing-shaped fracture when approach angle $\alpha = 30°$ (a) Induced normal stress (σ_{zz}); (b) Induced shear stress (τ_{xy}).

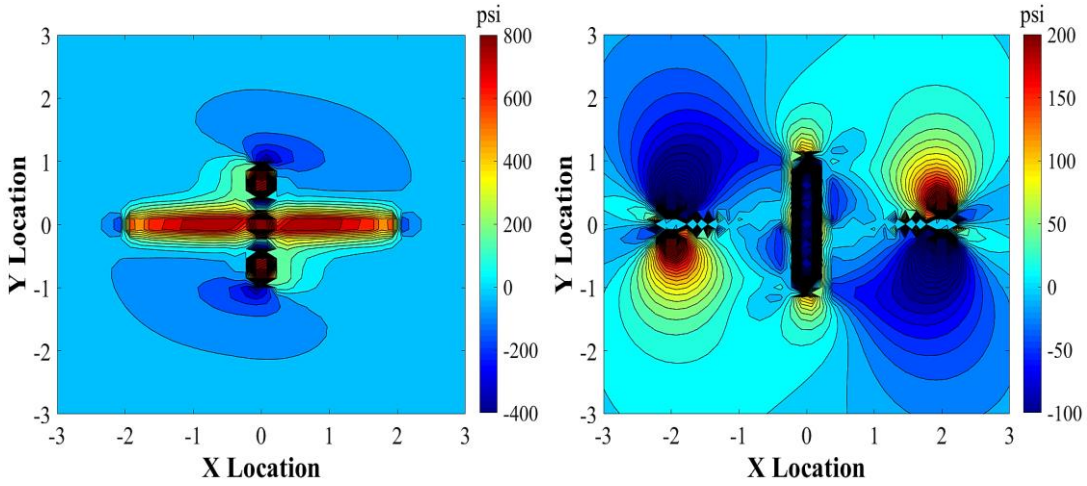

Figure 3.34: Induced stresses acting on normalized x-y plane induced by crossing-shaped fracture when approach angle $\alpha = 45°$ (a) Induced normal stress (σ_{zz}); (b) Induced shear stress (τ_{xy}).

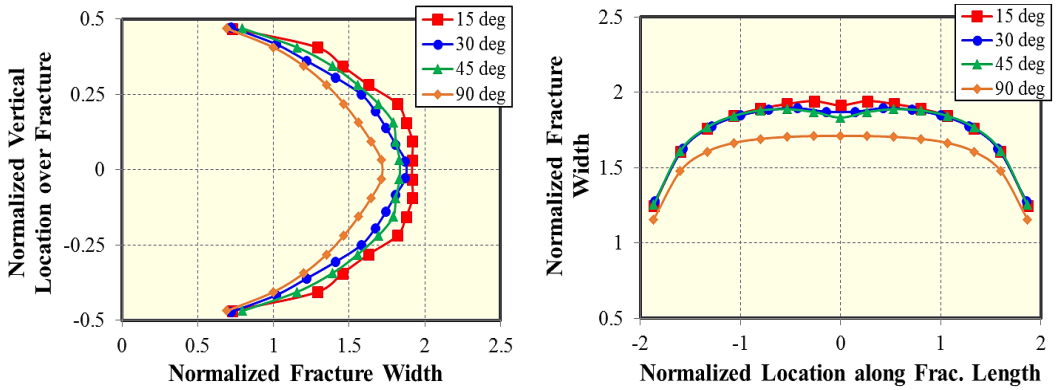

Figure 3.35: (a) Impact of approach angle on the normalized fracture width along the z direction; (b) Impact of approach angle on the normalized fracture width along the x direction.

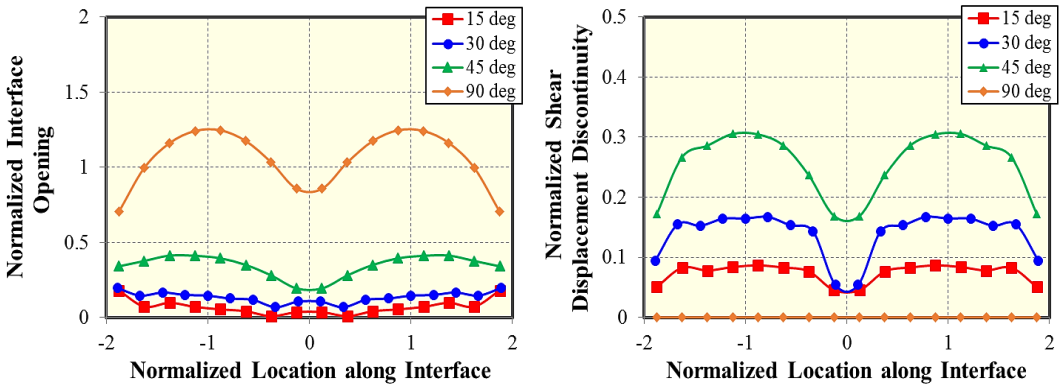

Figure 3.36: (a) Impact of approach angle on the normalized interface opening along the interface (x direction); (b) Impact of approach angle on the normalized shear displacement discontinuity along the interface (x direction).

3.2.2 Distance with the Injection Point

In this subsection, we selected the fracture geometry shown in Figure 3.31 (b). All required parameters are revealed in Table 3.1 and we only changed the value of Z/H ratio as 0, 0.25 and 0.4. Impact of Z/H ratio (the ratio of the distance between the center of the vertical fracture and the oblique interface to the fracture height) would be analyzed. This ratio can be regarded as an equivalent variable with the distance between the injection point and the interface during hydraulic fracture treatments. Figure 3.37 (a) elaborates the normalized width profiles of the vertical fracture along the z direction. A positive relation between the fracture width and Z/H ratio can be observed no matter the approach angle equals 45° or 90°. We also found that a width jump appears at the crossing position of the interface when the fracture geometry both satisfies that Z/H ratio does not equal zero and approach angle is orthogonal. This width jump is used for quantitatively calculating the interfacial sliding along the bedding plane, which is positively correlated with Z/H ratio when the approach angle equals 90°. Moreover, no obvious width jump occurs when the

vertical fracture non-orthogonally approaches with an inclined bedding plane, compared with the case of orthogonal approach angle. This is because the created shear displacement discontinuity along the bedding plane is smaller than that of orthogonal cases, as depicted in Figure 3.38 (b). Figure 3.37 (b) shows the normalized vertical fracture width along the x direction. Width alteration seems more obvious with the increment of Z/H ratio in the case of orthogonal approach angle. The normalized opening of interface (along the x direction) for different Z/H ratio and approach angle is described in Figure 3.38 (a). In the cases of orthogonal approach angle (labeled as yellow, light blue and light green colors), the opening of the interface is symmetric with $x = 0$. We observed a width "trough" in the middle section as a result of sudden increment of compressive stress acting on the interface. The "trough" depth is negatively correlated with Z/H ratio. Moreover, the opening of the interface is asymmetric with $x = 0$ if the approach angle equals $45°$ and Z/H ratio is not zero, due to the fact that the elevation of the interface makes the fracture geometry not symmetric any more. Figure 3.38 (b) illustrates the normalized shear displacement discontinuity along the interface (x direction). Compared with the case of orthogonal approach angle, the shear displacement discontinuity in the case of non-orthogonal approach angle is much smaller. In addition, the shear displacement discontinuity increases slightly with the increment of approach angle in the non-orthogonal case.

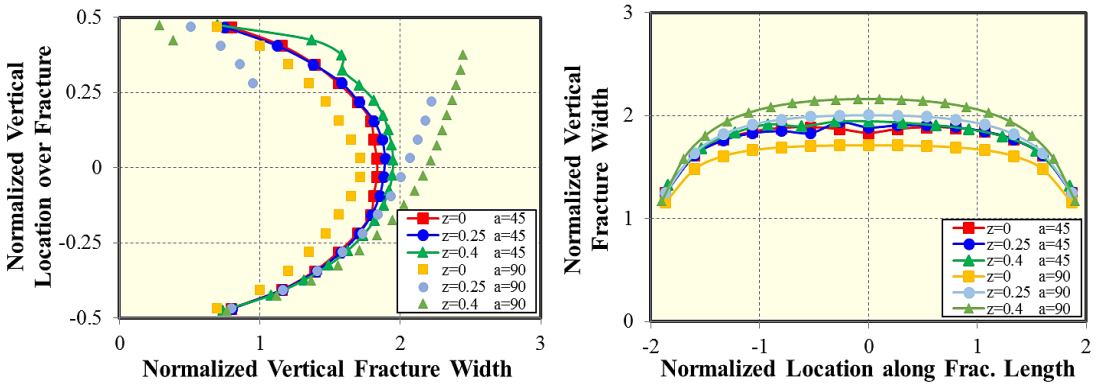

Figure 3.37: Impact of Z/H ratio for two different approach angle 45° and 90°: (a) Normalized vertical fracture width along the z direction; (b) Normalized vertical fracture width along the x direction.

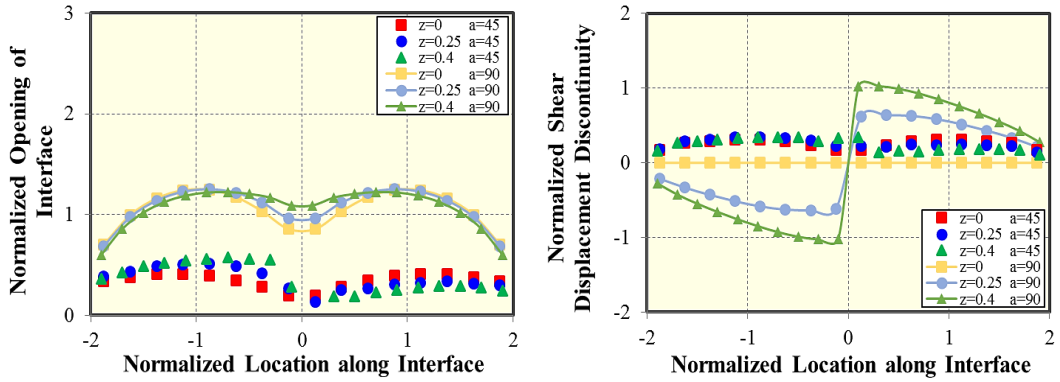

Figure 3.38: Impact of Z/H ratio for two different approach angle 45° and 90°: (a) Normalized opening of the bedding plane along the interface (x direction); (b) Normalized shear displacement discontinuity of the bedding plane along the interface (x direction).

3.2.3 Fluid Pressure within Fracture

Fluid pressure (P_f) is a significant parameter in determining the fracture width and further influence the fracture height growth. We would analyze the impact of fluid pressure on the width enlargement and restriction and also the shear displacement discontinuity along the interface, for two different approaching angle 45° and 90° in the fracture geometry depicted in Figure 3.31 (a). In Figures 3.39 and 3.40, we selected three

different fluid pressure 6000 psi, 6500 psi and 7000 psi. Figure 3.39 manifests that the vertical fracture width has a significantly positive correlation with the fluid pressure, irrespective of the approach angle. However, the change of fracture width is more noteworthy as the fluid pressure increases in the case of non-orthogonal angle. Interestingly, a "peak" is generated at the central region of the vertical fracture (region centered at z = 0 in Figure 3.39 (a) and region centered at x = 0 in Figure 3.39 (b)), as illustrated in Figure 3.39. In the case of non-orthogonal approach angle, we also observed an obvious "trough" in the centered region of the vertical fracture (along the x direction) when the fluid pressure is relatively small ($P_f = 6000$ psi). As we aggrandized the fluid pressure, it appears a transition from "trough" to "crest" (increasing fluid pressure from $P_f = 6500$ psi to $P_f = 7000$ psi). The opening of the bedding plane also positively related with the fluid pressure, as shown in Figure 3.40 (a). Fluid pressure has more impact on the tensile opening of the interface when the vertical fracture orthogonally approaches the horizontal interface, compared with the opening alteration in the case of non-orthogonal approach angle. Compressive stress acting on the middle section of the interface suddenly enlarges, which creates a "trough" of interface opening in this region. Figure 3.40 (b) shows that no shear sliding exists along the interface when approach angle equals 90°. However, shear displacement discontinuity is created as the interface becomes inclined and it has positive relation with fluid pressure. If the vertical fracture penetrates the oblique interface, larger fluid pressure makes the vertical fracture width much wider and the opening of the interface much narrower and more shear sliding appears along the interface,

which makes the fracture have more opportunity to divert its propagation pathway along the interface.

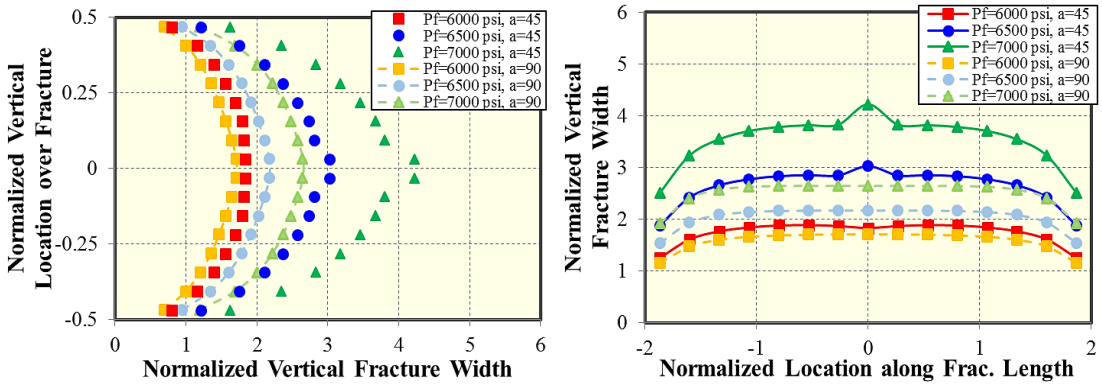

Figure 3.39: Impact of fluid pressure for two different approach angle 45° and 90°: (a) Normalized vertical fracture width along the z direction; (b) Normalized vertical fracture width along the x direction.

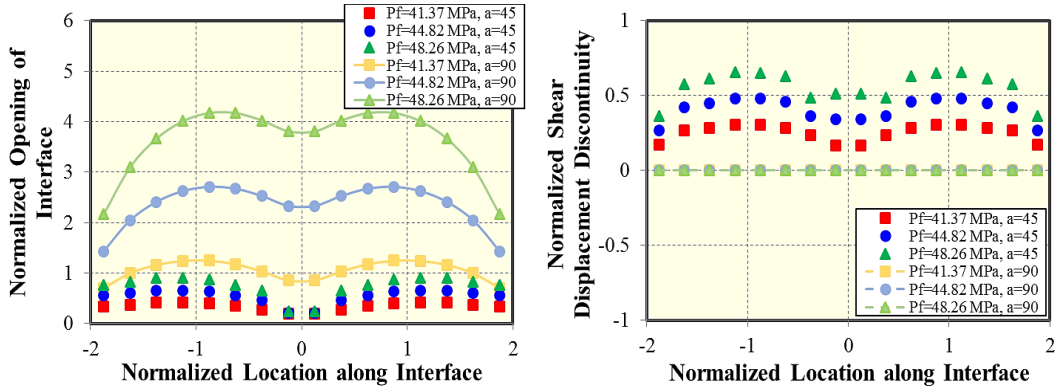

Figure 3.40: Impact of fluid pressure for two different approach angle 45° and 90°: (a) Normalized opening of the bedding plane along the interface (x direction); (b) Normalized shear displacement discontinuity of the bedding plane along the interface (x direction).

3.2.4 Young's Modulus

Young's modulus (YM), regarded as a significant rock property in the formation, has a big impact on the pathway of fracture propagation, which further determines the

fracture geometry. In this subsection, we used the fracture geometry from Figure 3.31 (a) and only altered the value of Young's modulus (1E6 psi, 3E6 psi and 6E6 psi) and kept other parameters equivalent with that in Table 3.1, in order to investigate the impact of Young's modulus on fracture width and shear displacements along the horizontal interface under the condition of two different approaching angle 45° and 90°. From Figures 3.41 (a) and 3.41 (b), we firstly found a negative correlation between the width of the vertical fracture and Young's modulus. Then we observed that the width of the vertical fracture increases as we changed the approach angle from orthogonal angle to non-orthogonal angle. However, the difference of the fracture width obtained from two different approach angle becomes smaller as the increment of Young's modulus. No evident alteration can be observed when Young's modulus reaches 6E6 psi. In terms of the opening of the interface, there is an obvious difference between width profile of the interface obtained from the case of orthogonal approach angle and that obtained from the non-orthogonal approach angle, with the same Young's modulus, as depicted in Figure 3.42 (a). Smaller Young's modulus makes the opening of the interface and shear displacement discontinuity both larger in the case of non-orthogonal approach angle, as illustrated in Figure 3.42 (a) and Figure 3.42 (b). At the same time, the impact of Young's modulus on the shear sliding along the interface is more obvious than its impact on the opening of the interface.

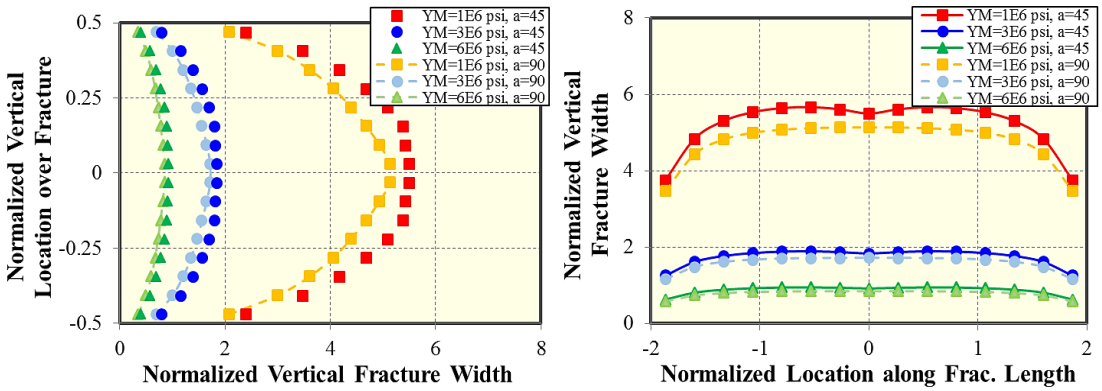

Figure 3.41: Impact of Young's modulus for two different approach angle 45° and 90°: (a) Normalized vertical fracture width along the z direction; (b) Normalized vertical fracture width along the x direction.

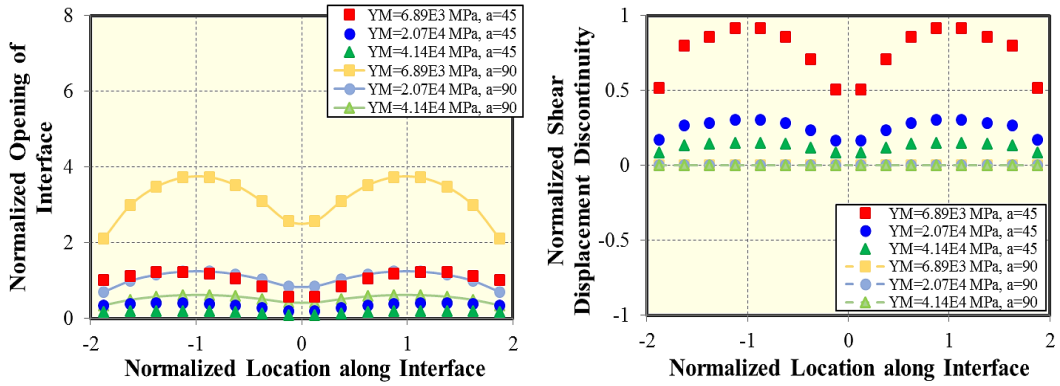

Figure 3.42: Impact of Young's modulus for two different approach angle 45° and 90°: (a) Normalized opening of the bedding plane along the interface (x direction); (b) Normalized shear displacement discontinuity of the bedding plane along the interface (x direction).

3.2.5 Poisson's Ratio

In this subsection, we kept using the parameters in Table 3.1 and altered the value of Poisson's ratio (PR) as 0.1, 0.25 and 0.4. Figures 3.43 and 3.44 indicate the impact of Poisson's ratio on the normalized vertical fracture width along the x and z directions, and the normalized interface opening and shear displacement discontinuity along the interface

(x direction), with two different approach angle 45° and 90°, respectively. Figure 3.43 shows that vertical fracture width has a negative relation with the Poisson's ratio. Vertical fracture width decreases as the approach angle transforms from the non-orthogonal angle to the orthogonal angle. In Figure 3.44, Poisson's ratio has almost no influence on the opening of the interface and shear displacement discontinuity along the interface in the case of non-orthogonal approach angle. The effect of Poisson' ratio on the opening of the interface becomes observable when the vertical fracture orthogonally contacts with the interface. Hence, Poisson' ratio is important of determining the opening of both the vertical fracture and interface, but it has less impact on the shear sliding along the interface, especially in the case of non-orthogonal approach angle.

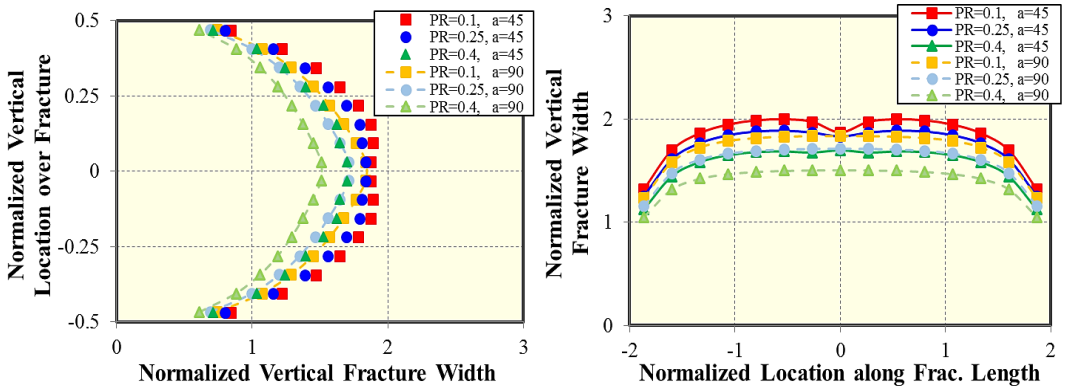

Figure 3.43: Impact of Poisson's ratio for two different approach angle 45° and 90°: (a) Normalized vertical fracture width along the z direction; (b) Normalized vertical fracture width along the x direction.

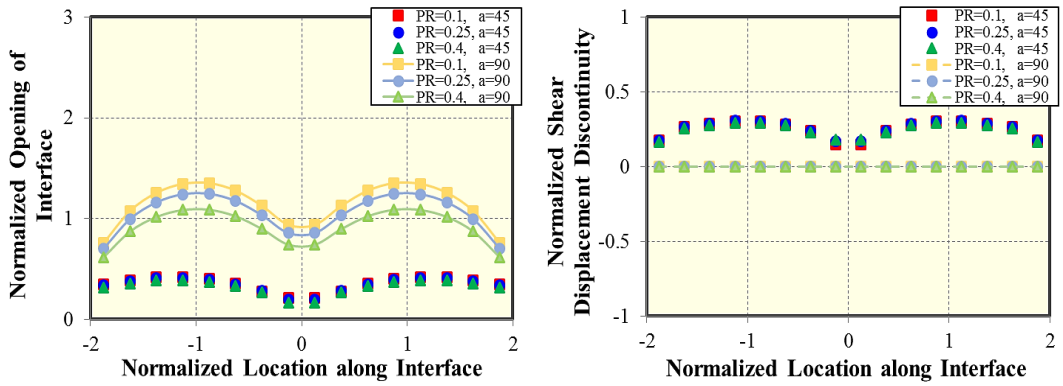

Figure 3.44: Impact of Poisson's ratio for two different approach angle 45° and 90°: (a) Normalized opening of the bedding plane along the interface (x direction); (b) Normalized shear displacement discontinuity of the bedding plane along the interface (x direction).

3.3 Conclusion

In this chapter, we did sensitivity analysis for the cases of orthogonal approach angle and non-orthogonal approach angle, respectively. In the section of orthogonal approach angle, we had a case of single fracture and single interface, a case of multiple fractures and single interface, and a case of single fracture and multiple interfaces. The width profile of fractures and the interaction of the vertical and horizontal fracture segments with predetermined fracture path were analyzed. We concluded that:

(1) A jump of fracture width on the vertical fracture at the crossing position of the interface, also defined as the interfacial sliding distance, is created due to the shear displacement discontinuities along the horizontal interface;

(2) Both widths of fracture segments and interfacial sliding distance are positively related with the distance between the center of the vertical fracture and the horizontal interface, half-length of horizontal fracture segment, the net pressure within fracture segments (vertical fracture or horizontal interface). However, Young's Modulus has a

negative relationship with both width of fracture segments and interfacial sliding distance;

(3) Compared with two fractures without the horizontal interface, the case of two vertical fractures with the interface has smaller fracture width under the interaction with the horizontal interface. Additionally, more energy would be dissipated in shearing sliding along the horizontal interface, which eventually causes the fracture height containment;

(4) For the case of multiple fractures, fracture spacing plays an important role in determining fracture width profiles, interfacial sliding distance and shear displacements along the fracture segments. Both widths of vertical fracture and horizontal interface are increasing with the increment of fracture spacing.

The 3-D fracture model developed by 3D DDM, also enables to simulate the interaction between the hydraulic fracture and oblique interface or other inclined frictional discontinuities. In the section of non-orthogonal approach angle with bedding planes, width profiles of both vertical fracture and interface segment were analyzed under the influence of different parameters, such as approaching angle, Z/H ratio, fluid pressure, Young's modulus and Poisson's ratio. We concluded that:

(1) Interface is much more difficult to be opened and shear sliding appears along the interface when the vertical fracture contacts with the oblique bedding plane;

(2) In the case of non-orthogonal approach angle, the opening of the interface has a positive correlation with the approach angle between the vertical fracture and the

interface. Moreover, shear displacement discontinuity along the interface increases with the increment of approach angle;

(3) Elevating the interface from the injection source has an unconspicuous impact on the interface opening and shear sliding along the interface in the case of non-orthogonal approach angle. In the orthogonal case, vertical fracture width is highly influenced by Z/H ratio;

(4) When the vertical fracture contacts with the oblique interface, fluid pressure has less influence on the opening of the interface but has an obvious effect on the shear sliding along the interface. Moreover, the increment of fluid pressure makes the alteration of vertical fracture more apparently in the case of non-orthogonal approach angle;

(5) Young's modulus and Poisson's ratio, as very significant formation properties, also influence the opening and the shear sliding of the interface. Compared with the case of non-orthogonal approach angle, the interface is easier to be opened in the orthogonal case, especially with a small Young's modulus. Smaller Young's modulus also creates larger shear displacement discontinuity along the interface when the approach angle is non-orthogonal. Additionally, Poisson' ratio does have an obvious effect on the interface opening and almost no effect on the shear sliding in the non-orthogonal case.

4. FLUID FLOW

This chapter includes five sections: fluid flow mathematical model, numerical modeling, model flowchart, iterative coupling algorithm of rock deformation and fluid flow, and conclusion. In terms of fluid flow mathematical model, two governing equations are introduced. There are governing equation of fluid flow inside the fracture and governing equation of material balance. In the section of numerical modeling, two-dimensional discretization and boundary condition at the bedding plane are described. Then model flow chart and iterative coupling algorithm are shown in the following sections.

4.1 Fluid Flow Mathematical Model

4.1.1 Governing Equations of Fluid Flow inside the Fracture

Figure 4.1 shows a hydraulic fracture geometry. Currie (1974) reformulated the Navier-Stokes equation for the case of the incompressible Newtonian fluid as,

$$\rho \frac{d\vec{v}}{dt} = \rho\vec{F} + \mu\nabla^2\vec{v} - \nabla p \tag{4.1}$$

where $\vec{\mathbf{v}} = (\mathrm{v_x}, \mathrm{v_y}, \mathrm{v_z})$ is the velocity vector**,** ρ is the fluid density, $\vec{\mathbf{F}}$ is the body force per unit mass, μ is the fluid viscosity, $\mathrm{p} = \mathrm{p(x, y, t)}$ is the pressure. $\rho \frac{d\vec{\mathbf{v}}}{dt}$ is the inertia part and $\rho\vec{\mathbf{F}}$ is the body force part. If we neglect the inertia and body forces, the equation above can be simplified as,

$$\nabla p = \mu\nabla^2\vec{v} \tag{4.2}$$

Additionally, we know that $\nabla^2\vec{\mathbf{v}}$ contains three components,

$$\nabla^2\vec{\boldsymbol{v}} = \frac{\partial^2 \boldsymbol{v}}{\partial x^2} + \frac{\partial^2 \boldsymbol{v}}{\partial y^2} + \frac{\partial^2 \boldsymbol{v}}{\partial z^2} \tag{4.3}$$

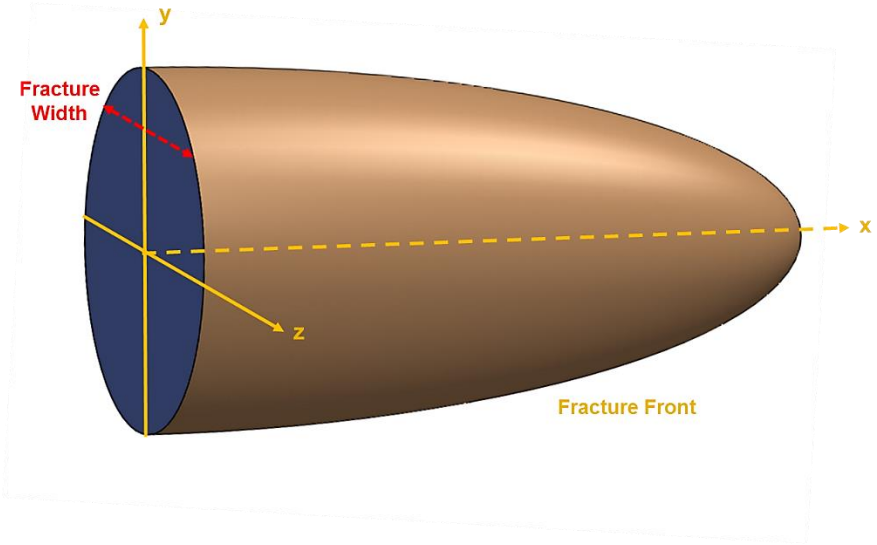

Figure 4.1: Hydraulic fracture geometry in three dimensions.

The derivatives of the velocity components in the x-y plane with respect to z are much larger than other derivatives of the velocity components because of the fluid pressure variation along the fracture width is negligible. Hence, Eq. (4.3) can be simplified as,

$$\nabla p = \mu\nabla^2\vec{\boldsymbol{v}} = \mu\left(\frac{\partial^2 \boldsymbol{v}}{\partial x^2} + \frac{\partial^2 \boldsymbol{v}}{\partial y^2} + \frac{\partial^2 \boldsymbol{v}}{\partial z^2}\right) \approx \mu\frac{\partial^2 \boldsymbol{v}}{\partial z^2} \tag{4.4}$$

Then Eq. (4.4) is split into two components along the x and y directions, respectively,

$$\frac{\partial p}{\partial x} = \mu\frac{\partial^2 v_x}{\partial z^2} = \mu\frac{\partial}{\partial z}\left(\frac{\partial v_x}{\partial z}\right) \tag{4.5}$$

$$\frac{\partial p}{\partial y} = \mu \frac{\partial^2 v_y}{\partial z^2} = \mu \frac{\partial}{\partial z}\left(\frac{\partial v_y}{\partial z}\right) \tag{4.6}$$

Integrate Eqs. (4.5) and (4.6) with respect to z, we can obtain the equations,

$$\int_0^z \frac{\partial p}{\partial x} dz = \int_0^z \mu \frac{\partial}{\partial z}\left(\frac{\partial v_x}{\partial z}\right) dz \;\Rightarrow\; \frac{\partial p}{\partial x} z = \mu \frac{\partial v_x}{\partial z} + k_1(x, y) \tag{4.7}$$

$$\int_0^z \frac{\partial p}{\partial y} dz = \int_0^z \mu \frac{\partial}{\partial z}\left(\frac{\partial v_y}{\partial z}\right) dz \;\Rightarrow\; \frac{\partial p}{\partial y} z = \mu \frac{\partial v_y}{\partial z} + k_2(x, y) \tag{4.8}$$

where k_1 and k_2 are arbitrary functions of coordinates x and y. Eqs. (4.7) and (4.8) can be integrated again with respect to z and we can obtain the equations,

$$\int_0^z \frac{\partial p}{\partial x} z dz = \int_0^z \left[\mu \frac{\partial v_x}{\partial z} + k_1(x, y)\right] dz \;\Rightarrow\; v_x = \frac{z^2}{2\mu}\frac{\partial p}{\partial x} + \frac{k_1(x,y)}{\mu} z + k_3(x, y) \tag{4.9}$$

$$\int_0^z \frac{\partial p}{\partial y} z dz = \int_0^z \left[\mu \frac{\partial v_y}{\partial z} + k_2(x, y)\right] dz \;\Rightarrow\; v_y = \frac{z^2}{2\mu}\frac{\partial p}{\partial y} + \frac{k_2(x,y)}{\mu} z + k_4(x, y) \tag{4.10}$$

where k_3 and k_4 are arbitrary functions of coordinates x and y. We assume that no slip occurs in the x direction on the surface of the fracture,

$$v_x = 0 \text{ , at } z = -\frac{w}{2} \text{ and } z = \frac{w}{2} \tag{4.11}$$

Hence, Eq. (4.9) can be formulated according to the boundary condition above,

$$\frac{1}{2\mu}\frac{\partial p}{\partial x}\left(\frac{w}{2}\right)^2 + \frac{k_1(x,y)}{\mu}\left(\frac{w}{2}\right) + k_3(x, y) = 0, \text{ when } z = \frac{w}{2} \tag{4.12}$$

$$\frac{1}{2\mu}\frac{\partial p}{\partial x}\left(-\frac{w}{2}\right)^2 + \frac{k_1(x,y)}{\mu}\left(-\frac{w}{2}\right) + k_3(x, y) = 0, \text{ when } z = -\frac{w}{2} \tag{4.13}$$

Then we can obtain the solution for $k_3(x, y)$ as,

$$k_3(x, y) = -\frac{1}{2\mu}\left(\frac{w}{2}\right)^2 \frac{\partial p}{\partial x} \tag{4.14}$$

Similarly, we also implement the same boundary condition along the y direction,

$$v_y = 0 \text{ , at } z = -\frac{w}{2} \text{ and } z = \frac{w}{2} \tag{4.15}$$

Eq. (4.10) can be formulated according to the boundary condition in Eq. (4.15),

$$\frac{1}{2\mu}\frac{\partial p}{\partial y}\left(\frac{w}{2}\right)^2 + \frac{k_2(x,y)}{\mu}\left(\frac{w}{2}\right) + k_4(x,y) = 0, \text{ when } z = \frac{w}{2} \tag{4.16}$$

$$\frac{1}{2\mu}\frac{\partial p}{\partial y}\left(-\frac{w}{2}\right)^2 + \frac{k_2(x,y)}{\mu}\left(-\frac{w}{2}\right) + k_4(x,y) = 0, \text{ when } z = -\frac{w}{2} \tag{4.17}$$

Then the solution of $k_4(x,y)$ can be obtained,

$$k_4(x,y) = -\frac{1}{2\mu}\left(\frac{w}{2}\right)^2 \frac{\partial p}{\partial x} \tag{4.18}$$

Eqs. (4.9) and (4.10) can be determined by the boundary conditions from Eqs. (4.11) to (4.18). Hence, the velocity profiles across the fracture width can be obtained as,

$$v_x = -\frac{1}{8\mu}[w^2 - 4z^2]\frac{\partial p}{\partial x} \tag{4.19}$$

$$v_y = -\frac{1}{8\mu}[w^2 - 4z^2]\frac{\partial p}{\partial y} \tag{4.20}$$

where $w = w(x,y,t)$ represents the fracture width (fracture opening). Thereafter we can derive the flow rates per unit length (m^2/s) in the x and y directions revealed as,

$$q_x = \int_{-\frac{w}{2}}^{\frac{w}{2}} v_x dz = \int_{-\frac{w}{2}}^{\frac{w}{2}} -\frac{1}{2\mu}\left[\left(\frac{w}{2}\right)^2 - z^2\right]\frac{\partial p}{\partial x}dz = \int_{-\frac{w}{2}}^{\frac{w}{2}} \left[-\frac{1}{2\mu}\left(\frac{w}{2}\right)^2\frac{\partial p}{\partial x} + \frac{z^2}{2\mu}\frac{\partial p}{\partial x}\right]dz$$

$$= \int_{-\frac{w}{2}}^{\frac{w}{2}} -\frac{1}{2\mu}\left(\frac{w}{2}\right)^2\frac{\partial p}{\partial x}dz + \int_{-\frac{w}{2}}^{\frac{w}{2}} \frac{z^2}{2\mu}\frac{\partial p}{\partial x}dz$$

$$= -\frac{1}{2\mu}\left(\frac{w}{2}\right)^2\frac{\partial p}{\partial x}\left(\frac{w}{2} - \left(\frac{w}{2}\right)\right) + \frac{1}{6\mu}\frac{\partial p}{\partial x}z^3\Big|_{-\frac{w}{2}}^{+\frac{w}{2}} = -\frac{w^3}{8\mu}\frac{\partial p}{\partial x} + \frac{w^3}{24\mu}\frac{\partial p}{\partial x}$$

$$= -\frac{w^3}{12\mu}\frac{\partial p}{\partial x}$$

…… (4.21)

$$q_y = \int_{-w/2}^{w/2} v_y dz = \int_{-w/2}^{w/2} -\frac{1}{2\mu}\left[\left(\frac{w}{2}\right)^2 - z^2\right]\frac{\partial p}{\partial y}dz = \int_{-\frac{w}{2}}^{\frac{w}{2}}\left[-\frac{1}{2\mu}\left(\frac{w}{2}\right)^2\frac{\partial p}{\partial y} + \frac{z^2}{2\mu}\frac{\partial p}{\partial y}\right]dz$$

$$= \int_{-\frac{w}{2}}^{\frac{w}{2}} -\frac{1}{2\mu}\left(\frac{w}{2}\right)^2\frac{\partial p}{\partial y}dz + \int_{-\frac{w}{2}}^{\frac{w}{2}}\frac{z^2}{2\mu}\frac{\partial p}{\partial y}dz$$

$$= -\frac{1}{2\mu}\left(\frac{w}{2}\right)^2\frac{\partial p}{\partial y}\left(\frac{w}{2} - \left(\frac{w}{2}\right)\right) + \frac{1}{6\mu}\frac{\partial p}{\partial y}z^3\Big|_{-\frac{w}{2}}^{+\frac{w}{2}} = -\frac{w^3}{8\mu}\frac{\partial p}{\partial y} + \frac{w^3}{24\mu}\frac{\partial p}{\partial y}$$

$$= -\frac{w^3}{12\mu}\frac{\partial p}{\partial y}$$

…… (4.22)

For simplification, Gu (1987) ignored the gravity term and spurt terms. Additionally, there is only one injection source (set at the center point of the first boundary element of a growing fracture). Figure 4.2 reveal the flow rate conservation within the fracture (Gu 1987). We have the balance equation of control volume as,

$$\left[q_x\Delta y - \left(q_x + \frac{\partial q_x}{\partial x}\Delta x\right)\Delta y\right] + \left[q_y\Delta x - \left(q_y + \frac{\partial q_y}{\partial y}\Delta y\right)\Delta x\right] = (\frac{\partial w}{\partial t} + q_L)\Delta x\Delta y \qquad (4.23)$$

Eq. (4.24), as a continuity equation of flow rate conservation, is reformulated after eliminating equivalent items from Eq. (4.23),

$$-\frac{\partial q_x}{\partial x} - \frac{\partial q_y}{\partial y} = \frac{\partial w}{\partial t} + q_L \qquad (4.24)$$

where $\frac{\partial w}{\partial t}$ represents the rate of fracture volume change and q_L represents the fluid leak-off rate which is from the fracture surfaces into the rock formation,

$$q_L = \frac{2C_L}{\sqrt{t-\tau(x,y)}} \tag{4.25}$$

where C_L is an experimentally determined leak-off coefficient and $\tau(x,y)$ is the time at which fluid leak-off begins at a point (x,y) on the fracture surface.

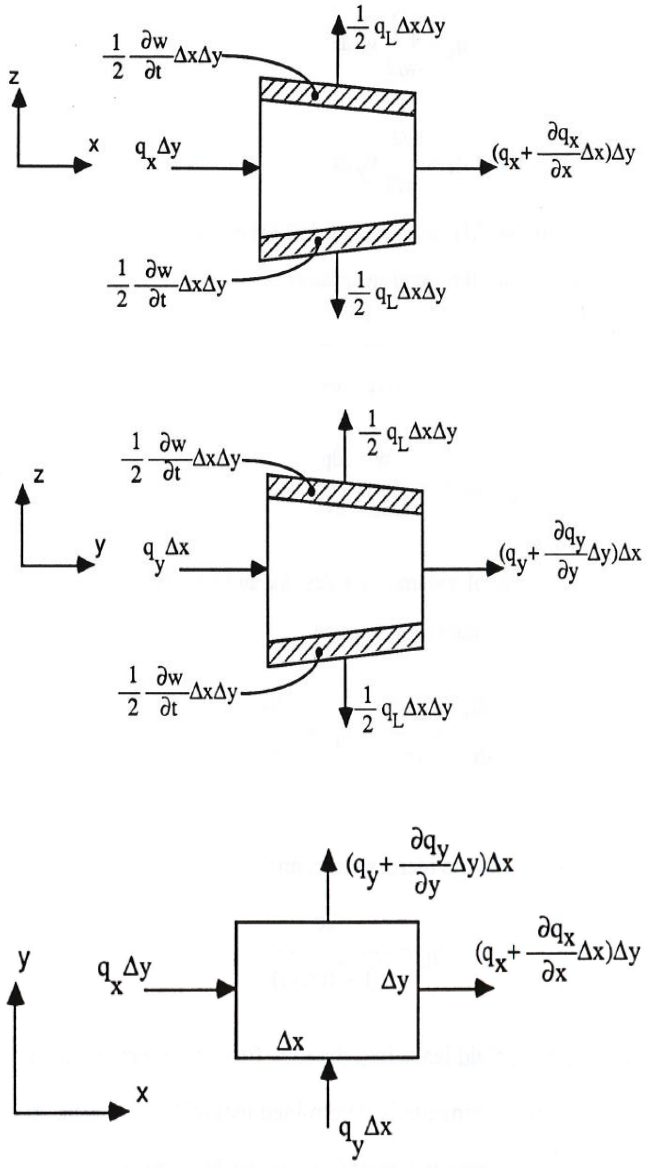

Figure 4.2: Flow rate conservation inside the fracture (Gu 1987).

Combining with the Eqs. (4.21), (4.22), (4.24) and (4.25), we obtain the simplified governing equation for the fluid motion inside the fracture,

$$\boldsymbol{\nabla} \cdot \left[\frac{w^3}{12\mu}\boldsymbol{\nabla} p\right] = \frac{\partial}{\partial x}\left[\frac{w^3}{12\mu}\frac{\partial p}{\partial x}\right] + \frac{\partial}{\partial y}\left[\frac{w^3}{12\mu}\frac{\partial p}{\partial y}\right] = \frac{\partial w}{\partial t} + \frac{2C_L}{\sqrt{t-\tau(x,y)}} \tag{4.26}$$

$$D(w) = \frac{w^3}{12\mu} \tag{4.27}$$

Additionally, the following cubic law equation governs the flow of incompressible fluid at the injection point,

$$-\frac{w^3(x,y,t)}{12\mu}\nabla p(x,y,t) = Q(x,y,t) \tag{4.28}$$

where ∇ represents two-dimensional gradient operator, $\mathrm{p(x, y, t)}$ is the fluid pressure inside the fracture, μ is the fluid viscosity, $\mathrm{Q(x, y, t)}$ represents the fluid injection rate.

4.1.2 Governing Equations of Material Balance

We can combine Eqs. (4.26) and (4.28) and then do the integration as,

$$\int_{\Omega(t)} \frac{\partial w}{\partial t} dV = \int_{\Omega(t)} [\boldsymbol{\nabla} \cdot [D(w)\boldsymbol{\nabla} p] - \frac{2C_L}{\sqrt{t-\tau(x,y)}} + \delta(x,y)Q(x,y,t)]dV \tag{4.29}$$

Divergence theorem can be applied as,

$$\iiint_V (\boldsymbol{\nabla} \cdot \vec{\boldsymbol{F}})dV = \oiint_S (\vec{\boldsymbol{F}} \cdot \vec{\boldsymbol{n}})\, dS \tag{4.30}$$

Then the first term of the right-hand side of Eq. (4.29) can be written as,

$$\int_{\Omega(t)} [\boldsymbol{\nabla} \cdot [D(w)\boldsymbol{\nabla} p]dV = \int_{\partial\Omega(t)} D(w)\, \boldsymbol{\nabla} p\, \vec{\boldsymbol{n}}\, dS = \int_{\partial\Omega(t)} D(w)\, \frac{\partial p}{\partial \vec{\boldsymbol{n}}}\, dS \tag{4.31}$$

In terms of Dirac delta function, we know that,

$$\delta^2(x,y) = \begin{cases} 0 & x^2 + y^2 \neq 0 \\ \infty & x^2 + y^2 = 0 \end{cases} \tag{4.32}$$

Then the third term of the right-hand side of Eq. (4.29) is reformulated as,

$$\int_{\Omega(t)} \delta(x,y)Q(x,y,t)\,dV = Q(x,y,t)\int_{\Omega(t)} \sqrt{\delta(x)\delta(y)}\,dV = Q(x,y,t) \tag{4.33}$$

Application of Leibnitz's rule gives,

$$\frac{d}{dx}\left(\int_{y_0}^{y_1} f(x,y)dy\right) = \int_{y_0}^{y_1} f_x(x,y)dy \tag{4.34}$$

Hence, the deformation formulas of the left-land side of Eq. (4.29) can be written as,

$$\int_{\Omega(t)} \frac{\partial w}{\partial t}dV = \frac{\partial}{\partial t}\int_{\Omega(t)} wdV \tag{4.35}$$

Hence, we obtain the deformed formulas for Eq. (4.29),

$$\frac{\partial}{\partial t}\int_{\Omega(t)} wdV = \int_{\partial\Omega(t)} D(w)\frac{\partial p}{\partial \vec{\boldsymbol{n}}}dS - \int_{\Omega(t)} \frac{2C_L}{\sqrt{t-\tau(x,y)}}dV \tag{4.36}$$

The boundary condition as the fluid flux at the fracture front equals to zero,

$$-D(w)\frac{\partial p}{\partial \vec{\boldsymbol{n}}} = -\frac{w^3}{12\mu}\frac{\partial p}{\partial \vec{\boldsymbol{n}}} = 0,\ \partial\Omega_f \tag{4.37}$$

Thus, we have,

$$\int_{\partial\Omega(t)} D(w)\frac{\partial p}{\partial \vec{\boldsymbol{n}}}dS = 0 \tag{4.38}$$

Then we get new formulas for Eq. (4.29),

$$\frac{\partial}{\partial t}\int_{\Omega(t)} wdV = Q(x,y,t) - \int_{\Omega(t)}\left[\frac{2C_L}{\sqrt{t-\tau(x,y)}}\right]dV = Q(x,y,t) - \int_{\Omega(t)}\frac{2C_L}{\sqrt{t-\tau(x,y)}}dV$$

$$= Q(x,y,t) - \int_{\Omega(t)}\frac{2C_L}{\sqrt{t-\tau(x,y)}}dV$$

…… (4.39)

We do integration with respect to time from the beginning of the pumping process, we obtain the solvability condition,

$$\int_0^t [\frac{\partial}{\partial t}\int_{\Omega(t)} w dV]dt = \int_0^t [Q(x,y,t) - \int_{\Omega(t)} \frac{2C_L}{\sqrt{t-\tau(x,y)}} dV]dt$$

$$\int_{\Omega(t)} w dV = \int_0^t Q(x,y,t)\, dt - \int_0^t \int_{\Omega(t)} \frac{2C_L}{\sqrt{t-\tau(x,y)}} dV\, dt$$

…… (4.40)

The equation of global conservation of mass can be formulated as,

$$\int_0^t Q(x,y,t)dt = \int_{\Omega(t)} w\, dV + \int_0^t \left[\int_{\Omega(t)} \frac{2C_L}{\sqrt{t-\tau(x,y)}} dV\right] dt \quad (4.41)$$

4.2 Numerical modeling

4.2.1 Two-Dimensional Discretization

According to Eq. (4.41), the fracture volume balance equation below can be implemented for calculating the pumping time for each time step, which is then used to determine the change rate of fracture width in Eq. (4.28),

$$\sum_{i=1}^{N^{(T)}} A_i^{(T)} w_i^{(T)} - \sum_{i=1}^{N^{(T-1)}} A_i^{(T-1)} w_i^{(T-1)} = q_0 \Delta t - \sum_{i=1}^{N^{(T)}} A_i^{(T)} \left(\frac{2C_L}{\sqrt{t-\tau(x,y)}}\right)_i^{(T)} \Delta t \quad (4.42)$$

where $A_i^{(T)}$ and $w_i^{(T)}$ represent the cross-section area and the opening of boundary element i at the current time step, respectively. $A_i^{(T-1)}$ and $w_i^{(T-1)}$ represent the cross-section area and the opening of boundary element i at the previous time step, respectively. $N^{(T)}$ and $N^{(T-1)}$ are total number of boundary element at the current time step and at the previous time step, respectively. q_0 is the pumping rate at the current time step, Δt is the pumping

time for current time step. Moreover, Eq. (4.26) can be written as a matrix equation form via finite difference method (LeVeque 2007),

$$\tilde{T}\vec{p} = \vec{b} \tag{4.43}$$

where $\tilde{T}$ is the transmissibility matrix, $\vec{p}$ is the vector representing the pressure within each boundary element of the fracture, $\vec{b}$ is the vector including the term of the rate of fracture volume change.

According to Eq. (4.26), we can do two-dimensional discretization along the x and y directions (neglecting the leak-off term), as shown in Figure 4.3,

$$\begin{aligned}\frac{\partial w_{i,j}}{\partial t} &= \frac{\partial}{\partial x}\left[\frac{w^3}{12\mu}\cdot\frac{\partial p}{\partial x}\right] + \frac{\partial}{\partial y}\left[\frac{w^3}{12\mu}\cdot\frac{\partial p}{\partial y}\right] \\ &= \frac{1}{48\mu\Delta x_{i,j}}\left[\frac{\left(w_{i-1,j}+w_{i,j}\right)^3}{a_{i-1,j}+a_{i,j}}\left(p_{i-1,j}-p_{i,j}\right)\right. \\ &\quad \left. - \frac{\left(w_{i,j}+w_{i+1,j}\right)^3}{a_{i,j}+a_{i+1,j}}\left(p_{i,j}-p_{i+1,j}\right)\right] \\ &\quad + \frac{1}{48\mu\Delta y_{i,j}}\left[\frac{\left(w_{i,j}+w_{i,j-1}\right)^3}{b_{i,j}+b_{i,j-1}}\left(p_{i,j}-p_{i,j-1}\right)\right. \\ &\quad \left. - \frac{\left(w_{i,j}+w_{i,j+1}\right)^3}{b_{i,j}+b_{i,j+1}}\left(p_{i,j}-p_{i,j+1}\right)\right]\end{aligned} \tag{4.44}$$

where $w_{i,j}$, $p_{i,j}$, $a_{i,j}$, $b_{i,j}$ represent the width of element (i,j), the presure of element (i,j), the half-length of element (i,j) and the half-height of element (i,j), respectively.

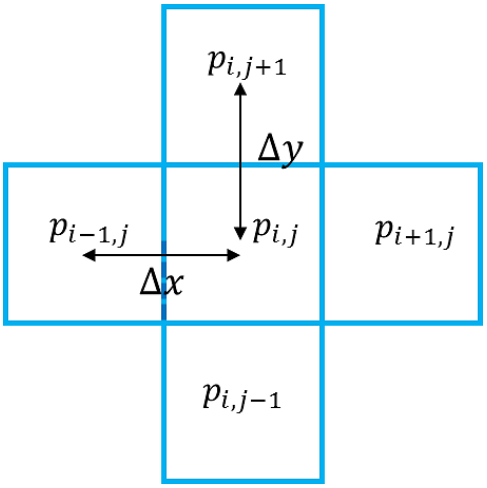

Figure 4.3 2D discretization example.

Then Eq. (4.44) can be reformulated as,

$$\frac{\partial w_{i,j}}{\partial t} = T_{i-\frac{1}{2},j}\left(p_{i-1,j} - p_{i,j}\right) - T_{i+\frac{1}{2},j}\left(p_{i,j} - p_{i+1,j}\right) + T_{i,j-\frac{1}{2}}\left(p_{i,j} - p_{i,j-1}\right)$$

$$- T_{i,j+\frac{1}{2}}\left(p_{i,j} - p_{i,j+1}\right)$$

$$= \left(T_{i-\frac{1}{2},j}\right)p_{i-1,j} + \left(T_{i+\frac{1}{2},j}\right)p_{i+1,j} + \left(-T_{i,j-\frac{1}{2}}\right)p_{i,j-1} + \left(T_{i,j+\frac{1}{2}}\right)p_{i,j+1}$$

$$+ \left(-T_{i-\frac{1}{2},1} - T_{i+\frac{1}{2},1} + T_{i,j-\frac{1}{2}} - T_{i,j+\frac{1}{2}}\right)p_{i,j}$$

$$= \boldsymbol{a_{i,j}}p_{i-1,j} + \boldsymbol{b_{i,j}}p_{i+1,j} + \boldsymbol{c_{i,j}}p_{i,j-1} + \boldsymbol{d_{i,j}}p_{i,j+1} + \boldsymbol{e_{i,j}}p_{i,j}$$

…… (4.45)

$$\boldsymbol{a_{i,j}} = T_{i-\frac{1}{2},j} = \frac{1}{48\mu\Delta x_{i,j}}\frac{\left(w_{i-1,j} + w_{i,j}\right)^3}{a_{i-1,j} + a_{i,j}} = \frac{\left(w_{i-1,j} + w_{i,j}\right)^3}{96\mu(a)^2}$$

$$\boldsymbol{b_{i,j}} = T_{i+\frac{1}{2},j} = \frac{1}{48\mu\Delta x_{i,j}}\frac{\left(w_{i,j} + w_{i+1,j}\right)^3}{a_{i,j} + a_{i+1,j}} = \frac{\left(w_{i,j} + w_{i+1,j}\right)^3}{96\mu(a)^2}$$

$$\boldsymbol{c_{i,j}} = -T_{i,j-\frac{1}{2}} = -\frac{1}{48\mu\Delta y_{i,j}}\frac{\left(w_{i,j}+w_{i,j-1}\right)^3}{b_{i,j}+b_{i,j-1}} = \frac{\left(w_{i,j}+w_{i,j-1}\right)^3}{96\mu(b)^2}$$

$$\boldsymbol{d_{i,j}} = T_{i,j+\frac{1}{2}} = \frac{1}{48\mu\Delta y_{i,j}}\frac{\left(w_{i,j}+w_{i,j+1}\right)^3}{b_{i,j}+b_{i,j+1}} = \frac{\left(w_{i,j}+w_{i,j+1}\right)^3}{96\mu(b)^2}$$

$$\boldsymbol{e_{i,1}} = \left(-T_{i-\frac{1}{2},1} - T_{i+\frac{1}{2},1} + T_{i,j-\frac{1}{2}} - T_{i,j+\frac{1}{2}}\right) = -\boldsymbol{a_{i,j}} - \boldsymbol{b_{i,j}} - \boldsymbol{c_{i,j}} - \boldsymbol{d_{i,j}}$$

…… (4.46)

4.2.2 Boundary Condition at Bedding Planes

Boundary condition at the bedding planes should be taken into consideration when discretizing the continuity equation. In terms of the vertical fracture element which is not fully surrounded by other elements, the pressure at its end without adjacent element is assumed as the horizontal minimum stress σ_{hmin}. In terms of the interface element, its pressure at the end without adjacent element is assumed as the over-burden stress σ_v. In this subsection, four examples of discretization are illustrated in Figures (4.4) and (4.5).

Figure 4.4 indicates the case that one vertical fracture element i both adjoins with the element $(i+1)$ on the interface and another vertical fracture element $(i-1)$. According to the continuity equation shown in Eq. (4.26), we did discretization on these three boundary elements only along the y direction (height direction) and obtained the formulas revealing the relation between the width and pressure as,

$$\frac{\partial}{\partial y}\left[\frac{w^3}{12\mu}\frac{\partial p}{\partial y}\right] = \frac{1}{12\mu\Delta y}\left[\frac{\left(\frac{w_{i+1}+w_i}{2}\right)^3}{\left(\frac{0+b_i}{2}\right)}(p_{i+1}-p_i) - \frac{\left(\frac{w_i+w_{i-1}}{2}\right)^3}{\left(\frac{b_i+b_{i-1}}{2}\right)}(p_i-p_{i-1})\right]$$

$$= \frac{1}{12\mu\left(\frac{\Delta y}{2}\right)}\frac{\left(\frac{w_{i+1}+w_i}{2}\right)^3}{\left(\frac{0+b_i}{2}\right)}(p_{i+1}-p_i)$$

$$-\frac{1}{12\mu\Delta y}\frac{\left(\frac{w_i+w_{i-1}}{2}\right)^3}{\left(\frac{b_i+b_{i-1}}{2}\right)}(p_i-p_{i-1})$$

$$= \frac{(w_i)^3}{96\mu\left(\frac{\Delta y}{2}\right)\left(\frac{b_i}{2}\right)}(p_{i+1}-p_i) - \frac{(w_i+w_{i-1})^3}{96\mu\Delta y\left(\frac{b_i+b_{i-1}}{2}\right)}(p_i-p_{i-1})$$

…… (4.47)

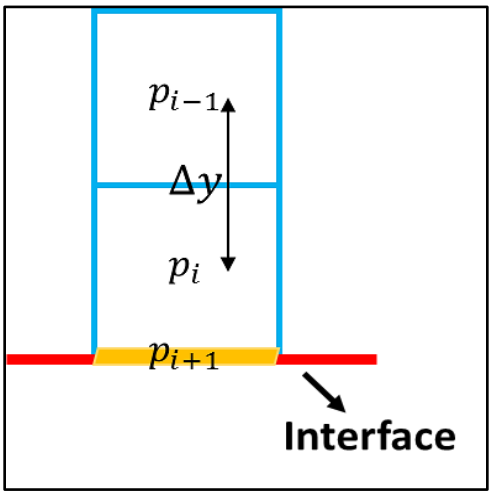

Figure 4.4: Vertical fracture element i adjoins with the interface element $(i+1)$ and another vertical fracture element $(i-1)$.

Figure 4.5 depicts the case that an interface element i both adjoins with two vertical fracture elements $(i-1)$ and $(i+1)$ at its upper end and lower end. In this case, we can do discretization along the y direction as,

$$\frac{\partial}{\partial y}\left[\frac{w^3}{12\mu}\frac{\partial p}{\partial y}\right] = \frac{1}{12\mu(\frac{\Delta y}{2})}\left[\frac{\left(\frac{w_{i+1}+w_i}{2}\right)^3}{(\frac{b_{i+1}+b_i}{2})}(p_{i+1}-p_i) - \frac{\left(\frac{w_i+w_{i-1}}{2}\right)^3}{(\frac{b_i+b_{i-1}}{2})}(p_i-p_{i-1})\right]$$

$$= \frac{1}{12\mu(\frac{\Delta y}{2})}\frac{\left(\frac{w_{i+1}+w_i}{2}\right)^3}{(\frac{b_{i+1}+b_i}{2})}(p_{i+1}-p_i)$$

$$- \frac{1}{12\mu(\frac{\Delta y}{2})}\frac{\left(\frac{w_i+w_{i-1}}{2}\right)^3}{(\frac{b_i+b_{i-1}}{2})}(p_i-p_{i-1})$$

$$= \frac{(w_{i+1})^3}{96\mu(\frac{\Delta y}{2})(\frac{b_{i+1}}{2})}(p_{i+1}-p_i) - \frac{(w_{i-1})^3}{96\mu(\frac{\Delta y}{2})(\frac{b_{i-1}}{2})}(p_i-p_{i-1})$$

…… (4.48)

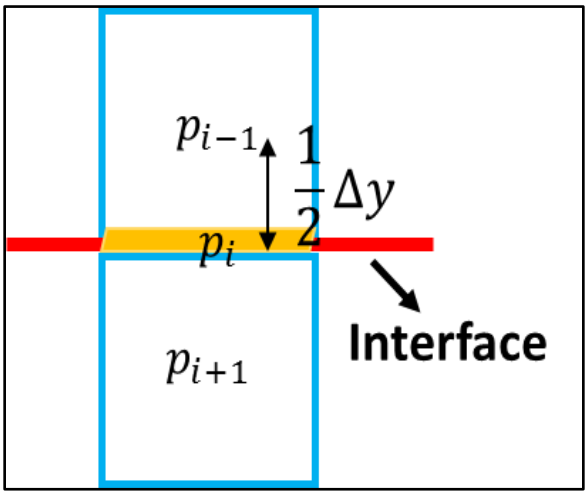

Figure 4.5: Interface element i both adjoins with one vertical fracture element $(i-1)$ at its upper end and another vertical fracture element $(i+1)$ at its lower end.

4.3 Model Flowchart

Figure 4.6 shows the flowchart of fluid flow model. First, we had the calculated fracture width profile from the rock deformation section (3D DDM), then we used fracture volume balance equation to determine the pumping time at current time step, then continuity equation and boundary condition are applied to construct the transmissibility matrix, then a solver is implemented for determining the fluid pressure for each boundary elements on both vertical fractures and horizontal bedding planes.

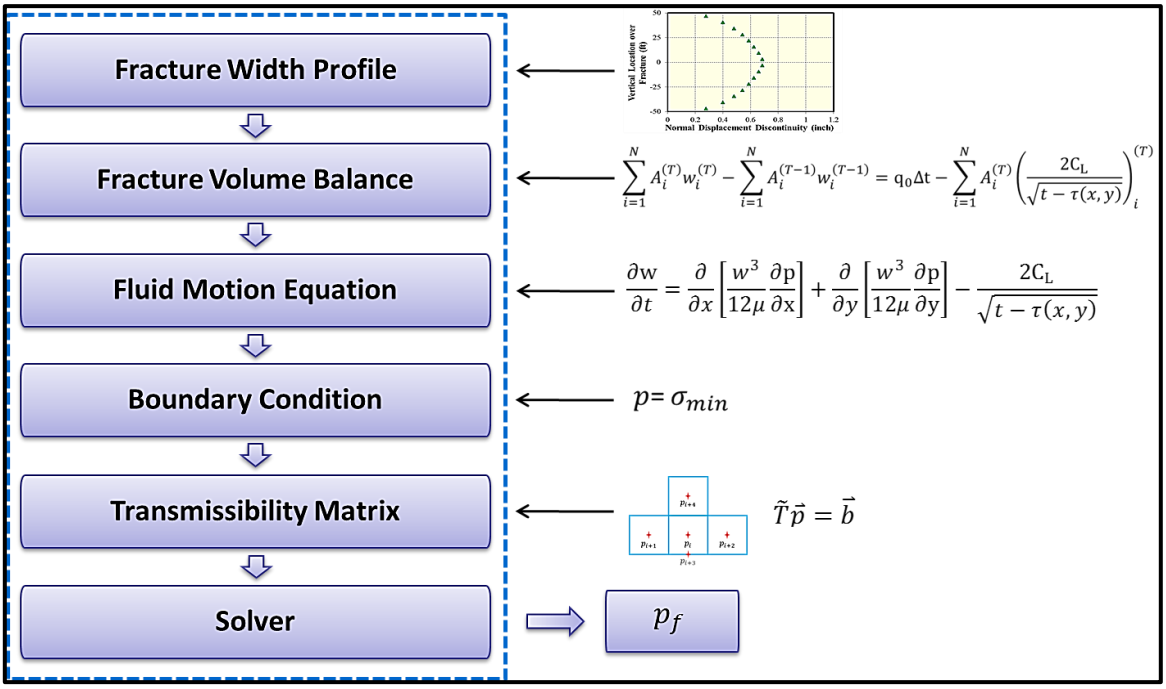

Figure 4.6: Flowchart of fluid flow.

4.4 Iterative Coupling Algorithm of Rock Deformation and Fluid Flow

An iterative algorithm (such as Picard iteration) was applied to couple the rock deformation and fluid flow at every updated time step. First we calculated the difference

of updated fracture width and previous calculated fracture width. If the convergence criterion is not satisfied, we modified the fracture width as

$$w_{k+1} = (1-\alpha)w_{k-1} + \alpha w_k \tag{4.49}$$

where α is a retardation coefficient ranging from 0 to 1 that prevents sudden jump or extreme fluctuations in fracture width. If the convergence criterion fails, decreasing this coefficient can improve convergence.

Figure 4.7 illustrates the workflow of the main algorithm in 3D hydraulic fracture propagation model. First, we had input parameters as fracture properties (dimension and angle of each boundary element on the fracture), fluid properties (viscosity, pumping rate) and formation properties (Young' modulus, Poisson's ratio, location of the bedding layers). Second, we plugged all inputs into the main algorithm, which was labeled by orange color and utilized to couple the rock deformation and fluid flow together. In the main algorithm, we did initialization and then used the fluid pressure calculated from last time step to obtain the initial fracture width for the current time step, via 3D DDM. The fracture volume balance equation can be used to determine the pumping time for current time step. Next, finite difference method is implemented to obtain the updated fluid pressure for each boundary element and 3D DDM is used again to calculate the updated fracture width. Convergence testing causes further Picard iteration to update a new fracture width as an input into the fracture volume balance equation when the change in fracture width is above the tolerance. Convergence below the tolerance advances the calculation to the next time step. After each time step, we could generate the output illustrated in the green dashed box, which includes the profiles of both the fracture width

and fluid pressure, and also the plots of the pressure-time and the width-time at the injection point.

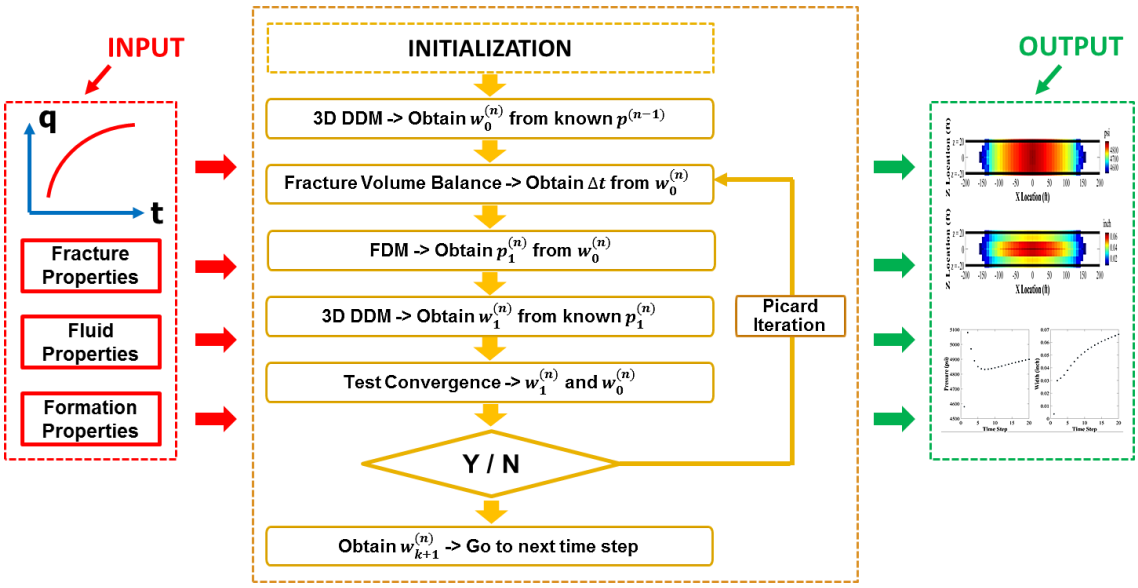

Figure 4.7: Flowchart of three-dimensional hydraulic fracture propagation model which includes input, main algorithm and output.

4.5 Conclusion

In this chapter, the mathematical derivation of flow rate conservation was firstly introduced. Then material balance equation was derived from the global conservation of mass in order to calculate the pumping time for each time step. Finite difference method was implemented to do discretization based on the continuity equations. Combining with the calculated pumping time and the width profile determined by the rock deformation, transmissibility matrix was constructed and then a solver was applied to calculate the fluid pressure for each boundary element on the fracture geometry. An iterative algorithm, aiming at checking the difference of updated fracture width and previous calculated

fracture width, was applied to couple the rock deformation and fluid flow at every updated time step. If the convergence criterion is not satisfied, fracture width was modified.

5. FRACTURE PROPAGATION MODEL

In this chapter, based on a new three-dimensional dynamic fracture propagation model developed in chapter 4, effects of weak bedding planes on fracture propagation were investigated. Comparison between the developed model and the PKN model showed good agreement. Our fracture propagation model was utilized to investigate the impact of different controlling parameters on hydraulic fracture propagation. These parameters include pumping rate, fluid viscosity, and Young's modulus. In each case, we analyzed the fracture width profile at the injection point and that near the junctions (intersection area between the vertical fracture and the bedding plane), the opening of the boundary element along the bedding planes which connects with the boundary element on the vertical fracture, the pressure distribution within the fracture and also the shear displacement discontinuities along the bedding planes. Additionally, our model enables assessment of the pumping rate required to ensure the fracture width at junctions and along intersected bedding planes which is sufficient for proppant transport, which also avoiding the potential bridging and screen-out of the proppant at the junctions.

5.1 Model Validation with PKN Model

For static fracture geometry, we calculated normal displacement discontinuity (fracture width) and induced stresses for a plane-strain fracture using 3D DDM and 2D analytical method in order to validate the 3D model. The numerical solution from 3D DDM has a good match with the 2D analytical solution in chapter 2 (Tang et al. 2017). In

terms of dynamic fracture propagation, we utilized PKN model for validation. The required input parameters for the PKN model are given in Table 5.1. Eqs. (5.1) to (5.3) are used to calculate fracture half-length, fracture width at the injection point and fluid pressure at the injection source, respectively (Valko and Economides 1995).

$$L = 0.524\left(\frac{Q^3 E}{\mu(1-\upsilon^2){h_f}^4}\right)^{0.2} t^{0.8} \tag{5.1}$$

$$w = 3.04\left(\frac{Q^2(1-\upsilon^2)\mu t}{E h_f}\right)^{0.2} \tag{5.2}$$

$$P = \sigma_{hmin} + 1.52\left(\frac{Q^2 E^4 \mu t}{(1-\upsilon^2)^4 {h_f}^6}\right)^{0.2} \tag{5.3}$$

Parameter	Value	Unit
Young's modulus	3.0E+06	psi
Poisson's ratio	0.25	Dimensionless
Viscosity	20	cp
Fracture Height	40	ft
Injection Rate	20	bbl/min

Table 5.1− Required parameters of the PKN model for validation.

For the PKN model, the fracture height is a constant (40 ft) and the fracture only propagates laterally. For the 3D DDM model, the fracture both propagates vertically and laterally at the beginning, it stops vertical growth when it contacts with the bedding planes and then it only grows laterally. Figure 5.1 illustrates the relation between the half-length of the fracture and the pumping time. The averaged relative error of 3D DDM model compared with the PKN model is approximately 3.5%.

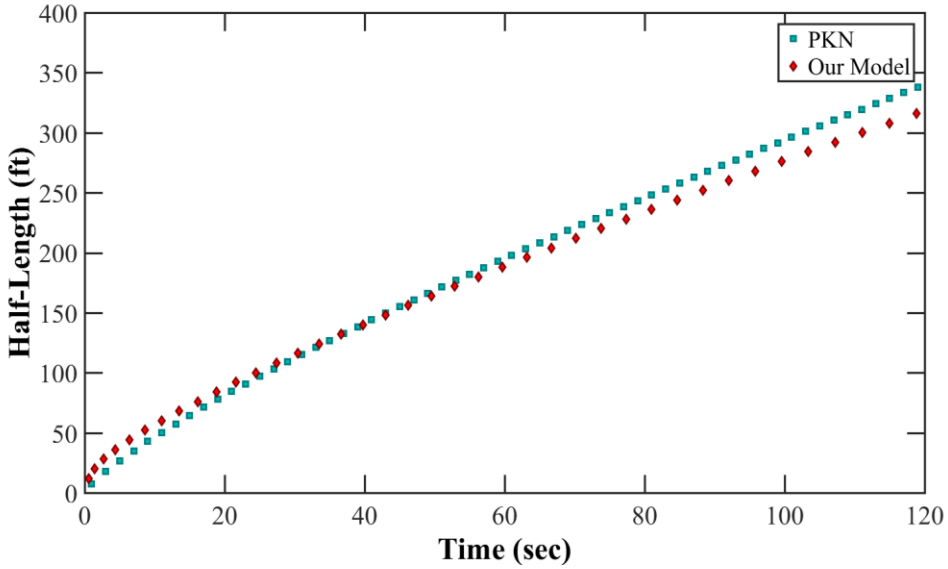

Figure 5.1: Comparison of the half-length of the fracture between PKN model and 3D DDM model.

Figures 5.2 (a) and 5.2 (b) indicate the profiles of pressure-time and width-time at the injection point, respectively. The averaged relative error of 3D DDM model is approximately as 5.1% for the pressure comparison and as 5.4% for the width comparison. From Figures 5.1 and 5.2, it reveals that our coupled model has a good match with the PKN model.

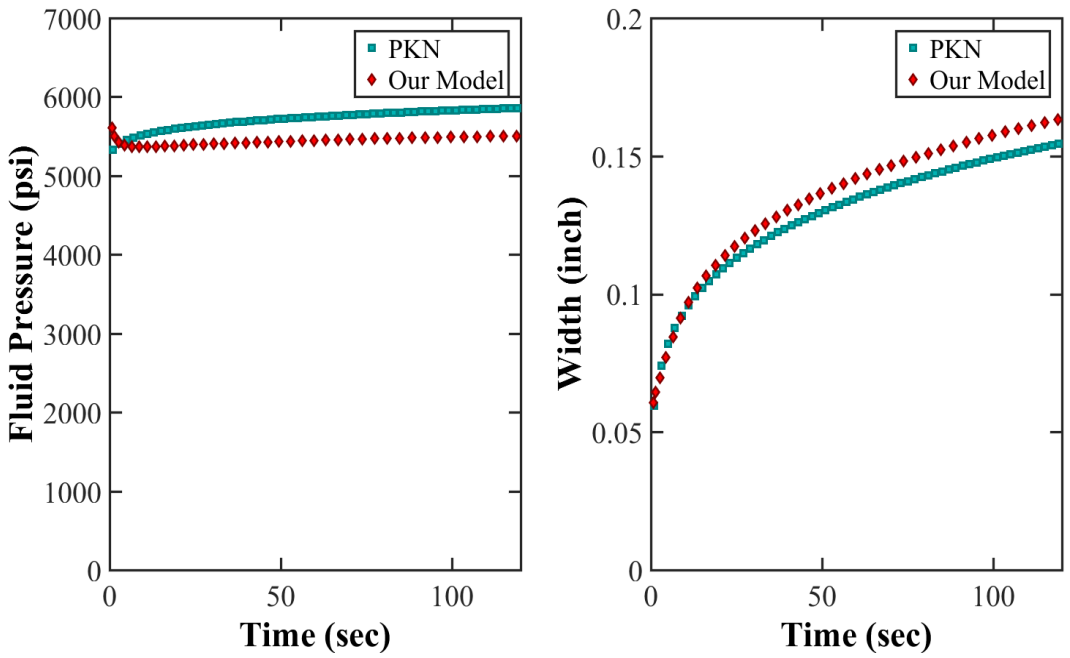

Figure 5.2: (a) Comparison of the fluid pressure within the fracture at the injection source; (b) Comparison of the fracture width at the injection source.

5.2 Base Case Analysis

In this section, we investigated the base case of a vertical fracture interacting with two symmetric bedding planes (I-shaped fracture geometry), as depicted in Figure 5.3. Injection source, junctions and bedding planes are shown by different colors in this figure. Junction, labeled as a red color, is the intersection area of the vertical fracture tip and the bedding planes. The fracture propagates vertically and laterally at the beginning. When the vertical fracture contacts with the bedding planes, the interface at the junction area is opened and fluid would infiltrate into the interface. During the fluid percolation into the bedding planes, shear displacement discontinuities would be created along the planes. In this case, we only accounted for the condition of the vertical fracture arrested by the bedding layers and its propagation along the bedding planes, and then studied the profiles

of displacement discontinuities (fracture width and shear displacement discontinuities) and pressure at different locations in the I-shaped fracture geometry. The required parameters in the base case are shown in Table 5.2.

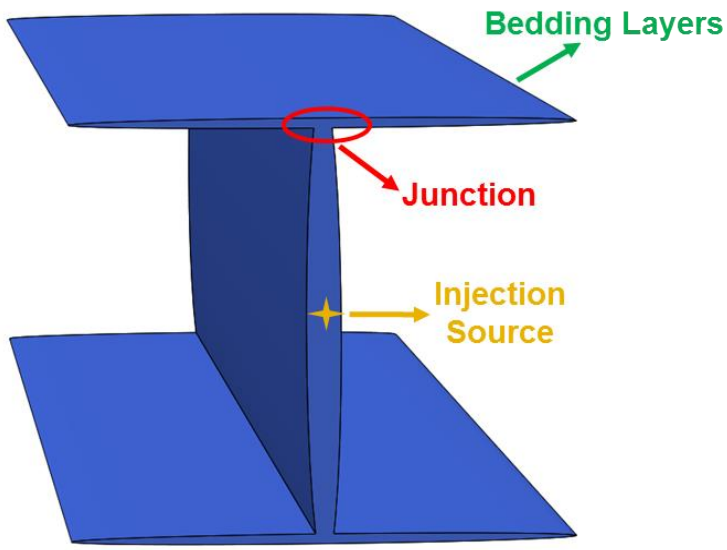

Figure 5.3: The geometry of an I-shaped fracture (one vertical fracture and two horizontal bedding planes).

Parameter	Value	Unit
Young's modulus	3.0E+06 (2.068E+10)	psi (Pa)
Poisson's ratio	0.25	Dimensionless
Viscosity	20 (0.02)	cp (Pa · sec)
Injection Rate	30 (0.052)	bbl/min (m^3/sec)
Maximum horizontal stress	5000 (3.447 E+7)	psi (Pa)
Minimum horizontal stress	5000 (3.447 E+7)	psi (Pa)
Over-burden stress	5000 (3.447 E+7)	psi (Pa)
Rock toughness	262.7 (1.0E+6)	psi · $\sqrt{ft}$ (Pa · $\sqrt{m}$)
Vertical location of upper interface	56 (17.069)	ft (m)
Vertical location of lower interface	-56 (-17.069)	ft (m)

Table 5.2− Required parameters for the base case (I-shaped fracture geometry).

Figures 5.4 and 5.5 show the three-dimensional visualizations of pressure profile and width profile of an I-shaped fracture at the end of injection, respectively. From Figure 5.5, we observed that the width of the vertical fracture is much larger than that of the bedding planes.

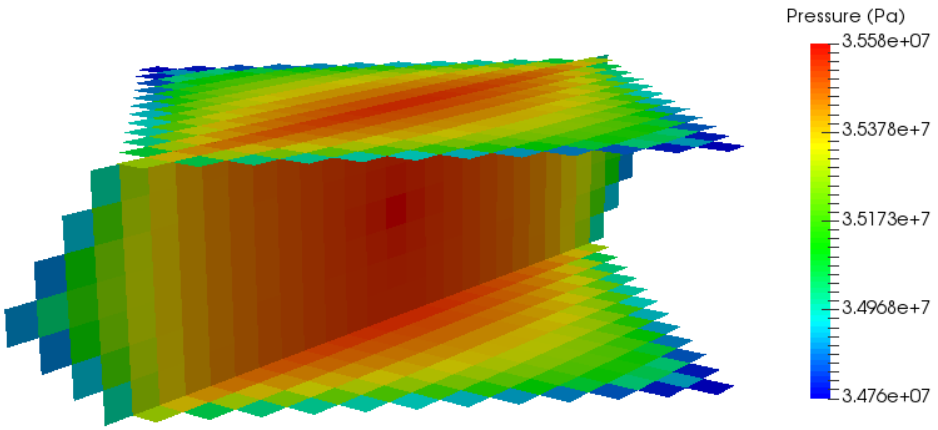

Figure 5.4: Pressure profile of the I-shaped fracture (one vertical fracture and two symmetric horizontal bedding planes) at the end of pumping treatment.

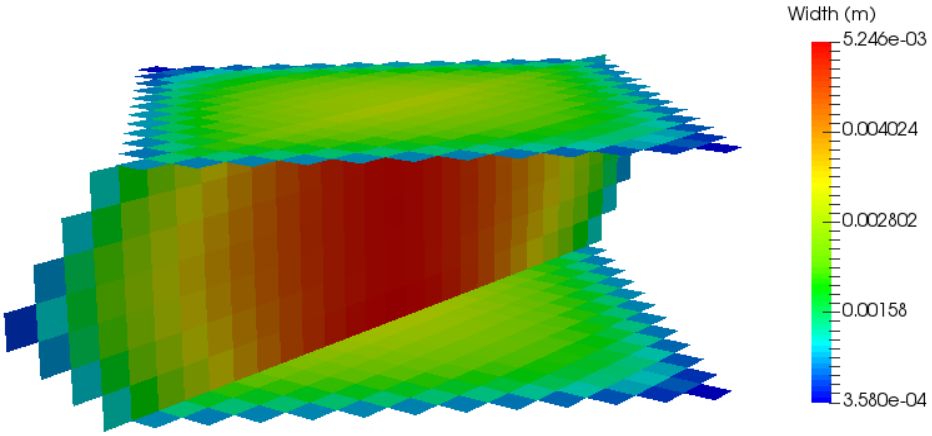

Figure 5.5: Width profile of the I-shaped fracture (one vertical fracture and two symmetric horizontal bedding planes) at the end of pumping treatment.

Two sub-figures in Figure 5.6 illustrate the displacement discontinuities profile and pressure profile at different location of the I-shaped fracture, respectively. In Figure 5.6 (a), "Vertical Width 1", "Vertical Width 2", "Interface Opening" and "Interface Shearing" represent the vertical fracture width at the injection point, the vertical fracture width at the junction area, the opening of the bedding plane at the junction area, the shear displacement discontinuities along the bedding plane at the junction area. In Figure 5.6 (b), "Vertical Pressure 1", "Vertical Pressure 2", "Interface Pressure" represent the vertical fracture pressure at the injection point, the vertical fracture pressure at the junction area, the pressure of the bedding plane at the junction area. In Figure 5.6 (a), we observed that displacement discontinuities in the four cases increase with increment of pumping time. At the early stage of injection, the vertical fracture width at the injection point is larger than other three displacement discontinuities. During the interim and later period of the treatment, the width of the vertical fracture at the junction area grows faster than that of

vertical fracture at the injection point. Moreover, we found that the vertical fracture width at the junction area is far greater than the opening of the bedding planes, identically observed from Figure 5.5. At the junction area, shear displacement discontinuities along the bedding plane is larger than the opening of the plane, which illustrates that the shear sliding plays a dominant role compared with the tensile opening of the bedding plane. Figure 5.6 (b) shows the pressure profiles at different locations of the I-shaped fracture. At the injection point, the fluid pressure drops rapidly at the early stage of injection and then decreases slightly from the interim period to the end of injection. At the junction area, the pressure of the vertical fracture is equivalent with the pressure at the opening of the interface.

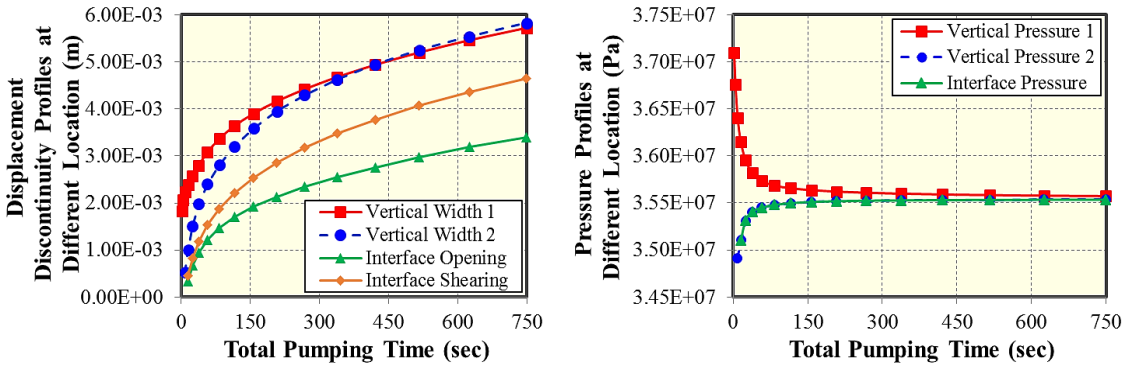

Figure 5.6: (a) Displacement discontinuity profiles at different locations of the I-shaped fracture; (b) Pressure profiles at different locations of the I-shaped fracture.

Figure 5.7 (a) indicates the profiles of displacement discontinuities of the vertical fracture along the fracture length direction at the end of injection. We labeled the fracture width of the vertical fracture as a red color and the shear displacement discontinuities as a blue color. Along the fracture length direction (across the centerline of the vertical

fracture), shear displacement discontinuities would not be generated and fracture width decreases quickly as it is far away from the fracture center. Along the upper bedding plane, both the opening of the interface and the shear displacement discontinuities of the interface would decrease as the lateral location moves away from the fracture center, as observed in Figure 5.7 (b).

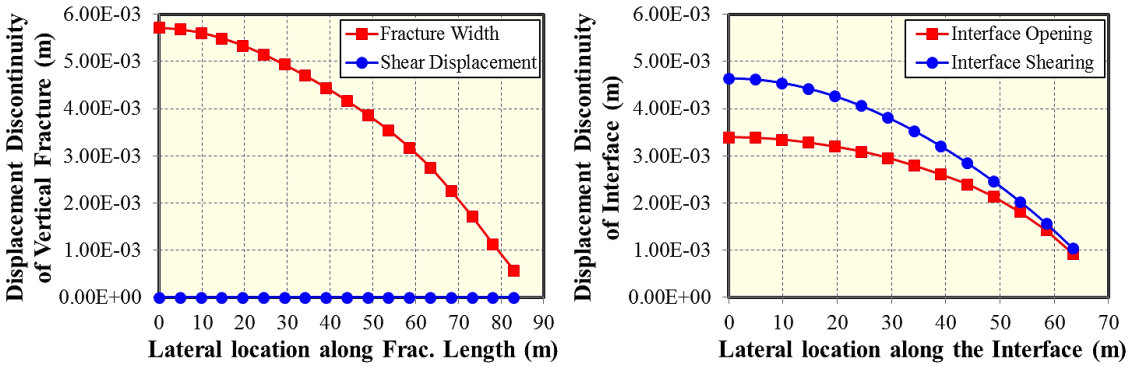

Figure 5.7: (a) Displacement discontinuity profiles of the vertical fracture along its length direction at the end of injection; (b) Displacement discontinuity profiles of the upper bedding planes along the interface at the end of injection.

5.3 Controlling Parameters Analysis

In this section, we investigated the case of one vertical fracture and two symmetric bedding planes (I-shaped fracture geometry) and studied the effects of different parameters (pumping rate, fluid viscosity, and Young's modulus) on the width profile of the vertical fracture, opening of horizontal bedding planes and also shear displacement discontinuities along the bedding planes.

5.3.1 Fluid Pumping Rate

In terms of sensitivity analysis for pumping rate (pr), three values are given as 10 bbl/min, 20 bbl/min, and 30 bbl/min. Other parameters are the same with those in the base case. In this case, we utilized pumping fluid volume instead of pumping time to represent the lateral coordinate, and then investigated the impact of pumping rate on other variables (vertical coordinate) such as width and pressure of the vertical facture at the injection point, width and pressure of the vertical facture at the junction area, opening and pressure of the bedding plane at the junction area, shear displacement discontinuities along the bedding plane at the end of injection.

Figure 5.8 (a) elaborates the impact of pumping rate on the vertical fracture width at the injection point and we found that the vertical fracture width increases with the increment of pumping fluid volume. Moreover, the vertical fracture width is positively correlated with the pumping rate with equivalent fluid volume. However, the pressure of the vertical fracture at the injection point drops rapidly as the pumping fluid volume increases, which is illustrated in Figure 5.8 (b). A positive relation between the pressure of the vertical fracture and the pumping rate is observed when the fluid volume is the same.

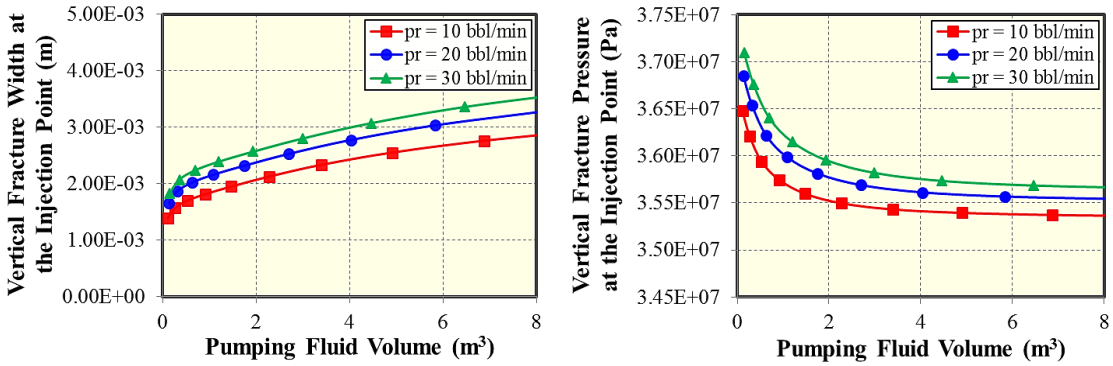

Figure 5.8: (a) Impact of pumping rate on the width of vertical fracture at the injection point; (b) Impact of pumping rate on the pressure of vertical fracture at the injection point.

Two sub-figures in Figure 5.9 indicate the impact of pumping rate on the width and pressure of the vertical fracture at the junction area, respectively. Both width and pressure of the vertical fracture at the junction area are positively related with the pumping fluid volume as the pumping rate is kept as a constant. In Figure 5.9 (a), the increment of the vertical fracture width at the junction area is obvious as the pumping rate increases from 10 bbl/min to 20 bbl/min. Continuously increment of pumping rate from 20 bbl/min to 30bbl/min makes the change of the vertical fracture width relatively smaller compared with the width alteration from 10 bbl/min to 20 bbl/min. Figure 5.9 (b) shows the pressure profile of the vertical fracture at the junction area, which has a similar trend as shown in Figure 5.9 (a). With the increment of the fluid volume, the pressure of the vertical fracture increases rapidly at the early-stage of the pumping treatment and then aggrandizes slightly during the interim and later period of the stimulation. Moreover, we observed that more fluid volume is required for the vertical fracture contacting with the bedding planes as the

pumping rate increases, although we knew that the time of the vertical fracture intersecting with the bedding planes is less if a larger pumping rate is given.

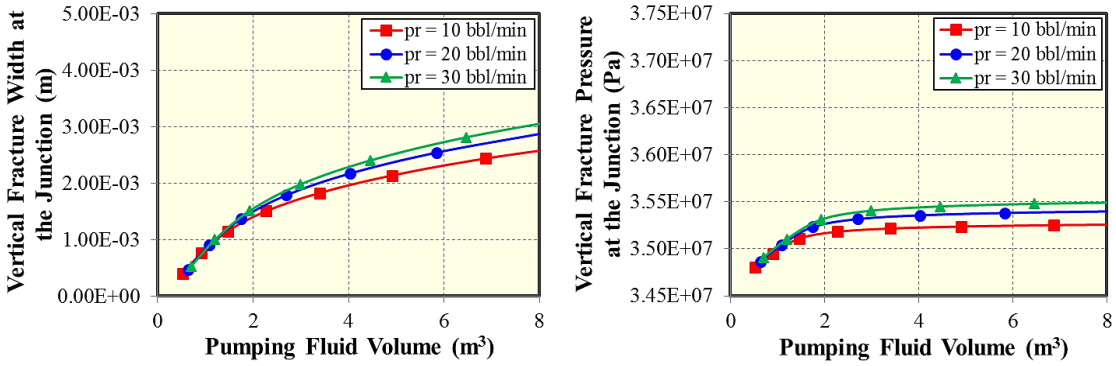

Figure 5.9: (a) Impact of pumping rate on the width of vertical fracture at the junction area; (b) Impact of pumping rate on the pressure of vertical fracture at the junction area.

When the vertical fracture is arrested by the bedding planes, the interface is opened at the junction area and the fluid would infiltrate into the bedding planes, and then the shear displacement discontinuities are generated along the bedding planes. Figure 5.10 (a) manifests that the impact of pumping rate on the opening of the bedding planes at the junction area when the vertical fracture is simultaneously arrested by two symmetric bedding planes. Interface at the junction area is opened wider as more fluid is injected into the formation. The opening of the bedding plane changes slightly as the pumping rate increases from 10 bbl/min to 30 bbl/min. Nevertheless, the pressure of fluid percolated into the interface alters less apparent as the pumping rate increases, which illustrated in Figure 5.10 (b).

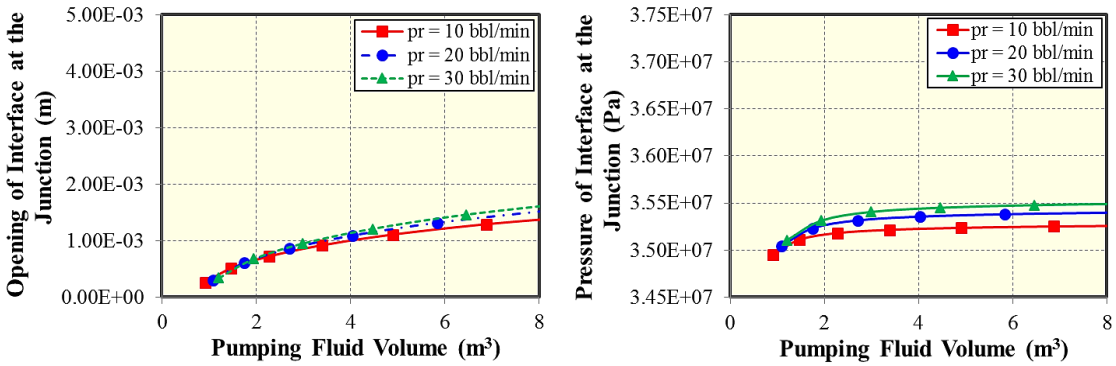

Figure 5.10: (a) Impact of pumping rate on the opening of bedding plane at the junction area; (b) Impact of pumping rate on the pressure of bedding plane at the junction area.

Figure 5.11 introduces the impact of pumping rate on the opening of the bedding plane and also the shear displacement discontinuities, along the upper bedding plane at the end of injection treatment, respectively. From Figure 5.11 (a), we observed that the opening of the bedding plane decreases as the lateral location along the upper interface is far away from the junction area. The maximum width of the bedding plane is obtained at the junction area. At the same lateral location along the upper interface, the opening of the bedding plane is positively correlated with the pumping rate. Similarly, Figure 5.11 (b) shows a positive relation between the pumping rate and the shear displacement discontinuities along the upper interface. The maximized value of shear displacement discontinuities is also obtained at the junction area. At the same position along the upper interface, the shear displacement discontinuities is larger than the opening of the interface, which provides an insight that the shear sliding plays a dominant role compared with the tensile mechanism of the bedding plane. Additionally, the width of the vertical fracture at the junction area is approximately twice than the opening of the bedding plane at the end

of the pumping treatment, as observed from Figure 5.9 (a) and Figure 5.10 (a). This observation provides a guideline for selecting appropriate size range of the proppant during the stimulation treatment.

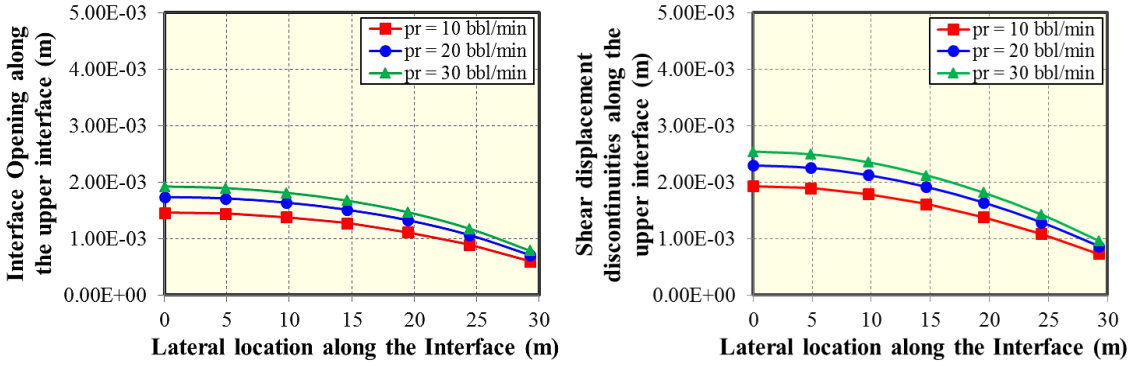

Figure 5.11: (a) Impact of pumping rate on the interface opening along the upper bedding plane at the end of injection treatment; (b) Impact of pumping rate on the shear displacement discontinuities along the upper bedding plane at the end of injection treatment.

5.3.2 Fluid Viscosity

In the section of analyzing the effect of fluid viscosity (miu), we chose three different values as 5 cp, 20 cp, 100 cp. Figures 5.12 (a) and (b) separately demonstrate the impact of fluid viscosity on the width and the pressure of the vertical fracture at the injection point. The lateral coordinate represents the total pumping time. From Figure 5.12 (a), we observed a positive relation between the fluid viscosity and the width of the vertical fracture at the injection point, with the same total pumping time. The pressure of the vertical fracture also increases with the augment of fluid viscosity, as illustrated in Figure 5.12 (b). Increasing the viscosity of the pumping fluid is an effective way to obtain the required width of the vertical fracture.

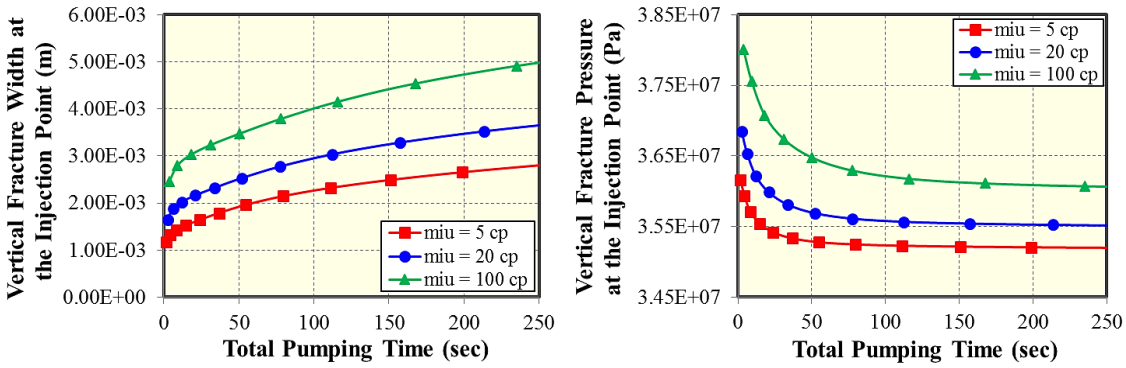

Figure 5.12: (a) Impact of fluid viscosity on the width of vertical fracture at the injection point; (b) Impact of fluid viscosity on the pressure of vertical fracture at the injection point.

Two sub-figures in Figure 5.13 indicate the impact of fluid viscosity on the width profile and pressure profile of the vertical fracture at the junction area, respectively. A positive correlation between the fluid viscosity and the vertical fracture width at the junction area, is very obvious in Figure 5.13 (a). At the junction area, the pressure profile of the vertical fracture (Figure 5.13 (b)) also has a positive correlation with the fluid viscosity. Figure 5.14 (a) shows the width profile of the bedding plane under the influence of the fluid viscosity, when the vertical fracture is arrested by the symmetric bedding planes. With smaller fluid viscosity, it takes less time for the vertical fracture to be arrested by the bedding planes, which means that the fracture propagates faster in the vertical direction. From Figures 5.14 (a) and 5.14 (b), we observed that both width and pressure of the bedding plane at the junction area, have a positive relation with the fluid viscosity. Greater prominence of the effect of the shear sliding (shear displacement discontinuities profile in Figure 5.15 (b)) along the bedding plane than that of tensile opening (width profile of the bedding plane in Figure 5.15 (a)), is illustrated in Figure 5.15. Both the

opening of the interface and the shear displacement discontinuities along the bedding plane drop very quickly when the lateral location along the bedding plane is far away from the junction area. Moreover, the opening and the shear displacement discontinuities of the bedding plane are both positively correlated with the fluid viscosity.

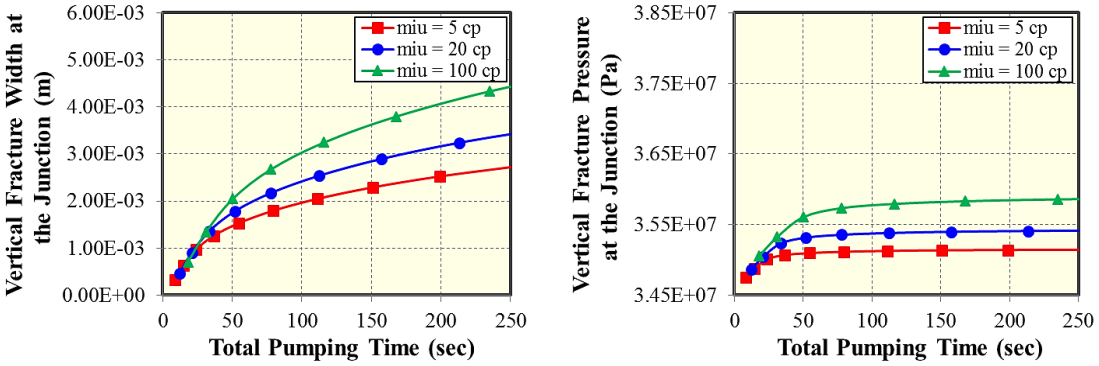

Figure 5.13: (a) Impact of fluid viscosity on the width of vertical fracture at the junction area; (b) Impact of fluid viscosity on the pressure of vertical fracture at the junction area.

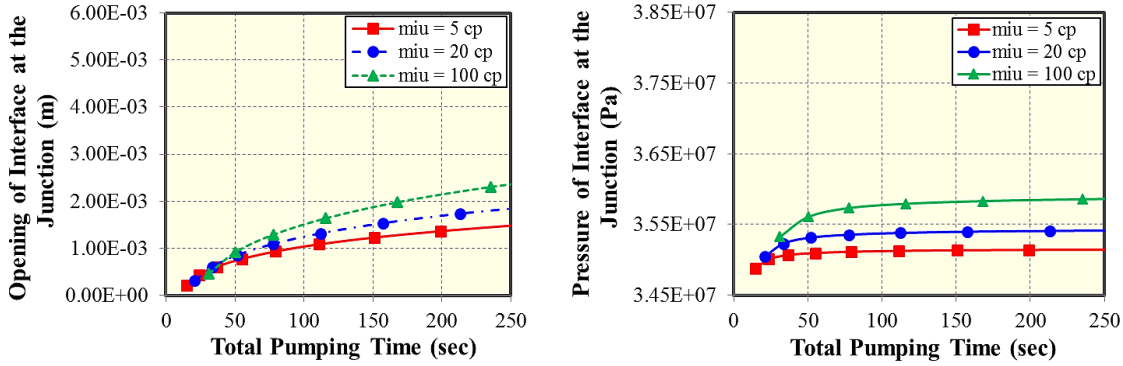

Figure 5.14: (a) Impact of fluid viscosity on the opening of bedding plane at the junction area; (b) Impact of fluid viscosity on the pressure of bedding plane at the junction area.

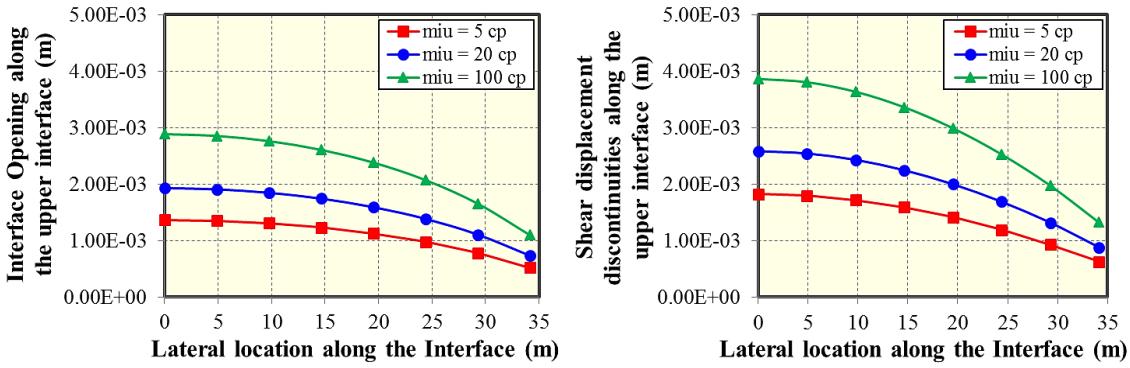

Figure 5.15: (a) Impact of fluid viscosity on the interface opening along the upper bedding plane at the end of injection treatment; (b) Impact of fluid viscosity on the shear displacement discontinuities along the upper bedding plane at the end of injection treatment.

5.3.3 Young's Modulus

The formation properties such as Young's modulus (YM) and Poisson's ratio, also play an important role in determining the fracture height growth and the fracture width profile. In this subsection, we discussed the impact of different Young's modulus (1×10^6 psi, 3×10^6 psi, 6×10^6 psi) on the width and pressure profiles of the vertical fracture at the injection source and at the junction area, those profiles of the bedding plane at the junction area, the opening of the interface and shear displacement discontinuities along the bedding plane at the end of the injection. Figures 5.16 (a) and 5.16 (b) indicate the impact of Young's modulus on the vertical fracture width and the impact of Young's modulus on the pressure of the vertical fracture, at the injection point, respectively. The vertical fracture width at the injection point has a negative correlation with Young's modulus. However, the pressure of the vertical fracture at the injection point is positively related with Young's modulus.

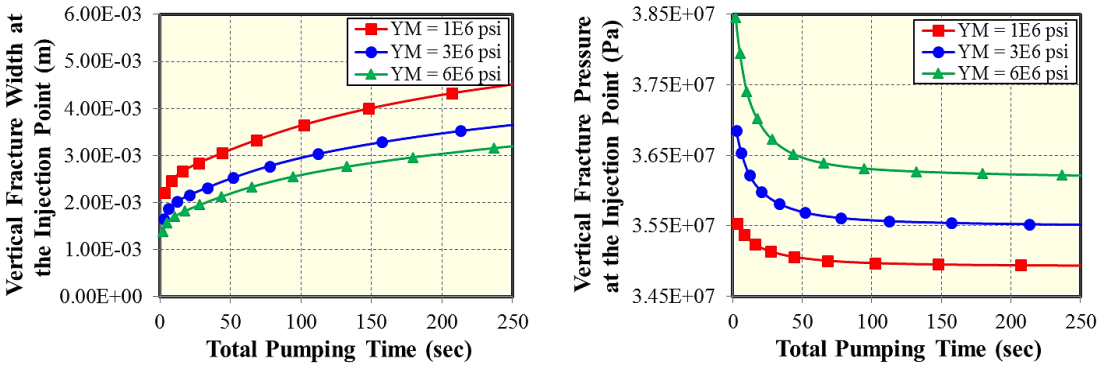

Figure 5.16: (a) Impact of Young's modulus on the width of vertical fracture at the injection point; (b) Impact of Young's modulus on the pressure of vertical fracture at the injection point.

Figure 5.17 (a) shows a negative correlation between the Young's modulus and the width of the vertical fracture at the junction area, after the vertical fracture contacts with two interface. Figure 5.17 (b) manifests that the pressure of the vertical fracture increases with the increment of the Young's modulus. Figure 5.17 also reveals that larger Young's modulus makes the vertical fracture earlier approaching the symmetric bedding planes.

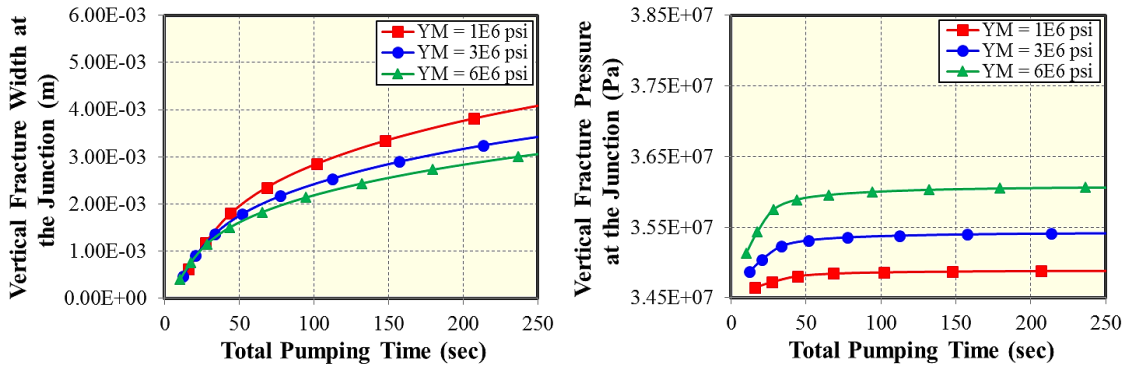

Figure 5.17: (a) Impact of Young's modulus on the width of vertical fracture at the junction area; (b) Impact of Young's modulus on the pressure of vertical fracture at the junction area.

Figure 5.18 (a) illustrates that a larger Young's modulus makes the opening of the bedding plane smaller at the junction area. The influence of Young's modulus is less on the opening of the bedding plane at the junction area, but it has more effect on the fluid pressure of the bedding plane at the junction area, as observed in Figure 5.18 (b). From Figures 5.17 and 5.18, we also found that the vertical fracture width is twice than the opening of the bedding plane at the junction area, when the vertical fracture is arrested by the bedding planes.

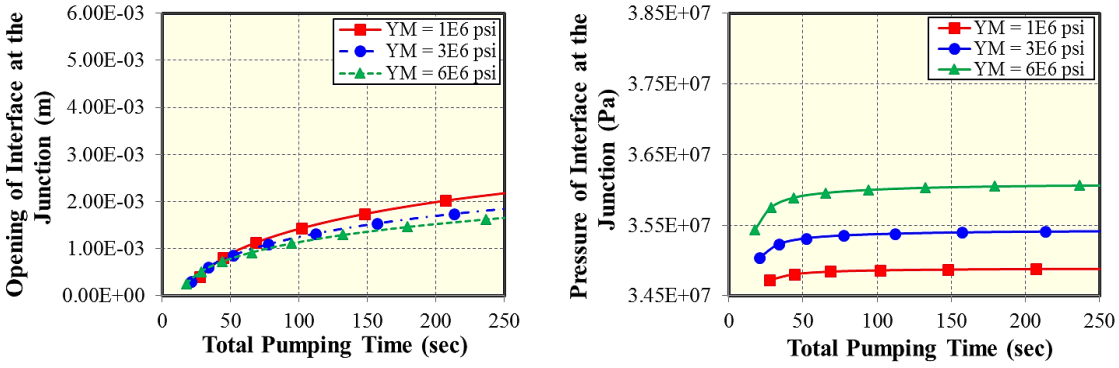

Figure 5.18: (a) Impact of Young's modulus on the opening of bedding plane at the junction area; (b) Impact of Young's modulus on the pressure of bedding plane at the junction area.

The impact of Young's modulus on the interface opening along the upper bedding plane at the end of injection, is described in Figure 5.19 (a). Figure 5.19 (b) elaborates that shear displacement discontinuities along the bedding planes are negatively related with the Young's modulus. Moreover, a higher Young's modulus in the formation can prevent the opening of the bedding plane and avoid more fluid percolated into the interface, and further reduce the fracture height containment.

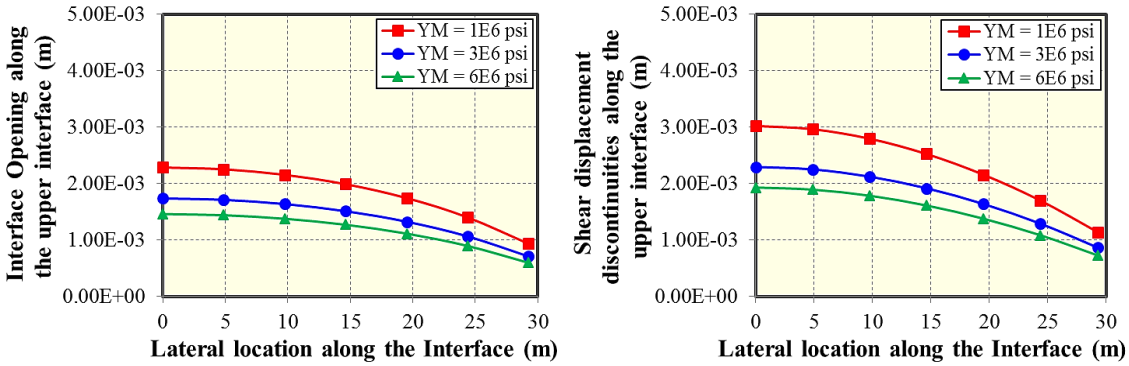

Figure 5.19: (a) Impact of Young's modulus on the interface opening along the upper bedding plane at the end of injection treatment; (b) Impact of Young's modulus on the shear displacement discontinuities along the upper bedding plane at the end of injection treatment.

5.4 Conclusion

This chapter introduces to investigate the mechanical interaction between hydraulic fractures and weak bedding planes in three dimensions and the physical mechanism of shear sliding along the bedding planes using a coupled hydraulic fracture propagation model. The investigation enables the following conclusions:

(1) Without considering layering, our fracture propagation model reproduces half-length, pressure, and width profiles at the injection point for the PKN model, thereby verifying it reproduces established model characteristics;

(2) During the period of injection, when bedding planes arrest growth of a vertical fracture, they open at the junction area and fluid percolates into the planes and creates shear displacement discontinuities along the planes. Both the width of the vertical fracture and shear displacement discontinuities along the bedding planes are far greater

than the opening of the bedding planes at the junction area, and this differential provides insight for selecting the proppant grain size range;

(3) Increased fluid injection rate into the formation slightly widens the opening of bedding planes at the junction area, but shear displacement discontinuities along the planes are a more obvious effect from rate variation. Moreover, our model enables assessment of the pumping rate required to obtain the required fracture width at both junctions and intersected bedding planes, which makes them sufficient for proppant transport;

(4) With lower fluid viscosity, a vertical fracture propagates faster and height growth is more easily arrested by the bedding planes. However, increasing the fluid viscosity is an effective way to obtain the large width of the vertical fracture. Hence, the fluid viscosity poses a trade-off between fracture height containment and width growth;

(5) Higher formation Young's modulus can prevent the opening of a bedding plane and reduce the fluid percolation into the interface, thus impairing the fracture height containment.

6. CONCLUSIONS AND FUTURE WORK

In this chapter, my primary research work in the dissertation were summarized. The new three-dimensional fracture propagation model considering the effect of bedding planes were developed. Thereafter, my future work were introduced with related references.

6.1 Conclusions

In this dissertation, I proposed a three-dimensional displacement discontinuity method (3D DDM) which can deal with cases of multiple fractures with arbitrary angles in three dimensions. A good match of fracture width and induced stresses between a 2D analytical solution and 3D DDM was obtained for a single fracture. Analysis of different fracture geometry and sensitivity analysis of different controlling parameters have been done to investigate the effects of the opening of the weak bedding plane and physical mechanism of slippage along the bedding plane, which provides a critical insights of fracture width distribution and their impacts on proppant transport. Then a three-dimensional hydraulic fracture propagation model was developed, which couples with rock deformation and fluid flow and also considers the effect of the bedding layers. In this model, the rock deformation part is governed by 3D DDM. The fluid flow part, governed by finite difference method, considers the flow along both the fracture length and height directions and is coupled with the rock deformation part via Picard iterative algorithm.

Comparison between the developed model and the PKN model showed a good agreement. From the dissertation, conclusions can be made as,

(1) Vertical fracture width is altered by the opening of a weak bedding plane and a width jump is created along the vertical fracture when the vertical fracture penetrates the bedding plane. This width jump, regarded as a primary mechanism of fracture height containment, is induced by the shear sliding along the bedding plane and positively correlated with the distance between the wellbore location and the horizontal interface. This mechanism not only indicates that the vertical fracture is easier to be arrested as the well location is far away from the bedding plane, but also helps us select an optimal landing location of the horizontal wellbore;

(2) Both widths of fracture segments and shear sliding along the bedding plane have positive correlation with the dimension of the bedding plane segment, the distance between the injection source and the bedding plane segment, the net pressure within the fracture segments. Conversely, higher formation Young's modulus can prevent the opening of a bedding plane and reduce the fluid percolation into the bedding plane segment, thus impairing the fracture height containment;

(3) The case of multiple fractures with the bedding plane has smaller fracture width compared with the case without the bedding plane, as a result of energy dissipation for shear sliding along the bedding plane. Moreover, fracture spacing significantly determines the fracture width distribution and shear displacements along the bedding plane. Both the openings of the vertical fracture and bedding plane segment has a positive correlation with the fracture spacing;

(4) It is more difficult for the opening of the bedding plane segment when the vertical fracture approaches the bedding plane with a non-orthogonal angle. Both the opening of the bedding plane segment and the shear displacement discontinuity along the plane have a positive relation with the approach angle. Elevating the bedding plane from the injection source has an unconspicuous impact on the opening of the bedding plane and shear sliding along the plane, when the approach angle is non-orthogonal;

(5) During the period of injection, both the vertical fracture width and shear displacement discontinuities along the bedding plane are far greater than the opening of the bedding plane at the junction area, when the vertical fracture is arrested by the bedding plane. Increasing the fluid viscosity is an effective way to obtain the large width of the vertical fracture. In addition, the increment of the pumping rate slightly widens the opening of the bedding plane but more obviously alters the shear displacement discontinuities along the plane. Our model enables to provide a critical insight for the selection of the proppant grain size range and assessment of the required pumping rate to obtain the required width at both junction and intersected bedding plane.

6.2 Future Work

Currently our 3D fracture propagation model can only simulate one vertical fracture interacts with multiple bedding planes. The case of multiple fractures would be added to the fracture propagation model in the future. In the rock deformation section, the maximum-circumferential-stress criterion would be implemented to calculate the stress intensity factors for both the opening mode and shear sliding mode, which are then utilized

to determine the fracture propagation direction. In the fluid flow section, we would consider the volume conservation and the pressure continuity by setting restrictions, such as hydrostatic-pressure change, perforation frictional pressure drop and frictional pressure loss in each casing interval (Wu and Olson 2015). Kirchoff's first and second laws would be applied to determine the flow rate distribution in multiple fractures (Siriwardane and Layne 1991; Mack et al. 1992; Elbel et al. 1992). Moreover, the internal and boundary heat sources would be added to our model so as to simulate the temperature distribution and induced thermal stresses (Shen et al. 2012). Microseismic mapping would be implemented to characterize the fracture complexity, which further evaluates the completion performance and modifies the design parameters of hydraulic fracture treatment (Cipolla et al. 2011).

REFERENCES

Abass, H. H., S. Hedayati and D. L. Meadows. 1996. Nonplanar Fracture Propagation from a Horizontal Wellbore: Experimental Study. *SPE Prod and Fac.*, 133-137.

Abbas, S., Gordeliy, E., Peirce, A., Lecampion, B., Chuprakov, D.A., and Prioul, R. 2014. Limited Height Growth and Reduced Opening of Hydraulic Fractures due to Fracture Offsets: an XFEM Application. Paper SPE 168622 presented at the SPE Hydraulic Fracturing Technology Conference, Woodlands, Texas, USA, 4–6 February.

Abou-Sayed, A. S., Sinha, K. P. and Clifton, R.J. 1984. Evaluation of the Influence of In-situ Reservoir Conditions on the Geometry of Hydraulic Fractures Using a 3-D Simulator: Part I: technical approach. SPE 12877, presented at SPE/DOE/GRI Unconventional Gas Recovery Symp. Pittsburgh, PA, May 13-15.

Adachi J, Siebrits E, Peirce A, Desroches J. Computer Simulation of Hydraulic Fractures. *International Journal of Rock Mechanics and Mining Sciences and Geomechanics Abstracts* 2007; 44:739–757.

Adachi, J. I., E. Detournay, and A. P. Peirce (2010). Analysis of the Classical Pseudo-3D Model for Hydraulic Fracture with Equilibrium Height Growth across Stress Barriers. *International Journal of Rock Mechanics and Mining Sciences* 47(4): 625-639.

Barree, R.D., 1983. A Practical Numerical Simulator for Three-dimensional Fracture Propagation in Heterogeneous Media. In: SPE 12273, SPE Symposium Reservoir Simulation, San Francisco, California, USA, 15–18 November.

Blanton, T.L. 1982. An Experimental Study of Interaction between Hydraulically Induced and Pre-Existing Fractures. In *Proceedings of the SPE/DOE Unconventional Gas Recovery Symposium, Pittsburgh, PA, 16–18 May 1982,* SPE/DOE 10847.

Blanton, T. L. 1986. Propagation of Hydraulically and Dynamically Induced Fractures in Naturally Fractured Reservoirs. SPE 15261, presented at the Unconventional Gas Technology Symposium of the Society of Petroleum Engineering, Louisville, KY, May 18-21.

Bao, J., Fathi, E., Ameri, S. A Coupled Finite Element Method for the Numerical Simulation of Hydraulic Fracturing with a Condensation Technique. *Eng Fract Mech*, 131 (2) (2014), pp. 269-281.

Bunger, A.P., Kear, J., Jeffrey, R.G., Prioul, R., and Chuprakov, D. 2015. Laboratory Investigation of Hydraulic Fracture Growth through Weak Discontinuities with Active Ultrasound Monitoring. Presented at the 13th ISRM International Congress of Rock Mechanics, Montreal, Quebec, Canada, 10-13 May.

Calhoun, D., and LeVeque R.J. A Cartesian Grid Finite-volume Method for the Advection-diffusion Equation in Irregular Geometries, J. *Comput. Phys*. 2000; 157:143–80.

Carter BJ, Desroches J, Ingraffea AR, Wawrzynek PA. Simulating Fully 3D Hydraulic Fracturing. In: Zaman M, Booker J, Gioda G, editors. Modeling in geomechanics. New York: Wiley Publishers, 2000.

Chen, Z., 2012. Finite Element Modeling of Viscosity-dominated Hydraulic Fractures. *J. Pet. Sci. Eng.* 88–89, 136–144.

Chuprakov, D. (2015). Hydraulic Fracture Height Growth Limited by Interfacial Leakoff. *Hydraulic Fracturing Journal.*

Chuprakov, D., Melchaeva, O., Prioul, R., 2013. Injection-sensitive Mechanics of Hydraulic Fracture Interaction with Discontinuities. In ARMA 47th US Rocks Mechanics/Geomechanics Symposium, San Francisco, California, USA, 23–26 June.

Chuprakov, D. and Prioul, R. 2015. Hydraulic Fracture Height Containment by Weak Horizontal Interfaces. Paper SPE 173337 presented at the SPE Hydraulic Fracturing Technology Conference, Woodlands, Texas, USA, 3–5 February.

Cipolla, C., Weng, X., Mack, M., Ganguly, U., Gu, H., Kresse, O., Cohen, C., and Wu, R. 2011. Integrating Microseismic Mapping and Complex Fracture Modeling to Characterize Fracture Complexity. Paper 140185 presented at the SPE Hydraulic Fracturing Technology Conference and Exhibition held in the Woodlands, Texas, USA, 24-26 January.

Clifton, R.J., Abou-Sayed, A.S., 1981. A Variational Approach to the Prediction of the Three-dimensional Geometry of Hydraulic Fractures. In: Paper SPE 9879, SPE/DOE Low Permeability Gas Reservoirs Symposium, Denver, Colorado, 27–29 May.

Clifton, R.J., Wang, J.J., 1991. Adaptive Optimal Mesh Generator for Hydraulic Fracturing. In: J.C. Roegiers (Ed.), Rock Mechanics as a Multidisciplinary Science, Rotterdam: Balkema, pp. 607–616.

Cohen, C., Kresse, O., and Weng, X. 2017. Stacked Height Model to Improve Fracture Height Growth Prediction, and Simulate Interactions with Multi-Layer DFNs and

Ledges at Weak Zone Interfaces. Presented at the SPE Hydraulic Fracturing Technology Conference. The Woodlands, Texas, USA, 24–26 January.

Cooke, M. L., and C. A. Underwood, 2001, Fracture Termination and Step-over at Bedding Interfaces due to Frictional Slip and Interface Opening: *Journal of Structural Geology*, v. 23, p. 223-238.

Crittendon BC. The Mechanics of Design and Interpretation of Hydraulic Fracture Treatments. *J Pet Tech* 1959; (October):21–9.

Crouch, S. L. 1976. Solution of Plane Elasticity Problems by the Displacement Discontinuity Method. *International Journal for Numerical Methods in Engineering* 10(2): 301-343.

Crouch, S. L. and Starfield, A. M. 1983. Boundary Element Methods in Solid Mechanics. London: George Allen & Unwin.

Cui, J., & Zhu, D. (2014, January 19). Diagnosis of Multiple Fracture Stimulation in Horizontal Wells by Downhole Temperature Measurements. International Petroleum Technology Conference. doi:10.2523/IPTC-17700-MS.

Cui, J., Zhu, D., & Jin, M. (2016, November 1). Diagnosis of Production Performance after Multistage Fracture Stimulation in Horizontal Wells by Downhole Temperature Measurements. Society of Petroleum Engineers. doi:10.2118/170874-PA.

Currie, I.G., 1974, *Fundamental mechanics of Fluids*, McGraw-Hill, New York.

Dahi-Taleghani, A., Olson, J.E., 2011. Numerical Modeling of Multi-strand Hydraulic Fracture Propagation: Accounting for the Interaction between Induced and Natural Fractures. *SPE J.* 16 (3), 575–581, SPE 124884-PA.

Dean, R.H., Schmidt, J.H., 2008. Hydraulic Fracture Predictions with a Fully Coupled Geomechanical Reservoir Simulator. In: Paper SPE 116470, SPE Annual Technical Conference and Exhibition, Denver, Colorado, USA, 21–24 September.

Dhatt, G. and Touzat G., 1984. The Finite Element Method Displayed, Wiley, New York.

Elbel, J.L., Piggott, A.R., and Mack, M.G. 1992. Numerical Modeling of Multilayer Fracture Treatments. Presented at the SPE Permian Basin Oil and Gas Recovery Conference, Midland, Texas, 18-20 March. SPE-23982-MS.

Fan T, Zhang G, Cui J. The impact of cleats on hydraulic fracture initiation and propagation in coal seams [J]. Petroleum Science, 2014, 11(4):215-229.

Fan T G, Zhang G Q. Laboratory investigation of hydraulic fracture networks in formations with continuous orthogonal fractures [J]. Energy, 2014, 74(2):164-173.

Fisher, M.K., Wright, C.A., Davidson, B.M., Goodwin, A.K., Fielder, E.O., Buckler, W.S., Steinberger, N.P., 2002. Integrating Fracture Mapping Technologies to Optimize Stimulations in the Barnett shale. In: Paper SPE 77411, SPE Annual Technical Conference and Exhibition, San Antonio, Texas, USA, 29 September – 2 October.

Fisher, M.K. and Warpinski N.R. 2012. Hydraulic Fracture-Height Growth: Real Data. *SPE Prod. Oper*. 27, 8.

Fu, P., Johnson, S.M., Carrigan, C.R., 2011. Simulating Complex Fracture Systems in Geothermal Reservoirs Using an Explicitly Coupled Hydro-mechanical Model. In: Paper ARMA 11–244, 45th US Rock Mechanics Symposium, San Francisco, California, 26–29 June.

Fung, R. L., Vilajakumar S., Cormack D. E. 1987. Calculation of Vertical Fracture Containment in Layered Formations. SPE 14707-PA. *SPE Formation Eval* 2(4): 518-23.

Geertsma J, de Klerk F. A Rapid Method of Predicting Width and Extent of Hydraulically Induced Fractures. *J Pet Tech* 1969; 21:1571–81 [SPE 2458].

Green AE, Sneddon IN. The Distribution of Stress in the Neighbourhood of a Flat Elliptical Crack in an Elastic Solid. Proc Cambridge Philos Soc 1950; 46:159–63.

"GSA Critical Issue: Hydraulic Fracturing." *Geological Society of America*. 10 Dec. 2014. http://www.geosociety.org/criticalissues/hydraulicFracturing/defined.asp&gt.

Gu, H., 1987. A Study of Propagation of Hydraulically Induced Fractures (Ph.D. dissertation), Department of Engineering Mechanics, The University of Texas at Austin, Austin, TX.

Gu, H., Yew, C.H., 1988. Finite Element Solution of a Boundary Integral Equation for Mode I Embedded Three-dimensional Fractures. Int. J. Num. Meth. Eng. 26, 1525–1540.

Gu, H. and Siebrits, E. 2008. Effect of Formation Modulus Contrast on Hydraulic Fracture Height Containment. *SPE Prod & Oper* 23 (02): 170-176.

Gu, H., Siebrits, E., and Sabourov, A. 2008. Hydraulic-Fracture Modeling with Bedding Plane Interfacial Slip. Paper SPE 117445 presented at the SPE Eastern Regional/AAPG Eastern Section Joint Meeting, Pittsburgh, Pennsylvania, USA, 11–15 October.

Gu, H. and Weng, X. 2010. Criterion For Fractures Crossing Frictional Interfaces At Non-orthogonal Angles. Paper ARMA 10-198 presented at the 44th U.S. Rock Mechanics Symposium and 5th U.S.-Canada Rock Mechanics Symposium, Salt Lake City, Utah, USA, 27-30 June.

Gu, H. Weng, X. Lund, J., Mack, M., Ganguly, U., Suarez-Rivera, R. 2011. Hydraulic Fracture crossing Natural Fracture at Non-orthogonal Angles, a Criterion, its Validation and Applications. SPE 139984, presented at the SPE Hydraulic Fracturing Technology Conference and Exhibition, The Woodlands, Texas, USA, 24-26 January.

Guo, X., Wu, K., and Killough, J., 2018. Investigation of Production-Induced Stress Changes for Infill Well Stimulation in Eagle Ford Shale. *SPE Journal*. SPE-189974-PA. https://doi.org/10.2118/189974-PA.

Huang, J., Yang, C., Xue, X., & Datta-Gupta, A. 2016. Simulation of Coupled Fracture Propagation and Well Performance under Different Refracturing Designs in Shale Reservoirs. Society of Petroleum Engineers. doi:10.2118/180238-MS.

Hubbert MK, Willis DG. Mechanics of Hydraulic Fracturing. *J Pet Tech* 1957; 9(6): 153-68.

Izadi, G., Moos, D., Cruz, L., Chiaramonte, L., and Johnson, S. 2017. Fully Coupled 3-D Hydraulic Fracture Growth in the Presence of Weak Horizontal Interfaces. Presented at the SPE Hydraulic Fracturing Technology Conference. The Woodlands, Texas, USA, 24–26 January.

Ji, L., Settari, A., Sullivan, R.B., 2009. A Novel Hydraulic Fracturing Model Fully Coupled with Geomechanics and Reservoir Simulation. *SPE J.* (September), 423–430.

Jing, L., Ma, Y., Fang, Z., 2001. Modeling of Fluid Flow and Solid Deformation for Fractured Rocks with Discontinuous Deformation Analysis (DDA) method. *Int. J. Rock. Mech. Min. Sci.* 38, 343–355.

Khristianovich S.A., Zheltov Y.P. Formation of Vertical Fractures by Means of Highly Viscous Liquid, Proc., Fourth World Pet. Congress, Rome (1955) 2, 579–586.

Kresse, O., Weng, X., Chuprakov, D., Prioul R., Cohen, C., 2013. Effect of Flow Rate and Viscosity on Complex Fracture Development in UFM Model. In: International Conference for Effective and Sustainable Hydraulic Fracturing, Brisbane, Australia, 20–22 May.

Kumar, D., Ghassemi, A., 3D simulation of multiple fracture propagation from horizontal wells, in: Proceedings 49th U.S. Rock Mechanics Symposium, San Francisco, CA, USA, ARMA-2015-585, American Rock Mechanics Association, 2015.

Kumar, D., Ghassemi, A., 2016. 3D proroelastic simulation and analysis of multiple fracture propagation and refracturing of closely-spaced horizontal wells. In: The 50th US Rock Mechanics/Geomechanics Symposium, Houston, Texas.

Lee, H.P., Olson, J.E., and Schultz, R.A. The Interaction Analysis of Propagating Opening Mode Fractures with Veins Using Discrete Element Method. ARMA-2016-769. In Proceedings of the US Rock Mechanics/Geomechanics Symposium, Houston, Texas, USA, June 26 – 29, 2016.

Lee, H.P., Razavi, O., and Olson, J.E. Hydraulic Fracture Interaction with Cemented Natural Fracture: A Three Dimensional Discrete Element Method Analysis. Presented

at the SPE Hydraulic Fracturing Technology Conference. The Woodlands, Texas, USA, 23–25 January 2018. SPE-189852-MS.

Lepotter, 2014. Hydraulic Fracturing: What the media doesn't say.

LeVeque, R.J., 2007. Finite Difference Methods for Ordinary and Partial Differential Equations: Steady-State and Time-Dependent Problems, Society of Industrial and Applied Mathematics, Philadelphia.

Li, J., Yu, W., Wu, K. 2018. Analyzing the Impact of Fracture Complexity on Well Performance and Wettability Alteration in Eagle Ford shale. Presented at Unconventional Resources Technology Conference (URTeC) in Houston, Texas, USA, 23 July – 25 July.

Li, N., Zhang, S., Zou, Y., Ma, X, Wu, S., Zhang, Y. 2017. Experimental analysis of hydraulic fracture growth and acoustic emission response in a layered formation. Rock Mechanics and Rock Engineering 51(4): 1047-1062.

Li, Y., Rui, Z., Zhao, W., Bo, Y., Fu, C., Chen G., Patil, S. 2018a. Study on the Mechanism of Rupture and Propagation of T-type Fractures in Coal Fracturing. Journal of Natural gas science and engineering. Vol. 52: 379-389.

Li, Y., Jia, D., Li, W., Zhang, K. 2018b. Model of T-Type Fracture in Coal Fracturing and Analysis of Influence Factors of Fracture Morphology. Energies. Vol. 11(5): 1196.

Liu, G. and Ehlig-Economides, C. 2015. Comprehensive Global Model for before-Closure Analysis of an Injection Falloff Fracture Calibration Test. Paper presented at the SPE Annual Technical Conference and Exhibition, Houston, Texas, USA. Society of Petroleum Engineers. DOI: 10.2118/174906-MS.

Liu, G. and Ehlig-Economides, C. 2016. Interpretation Methodology for Fracture Calibration Test before-Closure Analysis of Normal and Abnormal Leakoff Mechanisms. Paper presented at the SPE Hydraulic Fracturing Technology Conference, The Woodlands, Texas, USA. Society of Petroleum Engineers. DOI: 10.2118/179176-MS.

Ehlig-Economides, C.A. and Liu, G. 2017. Comparison among Fracture Calibration Test Analysis Models. Paper presented at the SPE Hydraulic Fracturing Technology Conference and Exhibition, The Woodlands, Texas, USA. Society of Petroleum Engineers. DOI: 10.2118/184866-MS.

Liu, S. and Valko, P.P. 2015. An Improved Equilibrium-Height Model for Predicting Hydraulic Fracture Height Migration in Multi-Layered Formations. Presented at the SPE Hydraulic Fracturing Technology Conference. The Woodlands, Texas, USA, 3–5 February.

Llanos, E.M., Jeffrey, R.G., Hillis, R. et al., Hydraulic Fracture Propagation through an Orthogonal Discontinuity: A Laboratory, Analytical and Numerical Study. *Rock Mech Rock Eng* (2017) 50: 2101. https://doi.org/10.1007/s00603-017-1213-3.

LUKOIL, 2013. Global Trends in Oil and Gas Markets to 2025.

Khristianovic SA, Zheltov YP. Formation of Vertical Fractures by Means of Highly Viscous Liquid. In: Proceedings of the fourth world petroleum congress, Rome, 1955. p. 579–86.

Ma XF, Li N, Yin CB, Li YC, Zou YS, Wu S, He F, Wang XQ, Zhou T (2017) Hydraulic fracture propagation geometry and acoustic emission interpretation: A case study of

Silurian Longmaxi Formation shale in Sichuan Basin, China. Petroleum Exploration & Development 44(6): 1030 – 1037.

Mack, M.G, Elbel, Jacques L., and Piggott, Andrew R. 1992. Numerical Representation of Multilayer Fracturing. Rock Mechanics, ed. Tillerson and Wawersik. Balkema, Rotterdam. ISBN 90 5410 0451.

Mack, M.G, Warpinski, R. Mechanics of Hydraulic Fracturing. In: Economides MJ, Nolte KG, editors. Reservoir stimulation, 3rd ed.. Chichester, UK: John Wiley & Sons; 2000. [Chapter 6].

Maxwell, S.C., Urbancic, T.I., Steinsberger, N.P., Zinno, R., 2002. Microseismic Imaging of Hydraulic Fracture Complexity in the Barnett Shale. In: Paper SPE 77440, SPE Annual Technical Conference and Exhibition, San Antonio, Texas, 29 September – 2 October.

McClure, M. W. 2012. Modeling and Characterization of Hydraulic Stimulation and Induced Seismicity in Geothermal and Shale Gas Reservoirs. Ph.D. Dissertation. Stanford University.

Meyer BR. Design Formulae for 2d and 3-d Vertical Hydraulic Fractures: Model Comparison and Parametric Studies. In Proceedings of the unconventional gas technology symposium, SPE 15240, 1986. p. 391–408.

Meyer, B.R., Bazan, L.W. 2011. A Discrete Fracture Network Model for Hydraulically Induced Fractures: Theory, Parametric and Case Studies. In: Paper SPE 140514, SPE Hydraulic Fracturing Conference and Exhibition, Woodlands, Texas, USA, 24–25 January.

Miskimins, J.L., and R.D. Barree, 2003. Modeling of Hydraulic Fracture Height Containment in Laminated Sand and Shale Sequences. In SPE Production and Operations Symposium, Oklahoma City, Oklahoma, USA, 22–25 March.

Nagel, N.B., Gil, I., Sanchez-Nagel, M., Damjanac, B., 2011. Simulating hydraulic fracturing in real fractured rock – overcoming the limits of pseudo 3D models. In: Paper SPE 140480, SPE Hydraulic Fracturing Conference and Exhibition, Woodlands, Texas, 24–26 January.

Nintcheu Fata, S. 2016. Coupling Elasticity and Fluid Flow for A 3D Hydraulic Fracturing Solver. Presented at the 50th US Rock Mechanics / Geomechanics Symposium held in Houston, Texas, USA, 26-29 June.

Nordren R.P. Propagation of a Vertical Hydraulic Fracture. *SPE J* 1972; 12(8):306–14 [SPE 7834].

IlScams.org. Oil Shale vs. Shale Oil vs. Shale Gas. http://www.oilscams.org/oil-shale-shale-oil-shale-gas.

Olson, J. E. 1995. Fracturing from Highly Deviated and Horizontal Wells: Numerical Analysis of Non-planar Fracture Propagation. SPE 29573, presented at SPE Rocky Mountain Regional/Low-Permeability Reservoirs Symposium, Denver, Colorado, March 20-22.

Olson, J. E. 2004. Predicting Fracture Swarms - The Influence of Subcritical Crack Growth and the Crack-tip Process Zone on Joint Spacing in Rock. Geological society, London, Special Publications 231(1): 73-88.

Olson, J. E. 2008. Multi-fracture Propagation Modeling: Application to Hydraulic Fracturing in Shales and Tight Gas Sands. ARMA 08-327 presented at the 42nd US Rock Mechanics Symposum and 2nd U.S.-Canada Rock Mechanics Symposium, held in San Francisco, June 29-July 2.

Olson, J. E., and Dahi-Taleghani, A. 2009. Modeling Simultaneous Growth of Multiple Hydraulic Fractures and Their Interaction with Natural Fractures. SPE 119739, presented at SPE Hydraulic Fracturing Technology Conference, The Woodlands, Texas, USA, 19–21 January.

Palmer, I.D. and Carroll, Jr., H.B. 1983. Three-Dimensional Hydraulic Fracture Propagation in the Presence of Stress Variations. *SPE J.* 23 (6): 870-878.

Palmer, I.D. and Carroll, Jr., H.B. Numerical Solution for Height and Elongated Hydraulic Fractures. In: Proceedings of the SPE/DOE low permeability reservoir symposium, Denver. SPE 11627, Society of Petroleum Engineers, 1983. p. 249–6.

Palmer, I.D and Craig, H.R. Modeling of Asymmetric Vertical Growth in Elongated Hydraulic Fractures and Application to First MWX Stimulation. In: Proceedings of the SPE/DOE/GRI unconventional gas recovery symposium, SPE 12879, 1984. p. 453–62.

Peirce, A.P., Siebrits, E., 2001. The Scaled Flexibility Matrix Method for the Efficient Solution of Boundary Value Problems in 2D and 3D Layered Elastic Media. *Comput. Methods Appl. Mech. Eng.* 190 (45), 5935–5956.

Perkins T.K., Kern L.R. Widths of Hydraulic Fractures. *J Pet Tech* 1961; 13(9):937–49 [SPE 89].

Renshaw, C.E., Pollard, D.D., 1995. An Experimentally Verified Criterion for Propagation across Unbounded Frictional Interfaces in Brittle, Linear Elastic-materials. *Int. J. Rock Mech. Min. Sci. Geomech. Abstr*. 32 (3), 237–249.

Riahi, A., Damjanac, B., 2013. Numerical study of interaction between hydraulic fracture and discrete fracture network. In: International Conference for Effective and Sustainable Hydraulic Fracturing, Brisbane, Australia, 20–22 May.

Rongved, L. 1957. Dislocation over A Bounded Plane Area in An Infinite Solid. *J. Appl. Mech.* 24: 252-254.

Rungamornrat, J., Wheeler, M. F., Mear, M. E. 2005. A Numerical Technique for Simulating Nonplanar Evolution of Hydraulic Fracture. SPE 96968, presentation at the 2005 SPE Annual Technical Conference and Exhibition, Dallas, Texas, U.S.A., 9-12 October.

Rutledge, J., Weng, X., Chapman, C., Yu, X., and Leaney, S. 2016. Bedding-plane Slip as A Microseismic Source during Hydraulic Fracturing. Presented at the SEG International Exposition and 86th Annual Meeting.

Salamon, M. D. G. 1964. Elastic Analysis of Displacements and Stresses Induced Mining of Seam or Roof Deposits, Part IV. J. S. Afr. Inst. Min. Metall. 65: 319-338.

Sangnimnuan, A., Li, J., Wu, K. (2017). Development of Efficiently Coupled Fluid Flow and Geomechanics Model to predict Stress Evolution in Unconventional Reservoirs with Complex Fracture Geometry. *SPE Journal,* SPE-189452-PA.

Sarmadivaleh, M. and V. Rasouli. 2013. Modified Reinshaw and Pollard Criteria for a Non-Orthogonal Cohesive Natural Interface Intersected by an Induced Fracture. *Rock Mechanics and Rock Engineering*: p. 1–9.

Settari A, Cleary MP. Development and Testing of a Pseudo-three-dimensional Model of Hydraulic Fracture Geometry (p3dh). In: Proceedings of the 6th SPE symposium on reservoir simulation of the Society of Petroleum Engineers, SPE 10505, January–February 1982. p. 185–214.

Settari A, Cleary MP. Development and Testing of a Pseudo-three-dimensional Model of Hydraulic Fracture Geometry. *SPE Production Engineering*, November 1986. p. 449–66.

Shen, B., Guo, H., Ko, T. Y., Lee, S. C., Kim, J., Kim, H. M., Stephansson, O (2013). Coupling rock fracture propagation with thermal and fluid flow processes. International Journal of Geomechanics, 13, 794– 808.

Shen, B., Siren, T. and Rinne M. 2015. Modeling Fracture Propagation in Anisotropic Rock Mass. *Rock Mech. Rock Eng*., 48(3), 1067-1081.

Shi, G., 1988. Discontinuous Deformation Analysis: A New Numerical Model for the Static and Dynamics of Block System (Ph.D. theses), University of California, Berkeley.

Shin, D. H., Sharma, M. M. 2014. Factors Controlling the Simultaneous Propagation of Multiple Competing Fractures in a Horizontal Well. SPE 168599 presented at the SPE Hydraulic Fracture Technology Conference held in The Woodlands, Texas, USA, 4-6 February.

Shou, K. J. 1993. A High Order Three-dimensional Displacement Discontinuity Method with Application to Bonded Half-space Problems. *Ph.D. Dissertation*. University of Minnesota.

Shou, K. J., Siebrits, E., Crouch, S. L. A higher order displacement discontinuity method for three-dimensional elastostatics problems. *Int. J. Rock. Min. Sci. & Geomech. Abstr.,* 34 (2) (1997), pp. 317-322.

Siebrits, E., Peirce, A.P., 2002. An Efficient Multi-layer Planar 3D Fracture Growth Algorithm Using a Fixed Mesh Approach. *Int. J. Numer. Meth. Eng*. 53, 691–717.

Simonson, E. R., A. S. Abou-Sayed, and R. J. Clifton.1978. Containment of Massive Hydraulic Fractures. *Society of Petroleum Engineers Journal*, 18(01), 27–32. SPE6089.

Singh, G., Pencheva, G., Kumar, T., Wick, T., Ganis, B., Wheeler, M.F., 2014. Impact of Accurate Fractured Reservoir Flow Modeling on Recovery Predictions. In: Paper SPE 168630, SPE Hydraulic Fracturing Technology Conference, The Woodlands, Texas, 4–6 February.

Siriwardane, H.J. and Layne, A.W. 1991. Improve Model for Predicting Multiple Hydraulic Fracture Propagation From a Horizontal Well. Presented at the SPE Eastern Regional Meeting, Lexington, Kentucky, 22–25 October. SPE-23448-MS.

Slatt, R.M., and Y. Abousleiman, 2011, Merging Sequence Stratigraphy and Geomechanics for Unconventional Gas Shales: The Leading Edge, v.30/3, p. 274-282.

Smith, I.M., Griffiths, D.V., 1998. Programming the Finite Element Method, third edition, Wiley, Hoboken, New Jersey.

Smith, M.B., Bale, A.B., Britt, L.K., Klein, H.H., Siebrits, E., and Dang, X. 2001. Layered Modulus Effects on Fracture Propagation, Proppant Placement, and Fracture Modeling. Paper SPE 71654 presented at the SPE Annual Technical Conference and Exhibition, New Orleans, 30 September–3 October.

Sneddon I.N. The Distribution of Stress in the Neighbourhood of a Crack in an Elastic Solid. Proc R Soc London A 1946; 187:229–60.

Sneddon, I. N. 1951. Fourier transforms. New York: McGraw-Hill.

Suarez-Rivera, R., Von Gonten, W.D., Graham, J., Ali, S., Degenhardt, J. and Jegadeesan, A. 2016. Optimizing Lateral Landing Depth for Improved Well Production. Presented at the SPE/AAPG/SEG Unconventional Resources Technology Conference, San Antonio, Texas, USA, 1-3 August.

Tang, J., Wu, K. 2018. A 3-D Model for Simulation of Weak Interface Slippage for Fracture Height Containment in Shale Reservoirs. *International Journal of Solids and Structures*. https://doi.org/10.1016/j.ijsolstr.2018.05.007.

Tang, J., Wu, K., Zeng, B., Huang, H., Hu, X., Guo, X., Zuo, L. 2017. Investigate Effects of Weak Bedding Interfaces on Fracture Geometry in Unconventional Reservoirs. *Journal of Petroleum Science and Engineering*. 165, 992-1009.

Teufel, L.W., and Clark, J.A. 1984. Hydraulic Fracture Propagation in Layered Rock: Experimental Studies of Fracture Containment. *SPE Journal*, 24(1), 19–32.

Thiercelin, M., Roegiers, J.C., Boone T.J., and Ingraffea, A.R. 1987. An Investigation of the Material Parameters that Govern the Behavior of Fractures Approaching Rock Interfaces. In 6th ISRM Congress, August 30 – September 3, 1987, Montreal, Canada. International Society for Rock Mechanics.

Valko, P. and Economides, M.J. 1995. *Hydraulic Fracture Mechanics*. New York: John Wiley & Sons.

Vandamme, L., J.H. Curran. A Three-dimensional Hydraulic Fracturing Simulator. *Int J Numer Meth Eng*, 28 (1989), pp. 909-927.

Van Eekelen, H.A.M. 1982. Hydraulic Fracture Geometry: Fracture Containment in Layered Formations. *SPE J.* 22 (3): 341-349.

Versteeg H.K. and Malalasekera W., 2007. An Introduction to Computational Fluid Dynamics, second edition, Pearson Education Limited, England.

Virgo, S., Abe, S., and Urai, J., 2013, Extension Fracture Propagation in Rock with Veins: Insight into the Crack-seal Process Using Discrete Element Method modelling: *Journal of Geophysical Research-Solid Earth*, v. 118, n. 10, p. 5236–5251.

Wang S., Li Y., Liu H., Jiang M. Hydraulic Fracture Propagation in Unconventional Reservoirs: The Role of Bedding Plane. SL: Structural Longevity, 8 (3) (2012), pp. 173-191.

Warpinski, N.R. and L. W. Teufel. 1987. Influence of Geologic Discontinuities on Hydraulic Fracture Propagation. *Journal of Petroleum Technology*, February, 209-219.

Warpinski, N.R., Lorenz, J.C., Branagan, P.T., Myal, F.R., Gall, B.L., 1993. Examination of a Cored Hydraulic Fracture in a Deep Gas Well. J. SPE Prod. Facil. (August), 150-164.

Weng, X., Kresse, O., Cohen, C., Wu, R., Gu, H., 2011. Modeling of Hydraulic Fracture Network Propagation in a Naturally Fractured Formation. In: Paper SPE 140253, SPE

Hydraulic Fracturing Conference and Exhibition, Woodlands, Texas, USA, 24–26 January.

Weng, X. Modeling of Complex Hydraulic Fractures in Naturally Fractured Formation. *J. Unconv. Oil Gas Resour*. 2015, 9, 114–135.

Wong, S. W., Xu, G., 2013. Interaction of Multiple Hydraulic Fractures in Horizontal Wells. SPE 163982, presented at SPE Middle East Unconventional Gas Conference and Exhibition, Muscat, Oman, January 2013.

Wu, K. and Olson J. E. 2013. Investigation of the Impact of Fracture Spacing and Fluid Properties for Interfering Simultaneously - or Sequentially - Generated Hydraulic Fractures. SPE 163821-PA. SPE Production & Operations 28(4): 427-436.

Wu, K. 2014. Numerical modeling of complex hydraulic fracture development in unconventional reservoirs. *Ph.D. Dissertation*. The University of Texas at Austin.

Wu, K. and Olson, J.E. 2015. Simultaneous Multifracture Treatments: Fully Coupled Fluid Flow and Fracture Mechanics for Horizontal Wells. *SPE J.* 20 (2): 337-346. SPE-167626-PA.

Wu, K. and Olson, J.E. 2015. Study of Multiple Fracture Interaction Based on An Efficient Three-Dimensional Displacement Discontinuity Method. Presented at the 49th US Rock Mechanics / Geomechanics Symposium held in San Francisco, CA, USA, 28 June- 1 July.

Wu, K., Sangnimnuan, A., Tang, J. 2016. Numerical Study of Flow Rate Distribution for Simultaneous Multiple Fracture Propagation in Horizontal Wells. In: The 50th US Rock Mechanics/Geomechanics Symposium, Houston, Texas. ARMA 16-38.

Xie, J., Huang, H., Ma, H., Zeng, B., Tang, J., Yu, W., Wu, K. Numerical Investigation of Effect of Natural Fractures on Hydraulic-fracture Propagation in Unconventional Reservoirs. *Journal of Natural Gas Science and Engineering* 54(2018), pp. 143-153.

Xing, P., Yoshioka, K., Adachi, J., and EI-Fayoumi, A. 2016. Experimental Study of Hydraulic Fracture Containment in Layered Reservoirs. Presented at the 50th US Rock Mechanics / Geomechanics Symposium. Houston, Texas, USA, 26–29 June.

Xu, W., Calvez, J.L., Thiercelin, M. 2009. Characterization of Hydraulically-induced Fracture Network Using Treatment and Microseismic Data in a Tight-gas Formation: A Geomechanical Approach. In: Paper SPE 125237, SPE Tight Gas Completions Conference, San Antonio, Texas, USA, 15–17 June.

Yamamoto, K., Tatsuo S. and Shunichi S. 2004. Multiple Fracture Propagation Model for a Three-dimensional Hydraulic Fracturing Simulator. *International Journal of geomechanics* ASCE 4(1): 46-57.

Yang, C., Xue, X., Huang, J., Datta-Gupta, A., & King, M. J. 2016. Rapid Refracturing Candidate Selection in Shale Reservoirs Using Drainage Volume and Instantaneous Recovery Ratio. Unconventional Resources Technology Conference. doi:10.15530/URTEC-2016-2459368.

Yu, W., Wu, K., Zuo, L., Tan, X., Weijermars, R. 2016. Physical Models for Inter-Well Interference in Shale Reservoirs: Relative Impacts of Fracture Hits and Matrix Permeability. Presented at the Unconventional Resources Technology Conference, San Antonio, Texas, USA, 1-3 August, 2016. URTeC: 2457663.

Zhang, G., Fan, T. A high-stress tri-axial cell with pore pressure for measuring rock properties and simulating hydraulic fracturing [J]. Measurement, 2014, 49(49):236-245.

Zhang, X., Jeffrey, R.G., 2006. The Role of Friction and Secondary Flaws on Deflection and Re-initiation of Hydraulic Fractures at Orthogonal Pre-existing Fractures. *Geophys. J. Int.* 166 (3), 1454–1465.

Zhang, X., Jeffrey, R.G., and Thiercelin, M. 2007. Deflection and Propagation of Fluid-driven Fractures at Frictional Bedding Interfaces: A Numerical Investigation. *Journal of Structural Geology* 29(3), 396–410.

Zhang, X. and Jeffrey, R.G. 2008. Reinitiation or Termination of Fluid-driven Fractures at Frictional Bedding Interfaces. *Journal of Geophysical Research-Solid Earth* 113(B8).

Zhang, X., Wu, B., Jeffrey, R. G., Connell, L., & Zhang, G. (2017). A New Pseudo-3d Model for Hydraulic Fracture Growth in a Multilayered Rock. *International Journal of Solids & Structures*, 115-116, 208-223.

Zhao, X.P. Young, R.P., 2009. Numerical Simulation of Seismicity Induced by Hydraulic Fracturing in Naturally Fractured Reservoirs. In: Paper SPE 124690, SPE Annual Technical Conference and Exhibition, New Orleans, Louisiana, 4–7 October.

Zhao, Z.H., Li, X., Wang, Y., Zheng, B., Zhang, B. A Laboratory Study of the Effects of Interbeds on Hydraulic Fracture Propagation in Shale Formation. Energies 2016, 9, 556.

Zhou, J., M. Chen, Y. Jin, and G. Zhang. 2008. Analysis of fracture propagation behavior and fracture geometry using a tri-axial fracturing system in naturally fractured reservoirs. *Int. J. Rock Mech. Min. Sci.* 45, 7: 1,143–1,152.

Zou, Y., Ma, X., Zhang, S., Zhou, T., Li, H., 2016. Numerical Investigation into the Influence of Bedding Plane on Hydraulic Fracture Network Propagation in Shale Formations. *Rock Mech. Rock Eng*. 49, 3597–3614.